Experimental Study of a 1 MW, 170 GHz Gyrotron Oscillator

by

Takuji Kimura

Submitted to the Department of Physics
in partial fulfillment of the requirements for the degree of

Doctor of Philosophy

at the

MASSACHUSETTS INSTITUTE OF TECHNOLOGY

September 1997

© Takuji Kimura, MCMXCVII. All rights reserved.

Author . . . .
Department of Physics
June 25, 1997

Certified by . . . .
Richard J. Temkin
Senior Scientist, Physics Department
Thesis Supervisor

Accepted by . . . .
George Koster
Chairman, Departmental Committee on Graduate Students

Experimental Study of a 1 MW, 170 GHz Gyrotron Oscillator

by

Takuji Kimura

Abstract

A detailed experimental study is presented of a 1 MW, 170 GHz gyrotron oscillator whose design is consistent with the ECH requirements of the International Thermonuclear Experimental Reactor (ITER) for bulk heating and current drive. This work is the first to demonstrate that megawatt power level at 170 GHz can be achieved in a gyrotron with high efficiency for plasma heating applications. Maximum output power of 1.5 MW is obtained at 170.1 GHz in 85 kV, 50 A operation for an efficiency of 35%. Although the experiment at MIT is conducted with short pulses (3 μs), the gyrotron is designed to be suitable for development by industry for continuous wave operation. The peak ohmic loss on the cavity wall for 1 MW of output power is calculated to be 2.3 kW/cm^2, which can be handled using present cooling technology. Mode competition problems in a highly over-moded cavity are studied to maximize the efficiency. Various aspects of electron gun design are examined to obtain high quality electron beams with very low velocity spread.

A triode magnetron injection gun is designed using the EGUN simulation code. A total perpendicular velocity spread of less than 8% is realized by designing a low-sensitivity, non-adiabatic gun. The RF power is generated in a short tapered cavity with an iris step. The operating mode is the TE$_{28,8,1}$ mode. A mode converter is designed to convert the RF output to a Gaussian beam.

Power and efficiency are measured in the design TE$_{28,8,1}$ mode at 170.1 GHz as well as the TE$_{27,8,1}$ mode at 166.6 GHz and TE$_{29,8,1}$ mode at 173.5 GHz. Efficiencies between 34%–36% are consistently obtained over a wide range of operating parameters. These efficiencies agree with the highest values predicted by the multimode simulations. The startup scenario is investigated and observed to agree with the linear theory. The measured beam velocity ratio is consistent with EGUN simulation. Interception of reflected beam by the mod-anode is measured as a function of velocity ratio, from which the beam velocity spreads are estimated. A preliminary test of the mode converter shows that the radiation from the dimpled wall launcher is a Gaussian-like beam.

Thesis Supervisor: Richard J. Temkin
Title: Senior Scientist, Physics Department

Acknowledgments

Contents

List of Figures

7

8

List of Tables

Chapter 1

Introduction

1.1 Background

In the past few decades, there has been a considerable effort to provide coherent, high-power sources in the electromagnetic spectrum. Among many of these devices, gyrotrons have proven to be efficient sources for RF generation at high power levels and up to very high frequencies. The applications for gyrotrons range from microwave sources for general science and industry, medicine, high power radar, plasma diagnostics, material sintering, to RF driver for high gradient accelerators. The main motivation for the development of high frequency and high average power gyrotrons, however, is the application in magnetic fusion devices for plasma heating and for electron current drive, which require a frequency range above 100 GHz with power levels in excess of several hundred kilowatts.

The general term "gyrodevices" is a short version of "electron cyclotron masers", which are sources based on the stimulated cyclotron radiation of electrons oscillating in uniform static magnetic field, the mechanism of which is known as the cyclotron resonance maser (CRM) instability. In a gyrotron the electron beam gyrating in a homogeneous axial magnetic field inside an open resonator excites a TE waveguide mode at the frequency close to both the cut-off frequency of the resonator and to the cyclotron frequency or its harmonics. In such a system the influence of the radio-frequency (RF) magnetic field due to weak recoil-effect on the axial momentum of an electron is negligible. Hence only the transverse electron gyration energy can be converted into RF radiation. The radiation is excited or amplified by gyrating electrons

that bunch in phase to yield their energy to the fast-wave field. The phase bunching is caused by the relativistic dependence of the electron mass on its velocity.

The CRM resonance satisfies the synchronism condition between the electrons and the wave

$$\omega = n\frac{\omega_c}{\gamma} \pm k_z v_z, \tag{1.1}$$

where ω and k_z are the frequency and axial wavenumber, respectively, v_z is the axial electron velocity, $\omega_c \equiv eB_0/m_e$ is the cyclotron frequency in the guiding magnetic field of amplitude B_0, e is the unsigned charge of an electron, m_e is the electron rest mass, and $n = 1, 2, ...$ is the harmonic number. The cyclotron frequency is divided by the relativistic factor $\gamma = (1 - v^2/c^2)^{-1/2}$, where v is the speed of the electron, and c is the speed of light in vacuum. The dispersion equation for the electromagnetic waveguide mode is given by

$$\omega^2 = c^2(k_\perp^2 + k_z^2). \tag{1.2}$$

Here $k_\perp$ is the transverse wave number for a given mode in the structure. Eq. 1.1 and Eq. 1.2 combine to form the cold (uncoupled) CRM dispersion relation, and yield the approximate value of the resonant radiation frequency.

Although gyrotrons can operate throughout the microwave and millimeter wave spectra and beyond, several types of sources pose competition in certain spectral regimes. In the microwave region, conventional microwave tubes present strong competition by providing better efficiency and wider bandwidths at comparable power levels. In the submillimeter-wave range, gyrotrons suffer from the need to operate at harmonics of the cyclotron frequency because of the inherent limitations of the superconducting solenoids that provide the magnetic field. In this region, it appears that free electron lasers (FEL's) will be the principal competitor.

The advantage of the high average power capability of gyrotrons is particularly evident in the millimeter wave region. Conventional devices such as magnetrons, and slow wave devices such as klystrons, traveling wave tubes (TWT's), require structures comparable to or smaller than the wavelengths, and are prone to overheating or breakdown at high frequencies. Thus in this part of the electromagnetic spectrum they are severely limited in both power and efficiency.

In comparison, the gyrotron is a fast wave device that relies on a cyclotron resonance interaction between a helical electron beam and RF fields in a fast (unslowed) wave, the phase velocity of which is $v_\phi > c$. Such interaction can be stimulated in the RF field of a practically arbitrary spatial structure. As a result a simple, cylindrical resonator capable of withstanding high power can be used.

Because the gyrotron operates with the cavity near cutoff, i.e., the axial wave number of the excited mode is small, the negative influence of the axial velocity spread on the synchronism condition Eq. 1.1 is weak and the interaction efficiency is less sensitive to beam velocity spread than other fast wave devices such as the free electron lasers. However, because the gyrotron operates near cutoff, the RF fields in the cavity are very intense, and thermal heating of the cavity walls becomes a limiting factor when high powers are generated.

The next major fusion experiment being considered is the collaboration known as the International Thermonuclear Experimental Reactor (ITER). Auxiliary RF heating is being considered for a wide variety of missions in ITER, including ionization and plasma formation during start-up, bulk heating to ignition, localized heating combined with temperature profile shaping, and current drive. The main attraction of electron cyclotron heating (ECH) is the use of a simple launching structure capable of a high power density, and the strong coupling of the power to the plasma [1]. It is therefore easier to conform the ECH delivery system to the reactor constraints such as shielding than alternative RF systems. ECH will also require a smaller wall area for the launcher. The problem for ECH has always been the availability of a suitable source. Although gyrotron development has progressed rapidly since the 1970's, so has the need of fusion experiments for more powerful sources at higher frequencies. The heating to ignition in ITER can be achieved with 50 MW electron cyclotron wave power at frequencies in the range of 140 to 170 GHz [2], plus 50 MW of ICRF (ion cyclotron range frequencies) [3] or NBI (neutral beam injection) power [4]. For central current drive at 6 T an increased frequency above that required for heating alone (approximately 220 GHz) would increase the complexity of the system. However, steady state current drive with the same heating system at 170 GHz (or 160 GHz) is possible in an advanced operation scenario at $\sim$ 10 MA, where the ECH system may drive up to 2 MA of off-axis current for profile control [2]. Other applications of ECH include stabilization of the $m = 2$ neoclassic (tearing) mode in tokamaks [5], and possibly

discharge cleaning [6].

The single frequency system at 170 GHz could satisfy the ITER requirements of heating and off-axis current drive. This will put the electron resonance close enough to the magnetic axis for central heating. Because of the large size of planned ECH system, about $50 - 100$ MW are required, individual gyrotrons must produce at least 1 MW with an interaction efficiency greater than 30%. The development of high power ($\geq$ 1 MW) continuous wave (CW) gyrotrons and windows is still a critical issue to be resolved in developing an ECH system.

A large variety of experiments over the past decade have demonstrated that gyrotrons are capable of producing megawatt power levels at frequencies of 100 GHz and above. In the U.S., a 110 GHz gyrotron with a $TE_{22,6,1}$ mode cavity developed at Communications Power Industry (CPI) has achieved output powers of 680, 530, and 350 kW for pulse durations of 0.5, 2.0, and 10.0 s, respectively [7]. There is also a significant international gyrotron research effort, which is primarily motivated by the need for long pulse microwave sources for fusion plasma heating. Notable oscillator experiments include efforts at 84 GHz in Japan [8], 110 GHz in Russia [9], 118 GHz in Switzerland [10], and 140 GHz in Germany [11] that have produced powers between 0.5-1.0 MW for pulse lengths of 0.2-5.0s. The development of a 170 GHz ITER gyrotron represents another major challenge for gyrotron technology.

1.2 Thesis Layout

This thesis presents the experimental investigation of a 1 MW, 170 GHz gyrotron oscillator. The objective is to design, construct, and test a gyrotron which produces high output power with high efficiency, while keeping the design compatible with CW operation. Detailed design of the electron gun and the interaction cavity will be described. Experimental results will be analyzed and compared to theoretical predictions.

The thesis is organized in the following manner. An overview of the gyrotron theory will be presented in Chapter 2. In Chapter 3, detailed experimental design will be described, with a focus on the design of electron gun and interaction cavity. Experimental results are presented and discussed in Chapter 4. A summary of this work is given in Chapter 5 along with discussions of future plans.

14

Chapter 2

Theory

2.1 Theory of Gyrotron Oscillator

In this section, the basic theory of a gyrotron oscillator is discussed. Starting with the relativistic Vlasov equation, the linear dispersion of the cyclotron resonance maser instability is derived, leading to the calculation of the growth rate. For a self-consistent, non-linear theory of gyrotron oscillators, the equations of motion for the electrons under the influence of TE waveguide RF fields is derived, and the wave equation for the RF field profile function with the beam current as a source term is constructed. These are followed by a discussion of the multi-mode theory. Normalized parameters useful for charactering gyrotron operation are defined, and the starting current are given in terms of the normalized parameters. Finally the ohmic loss density is related to the output power and the mode indices, providing a trade-off equation for mode selection in a high power CW gyrotron design.

2.1.1 Physical Mechanism of CRM Instability

The main component of a gyrotron consists of electrons which are in helical motion along the lines of an externally applied axial magnetic field. An annular electron beam is produced by a magnetron injection gun whose properties will be discussed later in Sec. 2.2.1. The electrons are influenced by an electromagnetic wave with a transverse component of electric field in an open ended resonator. The electrons become bunched in phase in their cyclotron orbit such

15

that there would be net energy flow from the transverse electron motion to the electromagnetic wave. The phase bunching occurs because the relativistic electron cyclotron frequency is a function of electron energy. The electromagnetic wave is guided out of the system through a vacuum window.

The gyrotron interaction relies on the cyclotron resonance maser (CRM) instability. The existence of CRM instability was first discovered by three researchers independently in the late 1950's, Twiss [12] in Australia, Schneider [13] in the USA, and Gapanov [14] in Russia. Experimental verification came soon after in the 1960's in Russia [15] and the U.S. [16]. A major experimental breakthrough is the invention of gyrotron [17], which resulted in escalation of CRM power in the millimeter and submillimeter range.

Insight into the physical mechanism responsible for the CRM instability can be obtained from the phase bunching process as shown in Fig. 2.1. These figures were created by a nonlinear simulation code which will be described in Sec. 2.1.4. The code tracks the trajectories of sample electrons in a single beamlet under the influence of the RF fields in the TE mode of a weakly perturbed cylindrical waveguide and calculates the energy exchange between the electrons and the electromagnetic wave. In this particular simulation, the electrons are orbiting in the clockwise direction about a externally applied magnetic field. The electrons are also moving with constant velocity in the direction of the static magnetic field. The effect of the electron beam on the RF fields is taken into account, i.e., the electric field amplitude is calculated self-consistently.

Fig. 2.1 shows plots of the relative positions of 100 electrons in the beamlet. The time t is normalized to the initial cyclotron orbit time, $2\pi/\omega_{c0}$. The plot shows the transverse position of the electrons in $x - y$ coordinate with respect to the direction of the local electric field, which is designated by an arrow. The axial field profile and the axial location of each plot are shown in Fig. 3.4. Initially the electrons are uniformly distributed around the Larmor orbit. The relativistic cyclotron frequency is set at $\omega_c/\gamma = 0.956\omega$, where ω is the angular frequency of the RF field. Therefore the electrons are rotating slightly slower than the RF field. As time progresses the electrons begin to move in phase so as to produce a higher density of electrons at the phase position of the electric field and then drift behind in phase for energy extraction. The efficiency is calculated from the average energy loss of the electrons divided by the initial

16
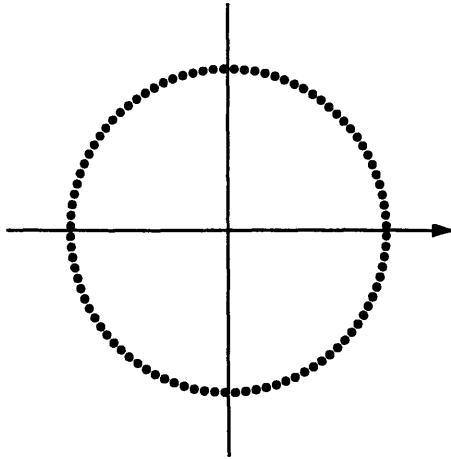
Plot 1: Time=14, Efficiency=0.0%   Plot 2: Time=28, Efficiency=4.0%
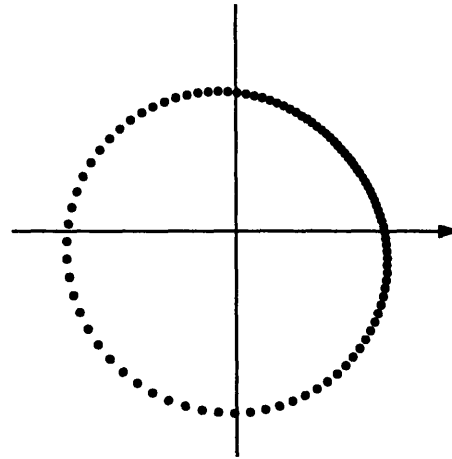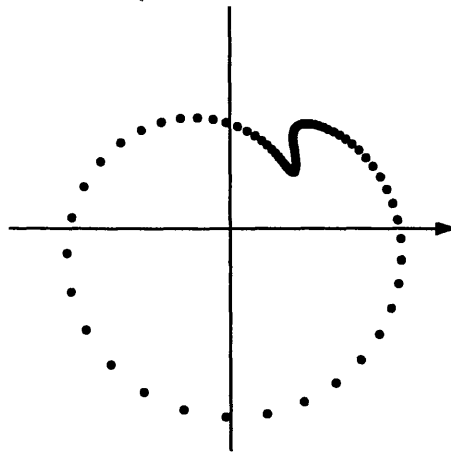
Plot 3: Time=36, Efficiency=21.1%   Plot 4: Time=42, Efficiency=41.2%
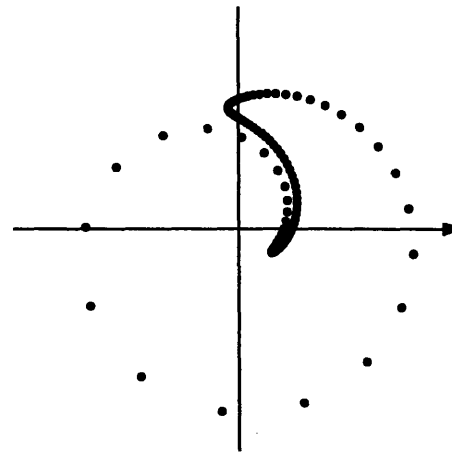
Figure 2.1: Evolution of transverse positions of the electrons in the frame of the local electric field in the CRM instability. The electrons are rotating in the clockwise direction. The arrow designates the direction of the local electric field.

17

beam energy. A positive efficiency means the beam gives up the energy to the RF wave.

It should be noted that phase bunching occurs in both axial and azimuthal velocity space. While the axial bunching leads to the Weibel instability, the CRM instability is due to phase bunching in the azimuthal direction [18].

2.1.2 Linear Theory

As pointed out by Davidson [19], the classical CRM instability in a nonneutral plasma in a static magnetic field $B_0 \hat{e}_z$ is a transverse electromagnetic instability driven by an inverted population in the perpendicular momentum dependence of the electron distribution function. To derive the dispersion relation for such a system, we start with the equation which governs the distribution of charged particles in a collisionless plasma, the relativistic Vlasov equation.

$$\frac{\partial f}{\partial t} + \mathbf{v} \cdot \frac{\partial f}{\partial \mathbf{r}} + q(\mathbf{E} + \mathbf{v} \times \mathbf{B}) \cdot \frac{\partial f}{\partial \mathbf{p}} = 0, \qquad (2.1)$$

where $f = f(\mathbf{r}, \mathbf{p}, t)$ is the particle distribution function. Linearize Eq. 2.1 by assuming that the dependent variables are the sum of a steady state part (subscript 0) and a small perturbation part (subscript 1), i.e., $f = f_0 + f_1$, $\mathbf{E} = \mathbf{E}_1$, $\mathbf{B} = \mathbf{B}_0 + \mathbf{B}_1$, the equation becomes

$$\frac{\partial f_1}{\partial t} + \mathbf{v} \cdot \frac{\partial f_1}{\partial \mathbf{r}} + q\mathbf{v} \times \mathbf{B}_0 \cdot \frac{\partial f_1}{\partial \mathbf{p}} =$$
$$-q(\mathbf{E}_1 + \mathbf{v} \times \mathbf{B}_1) \cdot \frac{\partial f_0}{\partial \mathbf{p}}. \qquad (2.2)$$

Here it is assumed that the electron density is sufficiently low ($s_e = \gamma \omega_{pe}^2 / \omega_{ce}^2 \ll 1$) such that the equilibrium self fields have a negligible influence on the electron trajectories. This equation can be integrated using the method of characteristics

$$f_1 = \int -q(\mathbf{E}_1 + \mathbf{v} \times \mathbf{B}_1) \cdot \frac{\partial f_0}{\partial \mathbf{p}} \, dt, \qquad (2.3)$$

where the integration is carried out over the unperturbed electron orbits. For the right-hand circularly polarized plasma wave with the perturbed quantities varying as

18

$$\psi_1 = \sum_{k_z=-\infty}^{\infty} \psi_1(k_z) \, e^{ik_z z - i\omega t}, \tag{2.4}$$

the dispersion equation has the following general form [19]

$$\omega^2 - k_z^2 c^2 = 2\pi \omega_p^2 \int_0^{\infty} p_\perp \, dp_\perp \int_{-\infty}^{\infty} dp_z \, \frac{f_0}{\gamma}$$

$$\times \left[\frac{\omega - \dfrac{k_z p_z}{\gamma m}}{\omega - \dfrac{k_z p_z}{\gamma m} - \dfrac{\omega_c}{\gamma}} - \frac{p_\perp^2 (\omega^2 - k_z^2 c^2)}{2\gamma^2 m^2 c^2 (\omega - \dfrac{k_z p_z}{\gamma m} - \dfrac{\omega_c}{\gamma})^2} \right], \tag{2.5}$$

where $\omega_c = eB_0/m_e$ is the non-relativistic cyclotron frequency, and $\omega_p = (n_e e^2/(m_e \epsilon_0))^{1/2}$ is the plasma frequency. For electrons drifting along the magnetic field with $p_z = p_{z0}$ and circling with perpendicular momentum $p_{\perp 0}$,

$$f_0 = \frac{\delta(p_\perp - p_{\perp 0})\delta(p_z - p_{z0})}{2\pi p_\perp}, \tag{2.6}$$

Eq. 2.5 becomes,

$$\omega^2 - k_z^2 c^2$$
$$= \frac{\omega_p^2}{\gamma} \left[\frac{\omega - k_z v_{z0}}{\omega - k_z v_{z0} - \omega_c/\gamma} - \frac{\beta_{\perp 0}^2 (\omega^2 - k_z^2 c^2)}{2(\omega - k_z v_{z0} - \omega_c/\gamma)^2} \right], \tag{2.7}$$

where $\beta_{\perp 0} = p_{\perp 0}/(\gamma m c)$. Eq. 2.7 is the dispersion relation for a plane wave CRM instability in an infinite plasma of streaming electrons. It is of fourth order in k_z. The fast wave branch of the solution exhibits the cyclotron maser instability for $k_z < \omega_c/[\gamma(c - v_z)]$, and $\gamma \omega_p^2/\omega_c^2 \ll 1$. The real oscillatory frequency and growth rate in the region of maximum growth are obtained from

$$(\omega - k_z v_z - \frac{\omega_c}{\gamma})^2 = -\frac{\beta_{\perp 0}^2 \omega_p^2}{2\gamma}. \tag{2.8}$$

Solving Eq. 2.8 for Re(ω) and Im(ω), one obtains,

19

$$\text{Re}(\omega) = k_z v_z + \frac{\omega_c}{\gamma},$$

$$\text{Im}(\omega) = \frac{\beta_{\perp 0} \omega_p}{\sqrt{2}\gamma}. \tag{2.9}$$

It should be emphasized that CRM instability is a relativistic effect and a relativistic treatment of the problem is necessary. This is evident from the fact that the term driving the instability in Eq. 2.7 is proportional to $\beta_{\perp 0}^2$, and the term vanishes in a nonrelativistic limit.

2.1.3 Nonlinear Theory

(i) Adiabatic Equations for Electron Motion

A nonlinear gyrotron theory is formulated here. Here we follow the derivation given by Fliflet *et al* in [20]. First a set of relativistic single-particle equations of motion is derived for the electrons in an annular beam where electrons follow helical trajectories due to a strong uniform static magnetic field and experience perturbing RF fields. Space charge effects are neglected. We begin with Maxwell's equations,

$$\nabla \times \mathbf{E} = -\frac{\partial \mathbf{B}}{\partial t}, \tag{2.10}$$

$$\nabla \cdot \mathbf{E} = \frac{\rho}{\epsilon_0}, \tag{2.11}$$

$$\nabla \times \mathbf{B} = \mu_0 \mathbf{J} + \mu_0 \epsilon_0 \frac{\partial \mathbf{E}}{\partial t}, \tag{2.12}$$

$$\nabla \cdot \mathbf{B} = 0, \tag{2.13}$$

and the Lorentz force equation for charged particles,

$$\frac{d\mathbf{p}}{dt} = -e(\mathbf{E} + \mathbf{v} \times \mathbf{B}) - e\mathbf{v} \times \mathbf{B_0}, \tag{2.14}$$

where $\mathbf{E}$ and $\mathbf{B}$ are the RF fields, and

$$\mathbf{B}_0 = B_0 \hat{\mathbf{e}}_z, \tag{2.15}$$

is the static magnetic field. It is convenient to use the normalized momentum variable

$$\mathbf{u} = \gamma \mathbf{v}, \tag{2.16}$$

and the relativistic factor is given by

$$\gamma = \sqrt{1 + \frac{u^2}{c^2}}, \tag{2.17}$$

where c is the speed of light. To obtain a slow time scale formulation, the following transformation is introduced for the transverse momentum

$$u_x + i u_y = i u_\perp e^{i(\Omega \tau + \phi)}, \tag{2.18}$$

where

$$\Omega = \frac{e B_0}{\gamma m_e} = \frac{\omega_c}{\gamma}, \tag{2.19}$$

is the relativistic cyclotron frequency, and

$$\tau = t - t_0, \tag{2.20}$$

where t_0 is the time the electron enters the interaction region. Eq. 2.14 can be rewritten as

$$\frac{du_\perp}{dt} = -a_x \sin(\Omega \tau + \phi) + a_y \cos(\Omega \tau + \phi), \tag{2.21}$$

$$u_\perp \left(\frac{d\phi}{dt} + \Omega - \frac{\omega_c}{\gamma} \right) = -a_x \cos(\Omega \tau + \phi) - a_y \sin(\Omega \tau + \phi), \tag{2.22}$$

$$\frac{du_z}{dt} = a_z. \tag{2.23}$$

Consider the beam interaction with the electric field of a TE circular waveguide mode. The electron beam interaction with RF magnetic field is small and can be neglected since the phase

velocity of the RF field is much greater than the speed of light for a wave near cutoff. The electric field of a TE$_{mp}$ mode is given by

$$\mathbf{E}(\mathbf{r}, t) = \mathbf{E}_\perp(\mathbf{r})e^{i\omega t} = \mathbf{E}_{mp}(r, \theta)f(z)e^{i\omega t}, \tag{2.24}$$

$$\mathbf{E}_{mp}(r, \theta) = A_{mp}\left[k_{mp}\,J_m'(k_{mp}r)\,\hat{\mathbf{e}}_\theta + i\frac{m}{r}J_m(k_{mp}r)\,\hat{\mathbf{e}}_r\right], \tag{2.25}$$

where J_m is the Bessel function of the first kind, the prime denotes differentiation with respect to the argument, and k_{mp} is the transverse wave number given by

$$k_{mp} = \frac{\nu_{mp}}{r_w}, \tag{2.26}$$

where ν_{mp} is the eigenvalue of the TE$_{mp}$ mode, i.e., the p-th root of the boundary equation $J_m'(x) = 0$, and r_w is the waveguide radius. The normalization constant is given by

$$A_{mp} = \frac{1}{\sqrt{\pi(\nu_{mp}^2 - m^2)}J_m(\nu_{mp})}. \tag{2.27}$$

The axial dependence of the RF fields in the resonator is given by the complex function

$$f(z) = |f(z)|e^{-i\phi(z)}. \tag{2.28}$$

The normalized forces due to the RF electric field are expressed as

$$a_x = -\frac{e}{m_e}(E_r\cos\theta - E_\theta\sin\theta), \tag{2.29}$$

$$a_y = -\frac{e}{m_e}(E_\theta\cos\theta + E_r\sin\theta), \tag{2.30}$$

$$a_z = 0. \tag{2.31}$$

Eq. 2.31 indicates that axial momentum of the electron is conserved since the interaction with the RF magnetic field is neglected. Substituting Eq. 2.29 and Eq. 2.30 into Eq. 2.21, using Eq. 2.25, and applying Graf's Addition theorem for Bessel functions [21], one obtains

an expansion in cyclotron harmonics,

$$
\begin{aligned}
\frac{du_\perp}{dt} = {}& -\frac{e}{2m_e} k_{mp} A_{mp} |f| \sum_{n=-\infty}^{\infty} (-1)^n \bigg[-J_{n+m-1}(k_{mp}r_g) J_n(k_{mp}r_L) \\
& \times \cos[\omega t + (n-1)(\Omega\tau + \phi) - \psi] + J_{n+m+1}(k_{mp}r_g) J_n(k_{mp}r_L) \\
& \times \cos[\omega t + (n+1)(\Omega\tau + \phi) - \psi] \bigg],
\end{aligned}
\tag{2.32}
$$

where r_g and r_L are the guiding center and Larmor orbit radii as shown in Fig. 2.2. Specializing to the interaction with a single harmonic $n = s$, one obtains

$$
\begin{aligned}
\frac{du_\perp}{dt} = {}& -\frac{e}{2m_e} k_{mp} A_{mp} J_{m-s}(k_{mp}r_g) [J_{s-1}(k_{mp}r_L) - J_{s+1}(k_{mp}r_L)] \\
& \times |f| \cos[(\omega - s\Omega)\tau + \omega t_0 - s\phi - \psi].
\end{aligned}
\tag{2.33}
$$

Similarly, from Eq. 2.22, one obtains

$$
\begin{aligned}
\left(\frac{d\phi}{dt} + \Omega - \frac{\omega_c}{\gamma} \right) u_\perp = {}& -\frac{e}{2m_e} k_{mp} A_{mp} J_{m-s}(k_{mp}r_g) \left[J_{s-1}(k_{mp}r_L) + J_{s+1}(k_{mp}r_L) \right] \\
& \times |f| \sin[(\omega - s\Omega)\tau + \omega t_0 - s\phi - \psi].
\end{aligned}
\tag{2.34}
$$

Introducing the slow time scale phase variable

$$
\Lambda = \left(\frac{\omega}{s} - \Omega \right) \tau + \frac{\omega}{s} t_0 - \phi,
\tag{2.35}
$$

and using

$$
r_L = \frac{u_\perp}{\omega_c} = \frac{u_\perp m_e}{e B_0},
\tag{2.36}
$$

the equation of electron motion can be written as
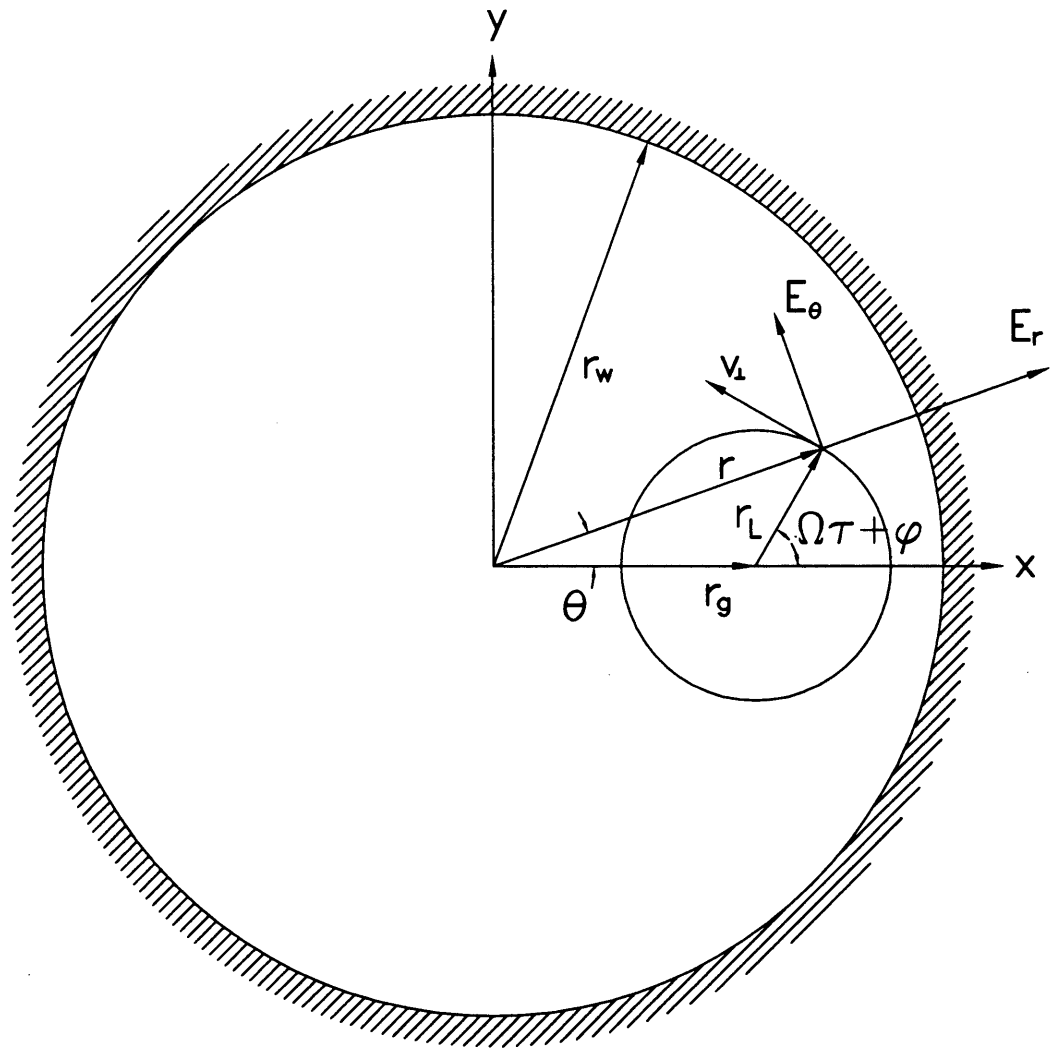
Figure 2.2: Geometry for Graf's Addition theorem. The electron is rotating in its gyro-orbit about its guiding center radius.

$$\frac{du_\perp}{dt} = -\frac{e}{2m_e}k_{mp}A_{mp}J_{m-s}(k_{mp}r_g)\left[J_{s-1}(\frac{k_{mp}u_\perp m_e}{eB_0}) - J_{s+1}(\frac{k_{mp}u_\perp m_e}{eB_0})\right]$$
$$\times |f|\cos(s\Lambda - \psi), \tag{2.37}$$

$$\frac{d\Lambda}{dt} = \frac{\omega}{s} - \frac{\omega_c}{\gamma} + \frac{e}{2m_e}\frac{1}{u_\perp}k_{mp}A_{mp}J_{m-s}(k_{mp}r_g)\left[J_{s-1}(\frac{k_{mp}u_\perp m_e}{eB_0}) + J_{s+1}(\frac{k_{mp}u_\perp m_e}{eB_0})\right]$$
$$\times |f|\sin(s\Lambda - \psi). \tag{2.38}$$

(ii) Wave Equation for the RF field profile function

Weakly irregular waveguide theory is used to obtain a wave equation with a current source for the RF profile function. Electron beam space-charge effects are neglected and only a single RF mode is assumed to be present. One starts with the Maxwell curl equations Eq. 2.10 and Eq. 2.12 to obtain the wave equation,

$$-\nabla \times \nabla \times \mathbf{E} = \mu\frac{\partial \mathbf{J}}{\partial t} + \frac{1}{c^2}\frac{\partial^2 \mathbf{E}}{\partial t^2}. \tag{2.39}$$

Assuming that $\mathbf{E}$ is written in terms of waveguide modes so that $\nabla \cdot E = 0$, Eq. 2.39 can be rewritten as

$$\nabla^2\mathbf{E} - \frac{1}{c^2}\frac{\partial^2 \mathbf{E}}{\partial t^2} = \mu\frac{\partial \mathbf{J}}{\partial t}. \tag{2.40}$$

Assuming steady state time-dependence $e^{i\omega t}$, the AC current density is given by

$$\mathbf{J}(\mathbf{r}, t) = \mathbf{J}_\omega(\mathbf{r})e^{i\omega t}, \tag{2.41}$$

where

$$\mathbf{J}_\omega(\mathbf{r}) = \frac{1}{2\pi}\int_0^{2\pi} \mathbf{J}(\mathbf{r}, t)e^{-i\omega t}\, d(\omega t). \tag{2.42}$$

Substituting Eq. 2.41 into Eq. 2.40 leads to the time-independent wave equation

$$\nabla \mathbf{E}^2 + \frac{\omega^2}{c^2}\mathbf{E} = i\mu\omega\mathbf{J}_\omega. \tag{2.43}$$

The electric field of a TE$_{mp}$ mode in a cylindrical waveguide is given by

$$\mathbf{E}(\mathbf{r}, t) = \mathbf{E}(\mathbf{r})e^{i\omega t}, \tag{2.44}$$

where

$$\mathbf{E}(\mathbf{r}) = \mathbf{E}_\perp(\mathbf{r}) = \mathbf{E}_{mp}(r, \theta)f(z) \tag{2.45}$$

and

$$\mathbf{E}_{mp}(r, \theta) = A_{mp}\left[k_{mp}J_m'(k_{mp}r)\hat{\mathbf{e}}_\theta + i\frac{m}{r}J_m(k_{mp}r)\hat{\mathbf{e}}_r\right]e^{-im\theta} \tag{2.46}$$

is the transverse mode vector function.

Combining Eq. 2.45 and Eq. 2.43 and neglecting mode coupling effects, one obtains

$$\mathbf{E}_{mp}\left[\frac{d^2}{dz^2} + \frac{\omega^2}{c^2} - k_{mp}^2\right]f(z) = i\mu\omega\mathbf{J}_\omega. \tag{2.47}$$

Multiplying by $\mathbf{E}_{mp}^*$ and integrating over the waveguide cross section leads to

$$\left(\frac{d^2}{dz^2} + \frac{\omega^2}{c^2} - k_{mp}^2\right)f(z) = i\mu\omega\int \mathbf{E}_{mp}^* \cdot \mathbf{J}_\omega\, da. \tag{2.48}$$

Here the orthonormality of the vector mode functions is used. To evaluate the right hand side of Eq. 2.48, note that the transverse current density is given by

$$\mathbf{J}_\perp = \rho\mathbf{v}_\perp, \tag{2.49}$$

where ρ is the linear charge density. If an idealized electron beam with a single guiding radius is considered, then

$$\rho = -\frac{I_b}{v_z}, \tag{2.50}$$

where I_b is the beam current.

26

Substituting Eqs. 2.46, Eq. 2.49 and Eq. 2.50 into the right hand side of Eq. 2.48 and making use of Eq. 2.18 leads to

$$
\int \mathbf{E}_{mp}^* \cdot \mathbf{J}_\omega \, da = -I_b k_{mp} A_{mp} \frac{1}{2\pi} \int_0^{2\pi} d(\omega t) \frac{v_\perp}{v_z} J_{m-1}(k_{mp}r)
$$
$$
\times \exp\left\{-i[\omega t - (m-1)\theta - \Omega\tau - \phi]\right\}. \tag{2.51}
$$

Expanding the Bessel function on the right hand side of Eq. 2.51 again using Graf's addition theorem yields

$$
\int \mathbf{E}_{mp}^* \cdot \mathbf{J}_\omega \, da = -I_b k_{mp} A_{mp} J_{m-s}(k_{mp}r_g) \frac{1}{2\pi} \int_0^{2\pi} d(\omega t) \frac{v_\perp}{v_z} J_{s-1}(k_{mp}r_L)
$$
$$
\times \exp\left\{-i[(\omega - s\Omega)\tau + \omega t_0 - \phi]\right\}. \tag{2.52}
$$

Here only the interaction with a single cyclotron harmonic is considered.

Since $t = t_0 + \int dz/v_z$ and $v_z \approx v_{z0}$, where v_{z0} is the initial longitudinal velocity, the average over (ωt) in Eq. 2.52 can be replaced by an average over (ωt_0) with little resulting error. Furthermore, since $\Lambda_0 = (\omega/s)t_0 + \phi_0$, where $\phi_0 = \phi(t = t_0)$, then

$$
d(\omega t_0) = s \, d\Lambda_0. \tag{2.53}
$$

Finally from Eq. 2.35, Eq. 2.36 and Eq. 2.52, using Eq. 2.53, one obtains the following equation for the RF profile function $f(z)$

$$
\left(\frac{d^2}{dz^2} + \frac{\omega^2}{c^2} - k_{mp}^2\right) f(z) = -i\mu\omega I_b k_{mp} A_{mp} J_{m-s}(k_{mp}r_g)
$$
$$
\times \frac{1}{2\pi} \int_0^{2\pi} d\Lambda \frac{v_\perp}{v_z} J_{s-1}\left(k_{mp}\frac{u_\perp}{\omega_c}\right) e^{-is\Lambda}. \tag{2.54}
$$

Eq. 2.37 and Eq. 2.38, together with Eq. 2.54 constitute a set of non-linear coupled equations for the gyrotron.

2.1.4 Self-Consistent Single-Mode Calculations

It is convenient to introduce a new variable

$$\zeta = \frac{\omega z}{v_{z0}}.$$ (2.55)

Then

$$\frac{d}{dt} = \frac{v_{z0}}{\omega v_z} \frac{d}{d\zeta}.$$ (2.56)

Thus the time dependence of the coupled equations can be eliminated and the numerical integration can be carried out over the axial distance, simplifying the computation process.

The desired solution to the coupled equations are those which satisfy the appropriate boundary conditions. The input RF boundary condition for a gyrotron is a growing evanescent wave

$$|f| = |f(\zeta = \zeta_0)|e^{k_0(\zeta - \zeta_0)},$$ (2.57)

where

$$k_0 = \sqrt{k_\perp(\zeta_0) - \omega^2/c^2}.$$ (2.58)

The initial phase of the profile function is arbitrary for an initially unbunched beam. Thus the initial conditions on the RF fields are completely specified by initial amplitude and operating frequency. The output RF boundary condition is an outgoing traveling wave given by

$$\frac{df}{d\zeta} = -ik_{\zeta f} f(\zeta_f),$$ (2.59)

where

$$k_{\zeta f} = \sqrt{\omega^2/c^2 - k_\perp(\zeta_f)}.$$ (2.60)

Eq. 2.59 corresponds to two conditions since f is complex. The solution of the coupled equations Eq. 2.37, Eq. 2.38, and Eq. 2.54 subject to oscillator boundary conditions constitutes an eigenvalue problem. The values must be found by a numerical search procedure. A

numerical code was developed for the calculation [22]. This code will be later referred to as the single-mode, self-consistent (SCSM) code.

From conservation of energy, the energy gained by the RF fields is equal to that lost by the electrons. Thus the electronic efficiency is calculated as

$$\eta_{elec} = \frac{\gamma_i - \langle \gamma_f \rangle}{\gamma_i - 1},$$

(2.61)

where γ_i is the initial value of the relativistic factor, equal for all electrons, and $\langle \gamma_f \rangle$ is the average of γ over all electrons leaving the interaction region.

An RF efficiency can be expressed as

$$\eta_{rf} = \frac{P_{rf}}{V_c I_b},$$

(2.62)

Here V_c and I_b are the cathode voltage and beam current, respectively. The RF output power can be computed by integrating the Poynting vector over the cross-section of the cavity after the field amplitude and the resonant frequency are solved self-consistently. The ratio of these two efficiencies should be

$$\frac{\eta_{rf}}{\eta_{elec}} = \frac{V_c - V_{dep}}{V_c},$$

(2.63)

where V_{dep} is the voltage depression of the electron beam in the cavity, which will be discussed in Sec. 2.2.3.

2.1.5 Mode Competition and Multi-Mode Theory

The self-consistent nonlinear theory given in Sec. 2.1.3 is based on the assumption that the gyrotron can always reach a steady state in which the radiation is of a single frequency and possesses a spatial structure transverse to the beam which is dominantly a single transverse mode of the empty cavity. However, the model excludes the possibility of any competing mode being excited. High-power gyrotrons in recent years are increasingly designed to operate in higher order mode due to ohmic loss constraints. Since the mode spectrum is very dense for higher order mode, the control of mode competition becomes an important aspect of the

29

gyrotron design process. It has been observed that operation in high order mode is often single moded, but competition from neighboring modes does affect the efficiency and the accessible operating modes.

The starting point for a multi-mode theory is the envelope equation for the mode amplitude. Here we follow the derivation given by Fliflet *et al* in [23]. The total transverse electric field is expanded as a superposition of transverse TE modes as

$$\mathbf{E}(r, \theta, z, t) = \sum_{n=1}^{N} A_n(z, t) \mathbf{E}_n(r, \theta, z) e^{-i\omega_0 t}, \tag{2.64}$$

where $\mathbf{E}_n = \hat{\mathbf{e}}_z \times \nabla_\perp \Psi$ is the waveguide transverse-mode vector function and Ψ is the corresponding scalar mode function which satisfies the Helmholtz equation with respect to the transverse coordinates. N is the number of interacting modes. An equation similar to Eq. 2.48 for the amplitude function can be obtained as

$$\left[2i \frac{\omega_0}{c^2} \frac{\partial}{\partial t} + \frac{\partial^2}{\partial z^2} + \frac{\omega_0^2 - \omega_{nc}^2}{c^2} \right] A_n(z, t) = -i\mu_0 \omega_0 \int \mathbf{E}_n^* \cdot \mathbf{J}_\omega \, da, \tag{2.65}$$

where derivatives with respect to z of the transverse vector function have been neglected, and ω_{nc} is the local mode cutoff frequency, which may depend on the axial position. The current density $\mathbf{J}_\omega$ is defined the same as Eq. 2.48.

At the cavity output, the amplitude function has the form of an outgoing wave,

$$A_n(z = L, t) = a_{nL}(t) e^{i(k_{nz}z - \psi_n(t))}. \tag{2.66}$$

Inside the cavity, the mode amplitude function can be approximated by

$$A_n(z, t) = a_n(t) e^{-i\psi_n(t)} h_n(z), \tag{2.67}$$

where $h_n(z)$ is an axial profile function which satisfies the Helmholtz equation

$$\left(\frac{d^2}{dz^2} + k_{nz}^2 \right) h_n(z) = 0. \tag{2.68}$$

The amplitude function in the cavity can be related to the mode amplitude at the output via the output Q factor according to

$$a_{nL}(t) = \left(\frac{W_n}{k_{nz}Q_n}\right)^{1/2} \frac{\omega_0}{c} a_n(t). \tag{2.69}$$

The free-running oscillator equations for the mode amplitude and phase can be derived as

$$\frac{da_n}{dt} + \frac{\omega_0 a_n}{2Q_n} = -\frac{\omega_0}{2\epsilon_0} \mathrm{Im} P_n(t), \tag{2.70}$$

$$\frac{d\psi_n}{dt} + \omega_0 = \omega_{cn} - \frac{\omega_0}{2\epsilon_0 a_n} \mathrm{Re} P_n(t), \tag{2.71}$$

where

$$P_n(t) = \frac{i}{W_n} \int_V da \, dz \, h_n(z) \mathbf{E}_n^* \cdot \mathbf{J}_\omega e^{i\psi_n}, \tag{2.72}$$

is the complex, slow-time-scale component of the electron-beam polarization for the mode n, and

$$W_n = \int_0^L dz \, |h_n(z)|^2. \tag{2.73}$$

The equation of motion for an electron interacting with several TE modes can be readily deduced following the procedure in the single-mode analysis.

A numerical code MAGY [24] was developed at the University of Maryland based on the multi-mode theory. The simulation is self-consistent, time dependent, multi-mode, multi-frequency. The code integrates the electron equations of motion for an ensemble of electrons uniformly distributed in azimuthal angle, self-consistently with the solution to the non-linear equations, computing the energy exchange between the electron beam and the electromagnetic field of the cavity. Each of the modes has a time dependent axial profile which is determined self-consistently with the response of the electrons and satisfies appropriate boundary conditions at both ends of the cavity.

2.1.6 Normalized Parameters

If certain profile function for the RF field in the cavity is assumed, then the nonlinear interaction between the beam and the RF field can be represented by generalized differential equations that describe the evolution of the energy of the electrons, and their phase with respect to the RF field [25]. When the beam is weakly relativistic ($\gamma \approx 1$), the perpendicular efficiency $\eta_\perp$ can be expressed in terms of the following three parameters for a given axial RF field profile.

$$\mu \equiv \pi \frac{\beta_{\perp 0}^2}{\beta_{z0}} \left(\frac{L}{\lambda}\right), \tag{2.74}$$

$$F \equiv \frac{E_0}{cB_0} \beta_{\perp 0}^{n-4} \left(\frac{n^{n-1}}{n!2^{n-1}}\right) J_{m\pm n}(k_\perp r_b), \tag{2.75}$$

$$\Delta \equiv \frac{2}{\beta_{\perp 0}^2} \left(1 - \frac{\omega_c}{\gamma\omega}\right). \tag{2.76}$$

Here $\beta_z = v_z/c$, $\beta_\perp = v_\perp/c$, λ is the wavelength, n is the harmonic number, μ is the normalized cavity interaction length, and L characterizes the width of the axial field profile $f(z)$. The parameter Δ indicates the detuning between the cyclotron frequency and the RF frequency. The plus and minus signs in the Bessel function subscript refer to co-rotation and counter-rotation of the RF fields with respect to the electron cyclotron motion, respectively. The coupling strength between the beam and RF field is represented by F, where r_b is the guiding center radius of the electron beam, and E_0 is the amplitude of the TE_{mp} circular electric field in the cavity given by

$$\mathbf{E}(r, \theta, z) = \text{Re}\left\{\left[J_m'(k_\perp r)\hat{e}_\theta + i\frac{m}{k_\perp r}J_m(k_\perp r)\hat{e}_r\right]E_0 f(z)e^{i(\omega t - m\theta)}\right\}. \tag{2.77}$$

The normalized parameters provide a compact description of the essential features of gyrotron behavior, and can be used regardless of the choice of mode. It is particularly useful for choosing the initial design parameters based on the optimized efficiency as function of F and μ. The starting current can also be calculated from the small signal gain of linear theory. Gaussian profile is a close approximation for the field profile of open cavities used in gyrotrons. The starting current for a fixed Gaussian field profile $f(z) = \exp(-4z^2/L^2)$ is calculated to be [25],

32

$$I_{st} = \frac{4}{\pi\mu} \frac{e^{2x^2}}{(\mu x - n)} I_0, \tag{2.78}$$

where $x = \mu\Delta/4$, and I_0 is given by

$$I_0 = \left(\frac{\pi}{2}\right)^{5/2} \left(\frac{\epsilon_0 m_e c^3}{e}\right) \frac{\gamma}{Q} \frac{L}{\lambda} \beta_{\perp 0}^{2(3-n)} \left(\frac{2^n n!}{n^n}\right)^2 \frac{(\nu_{mp}^2 - m^2) J_m^2(\nu_{mp})}{J_{m\pm n}^2(k_\perp r_b)}, \tag{2.79}$$

where Q is the quality factor of the cavity.

2.1.7 High Power and CW Constraints

For a gyrotron design to be compatible with CW operation, the ohmic losses on the cavity wall must be taken into account in the cavity design to prevent cavity melting or deforming. In a cylindrical cavity with slight irregularities in the waveguide radius, the RF electric and magnetic fields can be expressed as

$$\mathbf{E} = \left[i\frac{\mp m}{k_\perp r} J_m(k_\perp r)\, \hat{\mathbf{e}}_r + J_m'(k_\perp r)\, \hat{\mathbf{e}}_\theta\right] E_0 f(z) e^{\pm im\theta - \omega t}, \tag{2.80}$$

$$\mathbf{B} = \left[-i\frac{k_z}{\omega} J_m'(k_\perp r)\, \hat{\mathbf{e}}_r \mp i\frac{mk_z}{k_\perp r\omega} J_m(k_\perp r)\, \hat{\mathbf{e}}_\theta \right.$$
$$\left. +i\frac{k_\perp}{\omega} J_m(k_\perp r)\, \hat{\mathbf{e}}_z\right] E_0 f(z) e^{\pm im\theta - \omega t}. \tag{2.81}$$

where $f(z)$ is the axial field profile function. The ohmic loss density on the cavity wall can be calculated as [26]

$$\rho_{ohm} = \frac{1}{2\sigma\delta} |\hat{\mathbf{n}} \times \mathbf{H}|^2_{r=r_w}$$
$$= \frac{1}{2\sigma\delta\mu_0^2} \left(1 + \frac{m^2 k_z^2}{k_\perp^4 r_w^2}\right) \frac{k_\perp^2}{\omega^2} E_0^2 J_m^2(k_\perp r_w) |f(z)|^2, \tag{2.82}$$

where δ is the skin depth, σ is the conductivity, r_w is the radius of the cavity wall. The second term in the brackets is negligible in the cutoff limit $k_z \ll k_\perp$.

For a Gaussian axial profile function given by $f(z) = \exp(-4z^2/L^2)$, the stored energy in

the cavity is

$$U_w = \epsilon_0 E_0^2 \left(\frac{\pi}{2}\right)^{3/2} \frac{L}{2k_\perp^2} (v_{mp}^2 - m^2) J_m^2(v_{mp}). \tag{2.83}$$

The diffractive Q_D of gyrotron cavities in which the power is extracted from the end of the resonator, as opposed to the sides, is shown to be [27]

$$Q_D = \frac{4\pi}{1 - R_2} \left(\frac{L}{\lambda}\right)^2, \tag{2.84}$$

where L is the interaction length, λ is the wavelength, R_2 is the reflectivity at the output end of the cavity, and the input end is assumed to be cut-off. Using $Q_D \equiv \omega U_w / P$, where P is the power flow, and combining Eq. 2.82 and Eq. 2.83, one arrives at the equation relating the cavity mode indices to the ohmic loss density for a given output power,

$$
\begin{aligned}
(v_{mp}^2 - m^2) &= \frac{16\pi}{c^3} \sqrt{\frac{2}{\sigma \mu_0}} \left(\frac{L}{\lambda}\right) \frac{P \, v^{5/2}}{(1 - R_2) \, \rho_{ohm}} \\
&= 1.05 \times 10^{-3} \left(\frac{L}{\lambda}\right) \frac{P(\text{MW}) \, v^{5/2}(\text{GHz})}{(1 - R_2) \, \rho_\Omega(\text{kW/cm}^2)}.
\end{aligned}
\tag{2.85}
$$

Here an electrical conductivity of $5.0 \times 10^7 \, \Omega^{-1} \, \text{m}^{-1}$ for copper is assumed, corresponding to ideal conditions at room temperature. In actual operation, the cavity wall temperature can be as high as 250 °C [7], and the resulting higher resistivity can increase the ohmic losses by about 50-70%.

The trade-off equation Eq. 2.85 is very useful for determining a suitable mode for a given output power P and frequency v. This equation is plotted in Fig. 2.3 using L/λ of 6.5, which results in an efficient interaction between the beam and RF field, and a reflection coefficient R_2 of 0.5. Past experience with long pulse gyrotrons has shown that peak ohmic losses of about 2.3 kW/cm^2 (ideal condition) can be tolerated without degrading reliability. For 1 MW output powers at 170 GHz, a mode with $(v_{mp}^2 - m^2)^{1/2}$ greater than 52, such as the TE$_{28,8,1}$ mode, is required.

34
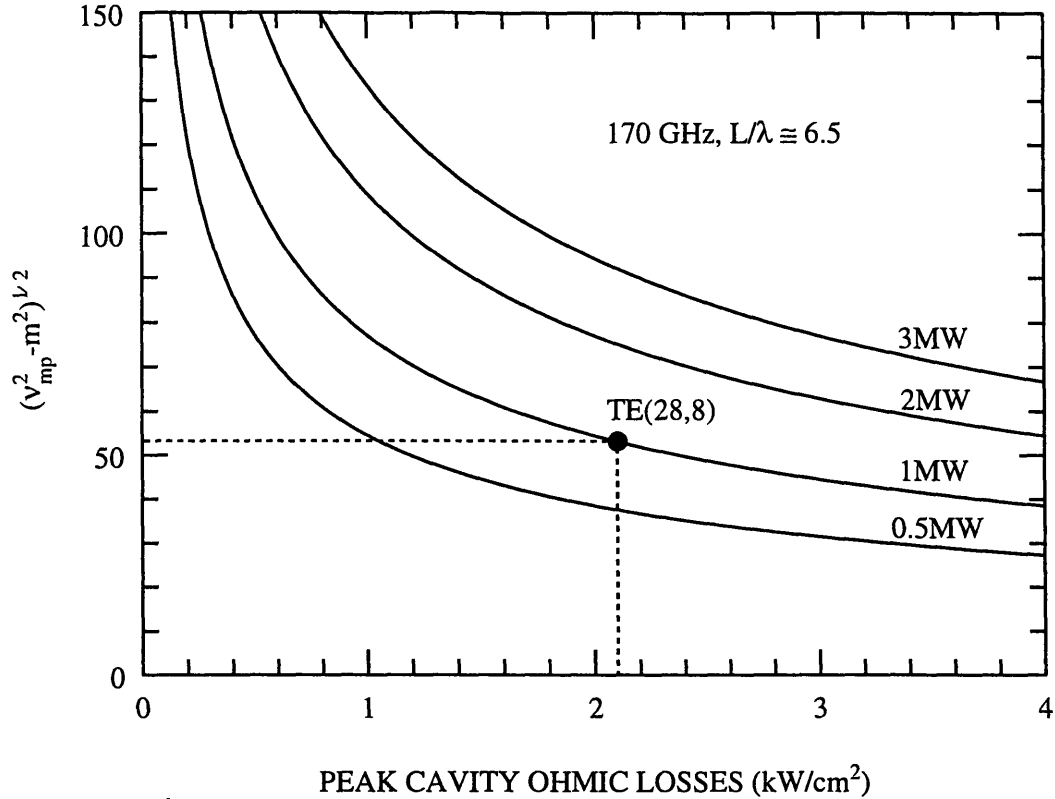
Figure 2.3: Plot of mode index vs. ohmic loss density.

2.2 Electron Beam Transport

In this section, the characteristics of the electron beam used in gyrotrons are studied. Adiabatic theory is used to characterize general features of electron beam produced by magnetron injection guns (MIG's). Design procedure based on electron trajectory code is described. The voltage depression and the space charge limiting current are expressed in terms of beam parameters. The sources of beam velocity spread are discussed.

2.2.1 Theory of Magnetron Injection Gun

Magnetron injection guns have been widely used in high power gyrotrons and have proven to be very successful. The characteristic feature of these guns is the emission of electrons in crossed electric and magnetic fields to form a beam with cyclotron motion. A typical MIG configuration and axial magnetic field profile are shown in Fig. 2.4. The MIGs used in gyrotrons are usually operated in temperature limited regime. Under temperature limited conditions, beam current

35

is a weak function of the applied voltage, and is varied by controlling the temperature of the emitter. The advantage of operating in temperature limited regime is that the behavior of the beam can be described approximately by analytical equations since space charge effects are weak and can be neglected.
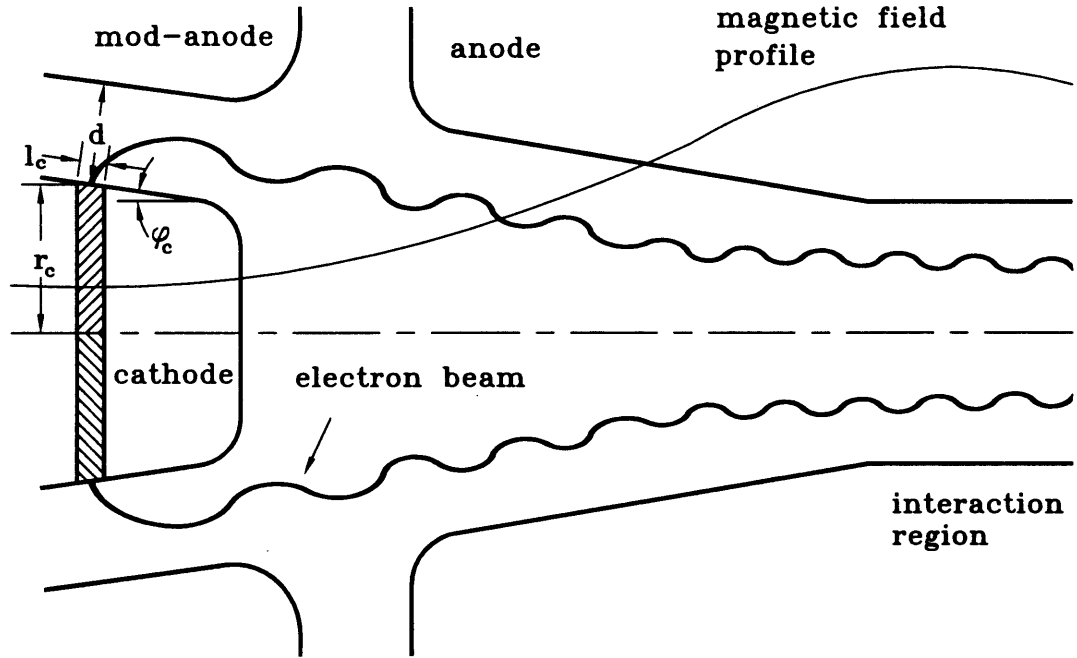
Figure 2.4: Schematic view of a magnetron injection gun.

The basic equations for describing the electron beam in a magnetron injection gun are based on the adiabatic approximation. The adiabatic approximation is valid if the variations in the electric and magnetic fields are rather small at characteristic dimensions of the electron trajectories. These conditions can be expressed as,

$$
z_L^2 \left| \frac{\partial^2 \mathbf{B}}{\partial z^2} \right| \ll \mathbf{B}, \qquad z_L^2 \left| \frac{\partial^2 \mathbf{E}}{\partial z^2} \right| \ll \mathbf{E},
$$

$$
z_L \left| \frac{\partial \mathbf{B}}{\partial z} \right| \ll \mathbf{B},, \qquad z_L \left| \frac{\partial \mathbf{E}}{\partial z} \right| \ll \mathbf{E}, \tag{2.86}
$$

where z_L is the axial distance the electron propagates during one cyclotron period. Since the static electric and magnetic fields in a MIG can be considered as slowly varying along the electron paths, the adiabatic theory is applicable. One of the adiabatic constants of motion is

36

the quantity

$$\frac{p_\perp^2}{2B} = \text{constant}, \tag{2.87}$$

where $p_\perp = \gamma m_e v_\perp$ is the transverse momentum of the electron, and B is the amplitude of the magnetic field.

The velocity of the electron in drift approximation can be written as

$$\mathbf{v} = \mathbf{v}_d + \mathbf{v}_\perp, \tag{2.88}$$

where $\mathbf{v}_d$ is the drift velocity, or the velocity of guiding center of the electron gyration, and $\mathbf{v}_\perp$ is the transverse velocity of gyration. Because the initial velocity at the emitter is zero, the transverse velocity should be equal but opposite in direction to the drift velocity. Therefore the initial velocity of an electron emitted from the cathode emitter is

$$v_{\perp c} = v_d = \frac{|\mathbf{E}_c \times \mathbf{B}_c|}{B_c^2} = \frac{E_c \cos \phi_c}{B_c}, \tag{2.89}$$

where B_c is the magnetic field at the cathode, ϕ_c is the slant angle of the emitter, which is very close to the angle between the emitter surface and the cathode magnetic field. For a conically shaped coaxial geometry the electric field at the emitter surface can be written as [28],

$$\begin{aligned} E_c &= V_a \frac{\cos \phi_c}{r_c \ln[1 + (d \cos \phi_c)/r_c]} \\ &\approx \frac{V_a}{d} \quad (\text{for } d \ll r_c). \end{aligned} \tag{2.90}$$

where V_a is potential difference between the cathode and the mod-anode, and d is the perpendicular distance between the two electrodes.

Once the initial velocity is determined, the perpendicular velocity in the interaction region can be determined from the magnetic field compression ratio. Since the relativistic mass factor at the cathode is $\gamma \approx 1$, from Eq. 2.87 , the perpendicular velocity in the cavity is given by

$$v_\perp = \frac{v_{\perp c}}{\gamma} \sqrt{\frac{B_0}{B_c}}. \tag{2.91}$$

where B_0 is the magnetic field amplitude in the cavity. Eq. 2.91 is the adiabatic expression for perpendicular velocity in the cavity in terms of the initial velocity and the compression ratio.

Another fundamental equation for the MIG comes from the conservation of canonical angular momentum: $(\gamma m_e r^2 \omega_e^2 - eB_z r^2/2) = $ constant. Here $\omega_e = d\theta/dt$ is the angular velocity of the electron, B_z is the axial magnetic field. It can be shown that in the cavity region,

$$(\gamma m_e r^2 \omega_e - eB_0 r^2/2) = (eB_0/2)(r_L^2 - r_g^2), \tag{2.92}$$

where r_g is the beam guiding center radius, and r_L is the Larmor radius given by

$$r_L = \frac{\gamma v_\perp}{\omega_c} = \frac{\gamma m_e v_\perp}{eB}. \tag{2.93}$$

Since the angular velocity initially at the cathode is zero, i.e., $\omega_e = 0$, hence

$$B_c r_c^2 = B_0(r_g^2 - r_L^2). \tag{2.94}$$

Electron beams in gyrotrons typically have $r_L \ll r_g$, thus the beam guiding center radius can be written in terms of the cathode emitter radius and the compression ratio as,

$$r_g = r_c \sqrt{\frac{B_c}{B_0}}. \tag{2.95}$$

Similarly the spread in guiding center radius is given by

$$\Delta r_g = l_c \sin\phi_c \sqrt{\frac{B_c}{B_0}}, \tag{2.96}$$

where l_c is the width of the emitter. Thus the beam thickness will be

$$\Delta r_b = \Delta r_g + 2r_L. \tag{2.97}$$

As already being pointed out, there is advantage of operating the gun in the temperature limited regime. This implies that the emitted current density J_c is substantially lower than

the space charge limiting (SCL) current density J_L. Between two conically shaped coaxial electrodes, the limiting current density is [28]

$$J_L = \frac{4\epsilon_0}{9}\left(\frac{2e}{m_e}\right)^{1/2}\frac{V_a^{3/2}}{d^2},\qquad(2.98)$$

Eqs. 2.88-2.98 are the basic equations for MIG design. Based on these equations, an existing cathode emitter was found to satisfy the following technical and physical constraints:

$$B_0/B_c \quad < \quad 50,\qquad(2.99)$$

$$J_c/J_L \quad < \quad 0.15,\qquad(2.100)$$

$$J_c \quad < \quad 10\,\text{A/cm}^2,\qquad(2.101)$$

$$E_c \quad < \quad 60\,\text{kV/cm},\qquad(2.102)$$

Here J_c is the emission density calculated from the required beam current and the area of the emitter surface. The constraint on compression is based on previous experience which has shown the higher the compression the more trouble there is with mirroring of electrons and arcing. The cathode emission is limited to $10\,\text{A/cm}^2$ so that longer lifetime ($\sim 10^6$ hours) for a standard dispenser cathode [29] is possible. The electric field on the electrode surface must be kept below about $100\,\text{kV/cm}$ to prevent field breakdown for a CW tube. Since normally the highest stress point is not at the cathode surface, the electric field limit at the cathode needs to be lower.

The choice of the slant angle ϕ_c influences whether the electron beam trajectories intersect each other within the gun region (non-laminar flow) or the flow is quasi-laminar. For a quasi-laminar flow, the transition from laminar to non-laminar state occurs in the beam tunnel section close to the interaction cavity. Previous study in Russia shows that for a specific gun, formation of a quasi-laminar beam requires an angle $\phi_c > 25°$. Laminar flows tend to reduce the sensitivity of velocity spread on increasing beam current.

2.2.2 Numerical Simulation of Electron Trajectories

The electron gun system can be numerically simulated with the widely used electron optics code EGUN [30]. The code was originally developed by W. B. Herrmannsfeldt at Stanford Linear Accelerator Center (SLAC). The code is designed to compute electron trajectories in electrostatic and magnetostatic fields. Also included are the effects of uniform space charge field and self-magnetic field. Problems can be treated in rectangular or cylindrical geometries. Axis symmetry is assumed in the cylindrical geometry. For calculations the EGUN code covers the cross-sectional geometry of the gun with square meshes of fixed size. Poisson's equation is solved by finite difference equations using boundary conditions defined by specifying the type and position of the boundary. Electric fields are determined by differentiating the potential distribution. The total beam is divided into a number of beamlets. The starting points of the beamlets are distributed equidistantly over the emitter length. The electron trajectory equations are fully relativistic and account for all possible electric and magnetic field components. Space charge forces are realized through appropriate deposition of charge density onto the grid points. A self-consistent solution is achieved iteratively.

The space charge weighing scheme in the code was modified to improve the accuracy of modeling. In the public-domain (PD) version of EGUN, the electric potential due to space charge at a given spatial location is calculated from the potential at two neighboring grid points. The choice of grid points is based on the local value of the trajectory radial velocity, dr/dz. For trajectories with $dr/dz < 45°$, charge is assigned to the two grid points at the same axial location, but are separated radially; for angles $dr/dz > 45°$, the two points are at the same radial position but differ axially. This space charge weighing scheme is very good for certain beams such as those from low to moderate-convergence Pierce-type guns [31], but may not be sufficiently accurate for a helical electron beam such as that used in a gyrotron. In the modified version, a four-point weighing scheme as shown in Fig. 2.5 is implemented. The space charge are assigned to the grid points according to $S_i = A_i S_0$, where A_i is the area diagonal to the i-th grid point, and $S_0 = -Id/v$ is the total space charge, I is the current carried by the representative beamlet, d is the distance the beam travels during one iteration cycle, and v is the beam velocity. The total area is normalized so that $\sum_i A_i = 1$. This type of weighing scheme is widely used in the particle injection codes. A typical simulation of the gun design

40

using the two schemes resulted in the same velocity ratio $v_\perp/v_\parallel$ of 1.6 in the cavity region, but slightly lower perpendicular velocity spread of 2.0% for the four-point scheme compared to 2.5% using the two-point scheme.
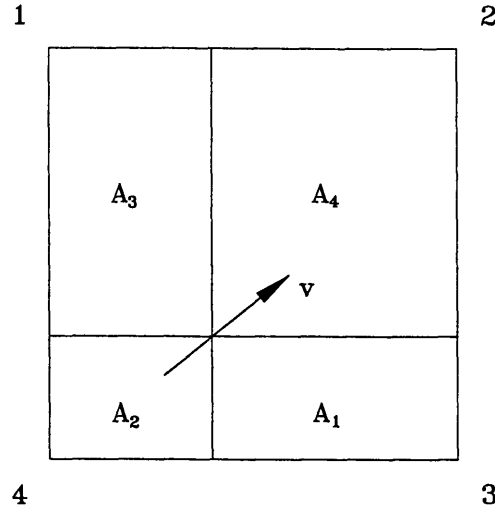
Figure 2.5: Illustration of the new space charge algorithm used in EGUN.

The maximum number of grid points that can be used in EGUN simulation is increased from 3×10^5 of the PD version to 3×10^6. This enables us to simulate beam propagation from the cathode to the cavity and even further in a single run without resorting to continuation runs. This also allows us to choose smaller grid sizes to accurately model the space charge effect. Generally simulation breaks down when the Larmor radius of the electron cyclotron orbit becomes comparable to half the mesh size since in this case the modeling of space charge becomes totally inadequate. In the present experiment, the Larmor radius of the electron in the interaction region is approximately 0.12 mm. Therefore a mesh size of less than 0.2 mm is required.

2.2.3 Voltage Depression and Limiting Current

The electron beam has to be transported from the gun to the interaction region and then further to the collector, where the electrons are stopped at the collector surface. Owing to the space charge in the beam the potential within the beam is reduced with respect to the wall potential. In a cylindrical tube with radius r_w, the potential depression V_{dep} between the tube and the the

axis of symmetry due to a concentric electron beam with a uniform current density is given by

$$V_{dep} = \frac{1}{4\pi\epsilon_0 c} \frac{I_b}{\beta_\parallel} G(r_i, r_a, r_w),$$ (2.103)

and G is a geometrical factor [32] defined as

$$G(r_i, r_a, r_w) = 2\ln\left(\frac{r_w}{r_a}\right) + \left[1 - \frac{2r_i^2}{\Delta r_b(r_a + r_i)} \ln\left(\frac{r_a}{r_i}\right)\right],$$ (2.104)

where r_i and r_a are the inner and outer beam radius and $\Delta r_b = r_a - r_i$. The first term of G corresponds to the potential drop between the wall and the outer beam radius. The term in the square brackets accounts for the potential drop over the thickness of the beam. For a thin annular beam with $\Delta r_b \ll r_i$ the geometrical factor reduces to $G(r_i, r_a, r_w) \approx 2\ln(r_w/r_a)$.

As a consequence of the voltage depression, a limiting current I_L can be determined for a given transverse momentum and a given cathode voltage. An increase in current beyond I_L causes an increase in the voltage depression in such a way that the axial velocity is reduced to zero and the beam no longer propagates and is reflected. The value of I_L needs to be considered when beam transport parameters are determined.

To derive the expression for limiting current, note that the relativistic mass factor can be written in terms of the voltage and voltage depression as

$$\gamma = 1 + \frac{e(V_c - V_{dep})}{m_e c^2}.$$ (2.105)

Combining Eq. 2.103 and Eq. 2.105, the beam current can be written as,

$$I_b = 4\pi\epsilon_0 c \frac{\beta_\parallel}{G}\left(1 + \frac{eV_c}{m_e c^2} - (1 - \beta_\perp^2 - \beta_\parallel^2)^{-1/2}\right).$$ (2.106)

The limiting current is obtained by maximizing beam current with respect to the parallel velocity while keeping the transverse momentum constant:

$$\left.\frac{\partial I_b}{\partial \beta_\parallel}\right|_{\gamma\beta_\perp = const} = 0.$$ (2.107)

This leads to the following expression [32] for the limiting current.

42

$$I_L(A) = \frac{4\pi\epsilon_0 m_e c^3}{e}\gamma_0[1-(1-\beta_{\|0}^2)^{1/3}]^{3/2}\frac{1}{G(r_i, r_a, r_w)}$$

$$= 1.707 \times 10^4\gamma_0[1-(1-\beta_{\|0})^{1/3}]^{3/2}\frac{1}{G(r_i, r_a, r_w)}\text{(Amp)}. \qquad (2.108)$$

where γ_0 and $\beta_{\|0}$ represents values in the absence of voltage depression. In the present experiment, the design parameters are 83 kV cathode voltage, 38 beam current and 1.6 velocity ratio, thus the limiting current is 74 A. Although velocity spread could further decrease the limiting current [33], beam reflection should not occur if $I_L/I_b \geq 2$. In case a 50 A, 83 kV beam is needed, the velocity ratio should be lower than 1.4 to keep the limiting current above 100 A.

2.2.4 Velocity Spread

Although the total energy is almost the same for all electrons produced by a MIG, it may be distributed between the perpendicular and parallel velocity components in different ways. The result is a velocity spread. The relation between the perpendicular and parallel velocity spreads can be obtained from the conservation of energy and is approximately given by

$$\frac{\Delta v_\perp}{v_\perp} = \alpha^2\frac{\Delta v_\|}{v_\|}. \qquad (2.109)$$

Large velocity spread reduces the interaction efficiency by allowing only part of the electrons to maintain the synchronism condition given by Eq. 1.1. Velocity spread also lowers the maximum achievable velocity ratio when parts of the beam start to be reflected from the magnetic mirror near the interaction region, thus further limiting the total efficiency.

The definition of velocity spread varies in different communities. In the US and at MIT, the spread is defined as the standard deviation (RMS) of the velocity distribution function. The definition used by Russian researchers is defined by the difference in the values of $v_\perp$ found at the levels 10% and 90% of the collector current cut-off curve. For a Gaussian distribution in perpendicular velocity, the Russian definition of the spread is roughly 2.6 times that of the US definition. For a square distribution the ratio is 2.8.

The primary cause of velocity spread is due to the beam optics since electrons emitted

from different sections of the emitter are exposed to different electric and magnetic fields. The electron beam space charge also increases spread. This effect is especially enhanced in a non-laminar flow of the electrons in the vicinity of the emitter region with entangled electron paths. For a gun with quasi-laminar flow, the transition from laminar to non-laminar state with intersecting electron paths occurs in the region where electron velocities are large and the influence of the space charge upon velocity spread is relatively weak. Because numerical gun code such as EGUN takes in to account the contributions from beam optics as well as uniform space charge effects, a careful design with a gun code can substantially reduce the spread due to these effects.

Besides beam optics and uniform space charge, additional velocity spread can be caused by the following factors:

1. Non-axisymmetric cathode magnetic field.

2. Non-axisymmetric cathode electric field.

3. Thermal spread of the initial velocities.

4. Roughness of the cathode surface.

5. Non-uniform emission density.

6. Instabilities caused by space charge.

7. Space charge effects of reflected electrons trapped between the magnetic mirror and the cathode.

Except the last two points, all of these factors introduce spreads to the initial velocity at the cathode. For an adiabatic beam flow, each of these spreads is a constant of motion along the beam path and accounts for the final spread in the interaction region. In Sec. 3.4.2, individual contributions from each of these sources will be investigated. Also a new design procedure for minimizing velocity spread will be presented.

Since these sources are statistically independent, their combined effect can be estimated by the statistical sum according to

$$\left(\frac{\Delta v_\perp}{v_\perp}\right)_{total} = \left[\sum_i \left(\frac{\Delta v_\perp}{v_\perp}\right)_i^2\right]^{1/2}. \tag{2.110}$$

2.2.5 Velocity Ratio Measurement

One major uncertainty in comparing experimental gyrotron efficiency with theoretical predictions is related to the uncertainty in the knowledge of the real beam parameters within the interaction region. The main beam parameters of interest are the average velocity ratio, the beam cross section, and the velocity spread. The beam cross section can be calculated fairly accurately from numerical simulation using gun code (EGUN) with a given magnetic field profile. The determination of the velocity spread is a more tricky problem, and will be discussed later in Sec. 4.2.2.

Here we describe the method used to experimentally measure the velocity ratio. It is based on the measurement of the parallel velocity of the beam using a capacitive probe. An earlier use of this device by several researchers was to measure electron beams in free electron lasers [34]. Later they were also used successfully in some of the gyrotron [35] and gyroklystron [36] experiments. The capacitive probe is a cylindrical device placed just before the entrance to the interaction cavity where the field is already uniform and therefore there is no substantial change of α. The principle for the measurement is the following. As the electron beam passes through the probe, an electric potential is induced on the probe's inner surface from the static radial electric field of the beam. Assuming constant axial density of the electron beam and infinite axial probe inner surface, the electric potential is given by

$$V_{cap} = \frac{e\lambda_e}{2\pi\epsilon_0} \ln\left(\frac{r_b}{r_{cap}}\right) = \frac{e\lambda_e}{C'}, \tag{2.111}$$

where λ_e is the electron density per unit length, r_b and r_{cap} are the beam and probe radii, C' is the capacitance. Then with the beam current given by $I_b = e\lambda_e v_\parallel$, the probe voltage and current measurements are combined to determine $v_\parallel$,

$$v_\parallel = \frac{I_b}{C'V_{cap}}. \tag{2.112}$$

Once $v_\parallel$ is determined, Eq. 2.103 can be used to calculate the voltage depression V_{dep}.

The relativistic mass factor, the perpendicular velocity, and the velocity ratio can be solved successively as,

$$\gamma = 1 + \frac{e(V_c - V_{dep})}{m_e c^2},$$ (2.113)

$$v_\perp = c\sqrt{1 - \frac{1}{\gamma^2} - \frac{v_\parallel^2}{c^2}},$$ (2.114)

$$\alpha = \frac{v_\perp}{v_\parallel}.$$ (2.115)

It is important to note that Eq. 2.111 is only correct for infinitely long cylinder. Due to stray capacitance of connections and edge effects of the probe, the capacitance C' cannot be calculated in a simple manner as shown in Eq. 2.111. Instead it needs to be calibrated experimentally. A reliable method of calibrating C' is to operate the gun at high cathode magnetic field and very low mod-anode voltage ($V_a < 1\,\mathrm{kV}$) so that the beam velocity ratio is close to 0.

In summary, the capacitive probe is a very useful passive device for measuring the beam velocity ratio. The results are reproducible and consistent with theory, and the calibration constant can be easily determined.

2.2.6 Energy Spread

Large energy spread of the beam could have much more detrimental effects on the gyrotron efficiency than the velocity spread. Calculation [24] shows that efficiency decreases by 10% for an RMS energy spread $\Delta\gamma/(\gamma_0 - 1)$ of 8%.

Energy spread due to electron-ion, electron-neutral-particle collisions are negligible with ultra-high vacuum in gyrotron tubes. However space-charge instabilities in the beam tunnel can cause energy exchange between electromagnetic or electrostatic waves and the electron beam, and increase the beam energy spread. To suppress the electromagnetic instabilities, the beam tunnel is built with lossy RF-absorbing materials, with slotted, uneven structures to prevent any spurious oscillations.

The effects of electrostatic instabilities on the beam energy spread have been studied by

Tran *et al* in [37] using 2-dimensional axisymmetric particle-in-cell codes. It was found that beam energy spread due to excitation of Bernstein modes strongly depends on the normalized density ω_p^2/Ω_{c0}^2, where $\omega_p = (n_e e^2/\epsilon_0 m_e)^{1/2}$ is the plasma frequency, and $\Omega_{c0} = eB_0/m_e$ is the nonrelativistic electron cyclotron frequency in the cavity. Since the beam used in the present experiment is designed to have a rather low density ($\omega_p^2/\Omega_{c0}^2 = 3 \times 10^{-4}$ for $I_b = 38\,\text{A}$), the RMS energy spread $\Delta\gamma/(\gamma_0 - 1)$ is estimated to be about 3%. With such an energy spread the predicted final efficiency decreases from 35% to 33% from the scaling in [24].

Another source of energy spread is the DC space charge due to finite beam thickness. For an annular beam of inner radius r_i and outer radius r_a, the energy spread is equal to the potential difference across the beam thickness given by the term inside the square brackets in Eq. 2.103. However for typical gyrotron beam parameters, the energy spread is on the order of 0.2% and is negligible.

Chapter 3

Experimental Design

3.1 Introduction

The purpose of this experiment is to study the physics of gyrotron interaction, demonstrate high power operation of a pulsed gyrotron at 170 GHz, and show that the design can be used in a CW operation. In this section, detailed design of this experiment is presented, with a focus on the design of the interaction cavity and the electron gun.

A schematic of the experiment is shown in Fig. 3.1. The experiment uses a superconducting magnet built by Cryomagnetics, Inc. The magnet is capable of providing magnetic field of up to 7.5 T. A λ-plate is also installed on the magnet. By pumping on the helium port, up to 9 T maximum field can be obtained so that the magnet can also be used to explore gyrotron operation over 200 GHz. The magnet consists of a pair of coils that allow tapering of the magnetic field. Such magnetic tapering has been used in the past to enhance the efficiency. However, the results presented in this thesis were obtained with a flat field at the cavity. A 20 cm warm magnet bore is large enough to accommodate components such as the mode converter and the 4-mirror transmission line.

The gyrotron is operated with the tube in horizontal position. A 2 liter/sec mini-pump attached to the rear of the gun and a vacuum gate valve (VAT-F10) is used to keep the electron gun under vacuum while the gyrotron tube is being assembled. A single 30 liter/sec vac-ion pump provides pumping for the whole system with a base pressure of 1×10^{-8} Torr and a pressure during operation of 4×10^{-7} Torr. The location and the orientation of the vac-ion

MIT ITER gyrotron schematic

electron gun

sc magnet

mirrors

pump

cavity   launcher

rf output

beam tunnel

gate valve

508mm
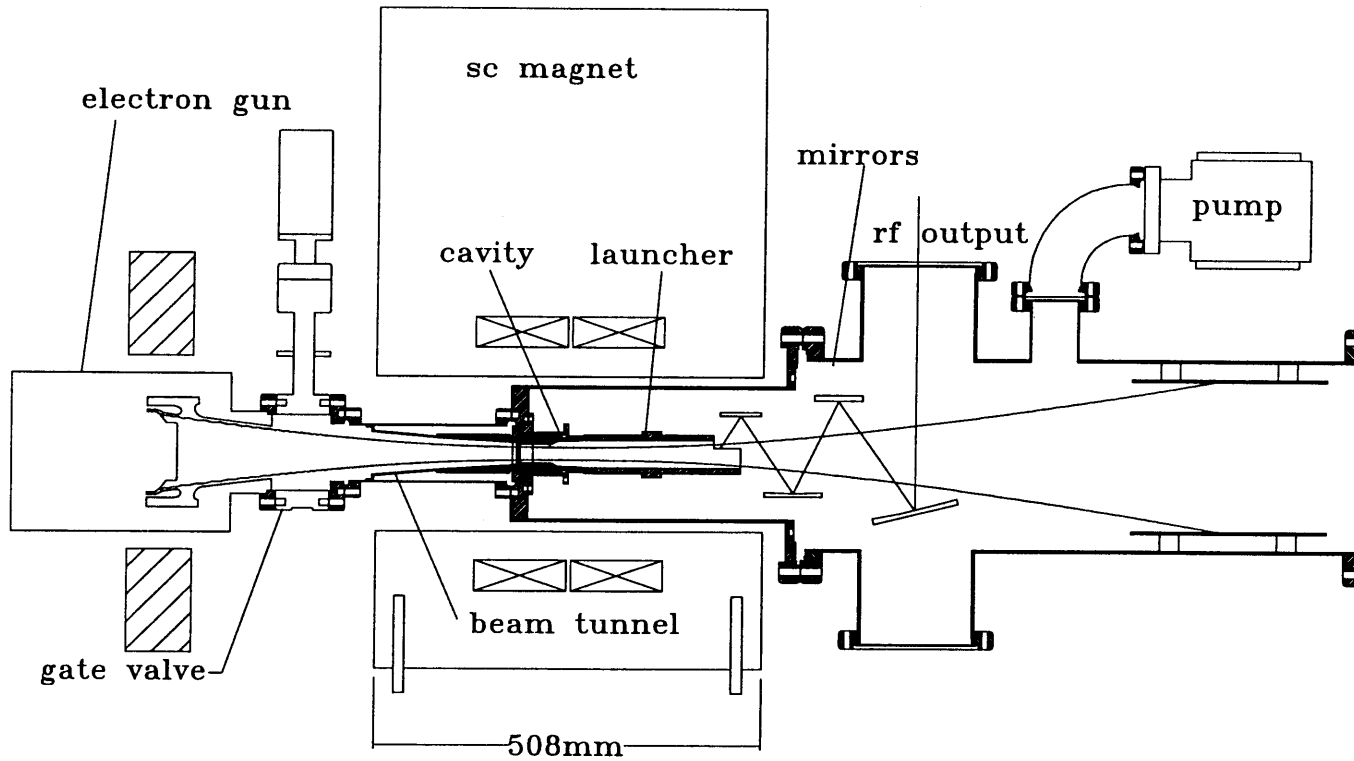
Figure 3.1: Schematic of the MIT 170 GHz gyrotron.

49

pump is chosen such that the magnetic field of the superconducting magnet does not disrupt the operation of the pump.

The electron beam is produced by a thermionic magnetron injection gun built by CPI. The electron beam is guided by the magnetic field to the cavity where the beam-RF interaction takes place. The spent electrons expand as they follow the magnetic field lines and reach the collector. The cavity is placed at the center of the magnetic field. A mode converter immediately follows the cavity, and converts the RF output from a TE_{mp} cylindrical waveguide mode to a Gaussian-like beam. The final output is emitted radially out of a 10 cm diameter vacuum window.

3.2   Mode Selection

The starting point for a design is the selection of the operating mode. As discussed in Sec. 2.1.7, for TE_{mp} mode at 170 GHz frequency, mode index of $(v_{mp}^2 - m^2)^{1/2} > 52$ is required in order to keep the peak ohmic loss density below $2.3\,kW/cm^2$. A number of high order modes can satisfy this condition. Voltage depression V_{dep} and limiting current I_L are further taken into account for the mode selection. Generally, the ratio of voltage depression and beam energy $V_{dep}/V_b < 10\%$ and the ratio of limiting current and beam current $I_L/I_b > 2$ are required. The former is from the efficiency point of view, the latter to prevent beam reflection. Lower azimuthal index m and higher radial index p correspond to larger cavity radius to beam radius ratio r_w/r_b, and this would increase the voltage depression and reduce the limiting current. On the other hand higher azimuthal index m seriously increases the potential for mode competition. Sufficient frequency separations are also needed between the main mode and any competing modes. Based on these considerations, the $TE_{28,8-}$ mode is selected as the operating mode.

General characteristics of the $TE_{28,8-}$ mode are shown in Table 3.1. The minus sign denotes the counter-rotation of the RF field with respect to the electron cyclotron motion.

Mode	TE$_{28,8}$-
Eigenvalue, ν_{mp}	60.101
$J_{28}(\nu_{mp})$	0.109
r_b/r_w	0.490
$J_{27}(\nu_{mp}r_b/r_w)$	0.221

Table 3.1: Characteristics of TE$_{28,8}$- mode.

3.3 Interaction Cavity

Because this experiment is our first attempt to build a prototype of a 170 GHz megawatt gyrotron that would meet the requirements of ITER, we decided to choose conservative design features that had been successfully demonstrated in past tests. They are based on a cylindrical tapered cavity that has proven very successful in previous high power gyrotrons [7].

First a cold cavity code CAVRF is used to calculate the resonant frequency and quality factor of a given cavity without the presence of the electron beam. The cavity is designed to oscillate in the TE$_{28,8}$- mode at 170 GHz, with an equivalent interaction length and a diffractive Q that yields optimum efficiency as computed by the normalized variable method. In the cold cavity approximation, knowledge of the resonator eigenfrequencies, quality factors and RF longitudinal field variations $f(z)$ of a TE or TM mode in an open cavity with weakly irregular profile can be determined from the numerical solution of the one-dimensional wave equation $d^2 f(z)/dz^2 + k_z^2 f(z) = 0$ with appropriate boundary conditions. Here k_z is the axial mode propagation constant. This is the same equation as Eq. 2.48 without the current source term on the right-hand side. Cold cavity simulation simplifies the designing process and allows one to quickly determine the essential features of the cavity. Fig. 3.2 shows the cold cavity simulation result for the initial cavity design. Plotted are the cavity wall profile, the amplitude and the phase of the RF field profile function $f(z)$ against the axial distance z. The code also calculates the resonant frequency, the diffractive Q, the effective length of the cavity, the peak ohmic loss density for 1 MW output power, the power leak to the input end in fractions, and the normalized parameters F and μ. These are summarized in Table 3.2.

The cavity profile is further optimized using a self-consistent, single-mode (SCSM) code based on the non-linear theory described in Sec. 2.1.3. The beam guiding center radius in the cavity is chosen to be 0.828 cm, which corresponds to the inner maximum of the coupling
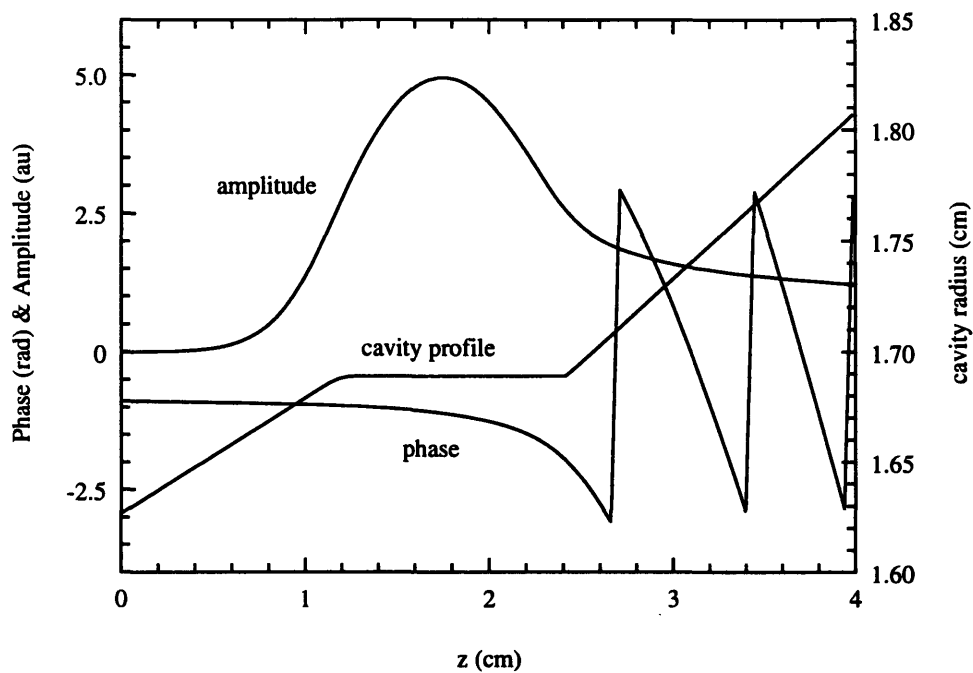
Figure 3.2: Initial cavity design simulated with the cold cavity code. Shown here are the cavity profile and the amplitude and phase of the axial profile function $f(z)$.

Frequency f	170.0 GHz
Diffractive Q	1312
L/λ	7.7
Peak ohmic loss density	$2.0\,\text{kW/cm}^2$
Power leak	0.000%
F	0.094
μ	16.1

Table 3.2: Parameters calculated by the cold cavity code for the initial cavity design .

between the electron beam and the electric field of the $\text{TE}_{28,8^-}$ mode. The coupling coefficient is given by

$$C_{mp} = \frac{J^2_{m\pm n}(k_\perp r_b)}{\pi(v^2_{mp} - m^2)J^2_m(v_{mp})}. \tag{3.1}$$

The first cavity we designed was a conventional cylindrical cavity with a 1.2 cm long straight section with linear tapers on both ends. Based on the cold cavity simulation, the straight section length and the taper angles are adjusted to obtain the desired frequency, the quality factor, the normalized field parameter F, and the normalized interaction length μ. Using the SCSM code, the cavity shape was optimized for the highest efficiency while peak ohmic loss is kept within $2.3 \, \text{kW/cm}^2$. An electronic efficiency of 48%, corresponding to an RF efficiency of 45%, was achieved for a 77 kV, 35 A beam with α of 1.6.

The multimode code MAGY is used to determine how mode competition would affect the efficiency of this cavity. Excitation of competing modes are examined when oscillation in the designed mode is present. The simulation can include two competiting modes in each run, and therefore different combinations of modes were tested. The simulation predicts a maximum RF efficiency of only 32% with single mode emission in the designed mode. As suggested by [38], the cavity was unable to achieve high efficiency because of the long interaction length $\mu = 16$ that reduces the region of stable operation for the design mode against the excitation of the competing mode.

To circumvent this problem, we decided to choose a cavity with a short straight section. As shown in Fig. 3.3, the final design of the cavity consists of the the following four sections: 3.2 degree linear input taper, 0.8 cm long straight section, a 5×10^{-3} cm radial dimension iris step, and a nonlinear uptaper to 1.875 cm radius. As the length of the straight section is reduced, the quality factor Q dropped to 800 since Q scales as $(L/\lambda)^2$. As a result the maximum achievable efficiency is below 35%. The iris step is introduced to increase the reflection at the cavity output end and raise the quality factor. The iris cavity has a diffractive Q of 1385 based on the self-consistent simulation. Operating well above the minimum Q is needed to achieve high efficiency, and helps to reduce the cavity's sensitivity to external reflections.

Among the features of the cavity, the linear input taper prevents excitation of any backward

wave propagating to the cathode region and disrupt the gun operation. The angle of the input taper should be as small as possible to limit the number of modes that are cutoff in the cavity, and thereby limit the number of high Q modes. Small taper angle also allows the design to have longer evanescent region so that there will be enough attenuation to prevent the power from leaking back to the gun. However, if the angle is too small, the taper can act as an interaction region for competing modes and thus degrade the beam quality and lower the efficiency. These are the considerations for selecting 3.2° as the angle for the input taper.

The transitions between sections are rounded in order to minimize the mode conversion that could cause power leakage back into the gun region. Mode conversion would also occur if a linear taper is used at the cavity output end. Calculation shows a 6 degree linear taper causes approximately 10% power conversion into other modes. Therefore a nonlinear taper is needed to form transition from the iris step to the radius of the mode converter. A computer code TAPER which solves the generalized Telegraphist's equations [39] is used for the nonlinear taper design. The profile of the nonlinear taper consists of an arc, a linear taper, and another arc, as shown in Fig. 3.3. The mode purity is calculated to be 99.4%. In the initial experiment, another nonlinear taper is placed between the first taper and a straight cylindrical waveguide which propagates the RF to the output window. The mode purity for this taper is calculated to be 99.1%.
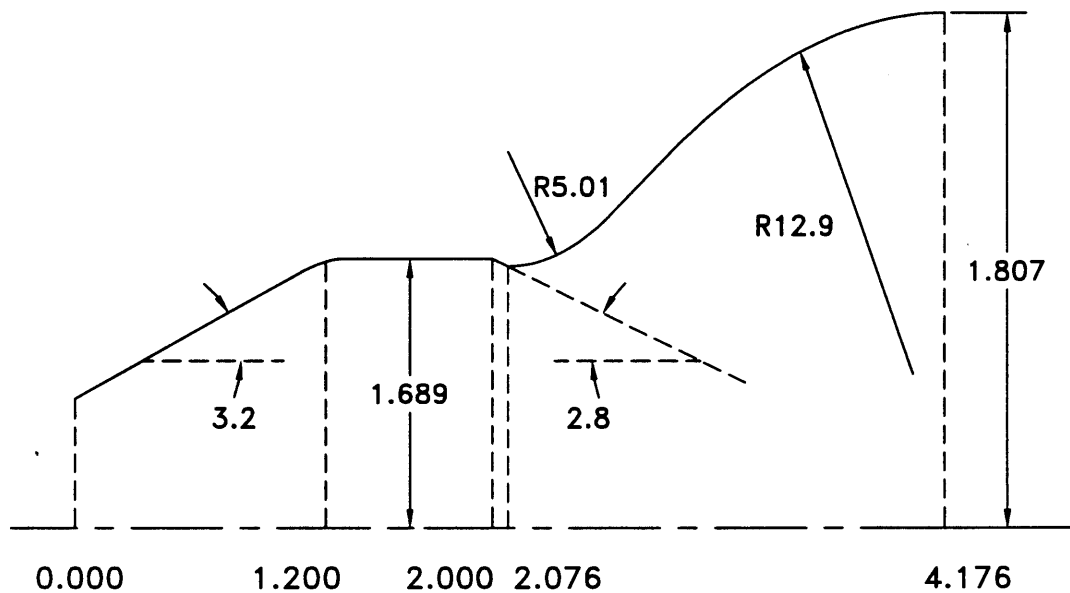
Figure 3.3: Profile of the 170 GHz gyrotron cavity. Unit of length in cm, angle in degree.

Mode	TE$_{28,8,1}$
Frequency f	170.0 GHz
Cathode voltage V_c	83 kV
Beam current I	38 A
Voltage depression ΔV	6 kV
Velocity ratio α	1.6
Magnetic field B_0	6.67 Tesla
Beam radius r_b	0.828 cm
Final power	1.1 MW (See Table 3.4)
Final efficiency	35% (See Table 3.4)
Peak ohmic loss density	2.3 kW/cm^2 (for $P = 1$ MW)
L/λ	6.5
Diffractive Q	1385
F	0.09
μ	14

Table 3.3: Design parameters for the cavity

Study shows that operating at lower beam voltage could reduce wall ohmic losses [40]. However low beam voltage is also associated with larger voltage depression and lower limiting current, as well as the increased beam current required to achieve a required output power. Thus the cathode voltage is chosen at 83 kV and the beam current of 38 A is set by the required output power of 1 MW. For these operating parameters and a velocity ratio of 1.6, the voltage depression V_{dep} is calculated from Eq. 2.103 to be 6 kV. Thus the beam voltage V_b is 77 kV.

The performance of the iris cavity is investigated with the SCSM code. A typical simulation result is shown in Fig. 3.4. Here the electronic efficiency η_{elec}, the cavity wall profile, and the RF profile function $f(z)$ are plotted against the axial distance z. Total RF power of 1.32 MW is obtained with a 77 kV, 38 A beam, corresponding to an electronic efficiency of 45%. The peak ohmic loss density on the cavity wall is calculated to be 2.6 kW/cm^2 for ideal copper at room temperature. To simulate the actual CW operation, the magnetic field is slightly increased to yield an output power of 1.15 MW. In this case, the peak ohmic loss density is calculated to be 2.3 kW/cm^2. The design parameters for this cavity are listed in Table 3.3.

Using the SCSM code, the efficiency is calculated as a function of the detuning parameter Δ which is defined by Eq. 2.76. The result is shown in Fig. 3.5. Here a velocity ratio of $\alpha = 1.6$ is kept as constant for a 77 kV, 38 A electron beam while the magnetic field is varied. A velocity spread of $(\Delta v_\perp / v_\perp)_{rms} = 10\%$ is assumed in the calculation. The corresponding
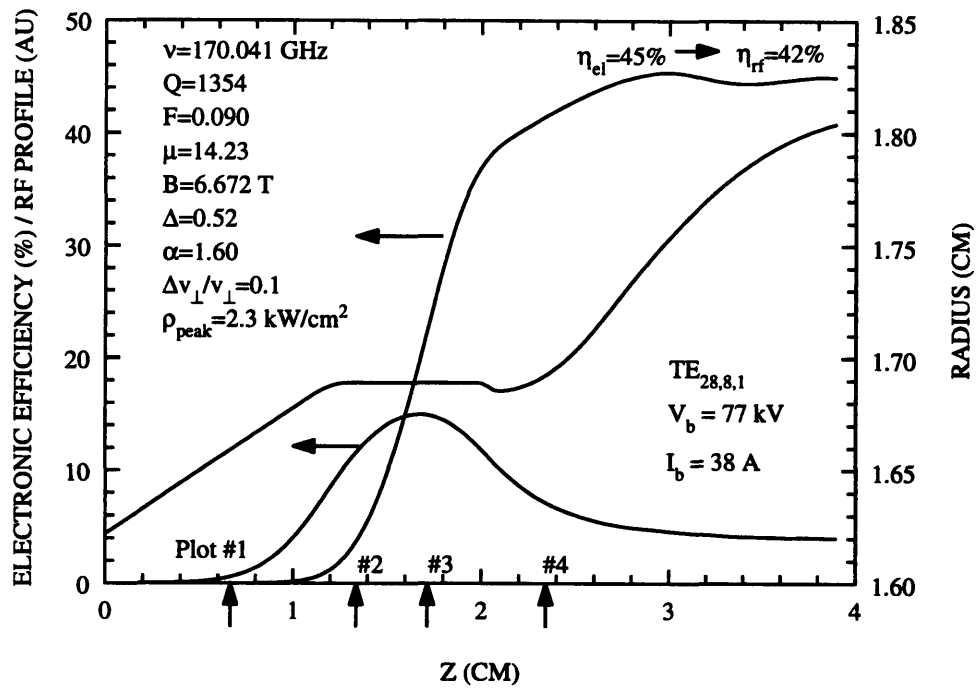
Figure 3.4: Result of cavity simulation using the self-consistent, single-mode code. Plotted are the radius of the cavity, the axial profile of the RF electric field, and the calculated electronic efficiency. The arrows on the horizontal axis designate the locations at which the transverse positions of electrons in the Larmor orbit as shown in Fig. 2.1 are evaluated.

magnetic fields are 6.711 T at Δ of 0.45 and 6.623 T at Δ of 0.53 for these beam parameters. The maximum RF efficiency of 42% is obtained at Δ of 0.52.
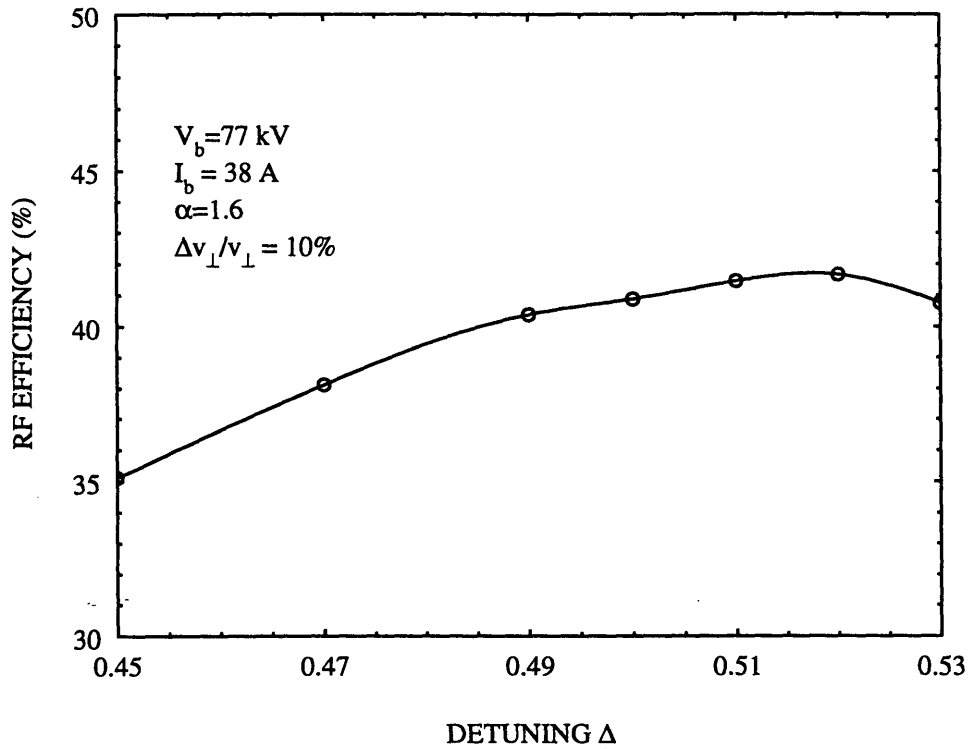
Figure 3.5: Efficiency versus detuning parameter at fixed cathode voltage, beam current and beam α.

The electronic efficiency of 45% is calculated from $\eta_{elec} = P_{out}/(V_b I_b)$, where P_{out} is the power generated in the cavity, V_b and I_b are the beam voltage and beam current, respectively. Taking into account the voltage depression V_{dep} of 6 kV between the beam and the cavity wall, the RF efficiency $\eta_{rf} = P_{out}/(V_c I_b)$ will be 42%. Note that the cathode voltage is $V_c = V_b + V_{dep}$. An additional power loss of 11% is estimated. This includes the ohmic loss in the cavity, diffraction and ohmic loss in the mode converter, and absorption by the window. The resulting final efficiency is 38%. During the initial operation, instead of the mode converter, a 2.223 cm radius, 78 cm long cylindrical waveguide is used to propagate the RF from the cavity to the output window. Since the ohmic loss in this waveguide is approximately the same as the losses in the mode converter, the final efficiency is also 38%. As will be discussed later, multimode theory predicts that the maximum efficiency as calculated by the single mode theory

	Single-mode theory	Multi-mode theory
Beam voltage (kV)	77	77
Beam current (A)	38	38
Velocity ratio	1.6	1.6
Cavity magnetic field (T)	6.67	6.70
Detuning Δ	0.52	0.47
Power from cavity (MW)	1.32	1.20
Electronic efficiency	45%	42%
RF efficiency	42%	39%
RF losses (MW)	0.145	0.132
Final output power (MW)	1.17	1.07
Final efficiency	38%	35%

Table 3.4: Summary of efficiency calculations. Perpendicular velocity spread of 10% is assumed.

can not be achieved due to mode competition from the azimuthal competing mode. For the case with 77 kV beam voltage, 38 A beam current and velocity ratio of 1.6, the highest detuning that can be reached is 0.47. Higher detuning will result in multimoding. It can be seen from Fig. 3.5 that the optimum RF efficiency is about 4% lower than the prediction based on the assumption of single mode oscillation. Therefore if mode competition is taken into account, the final efficiency for this gyrotron is predicted to be 35%. A summary of the efficiency calculations is given in Table 3.4.

Using the SCSM code, optimized efficiency is calculated for different values of velocity ratio. The result is shown in Fig. 3.6. It seems natural that the optimized efficiency increases with α because more energy is contained in the transverse motion of electrons. An interesting comparison of experimental data with this theory will be made later in Sec. 4.1.2. In the actual experiment, beam with a finite velocity spread and a very high α will be reflected from the magnetic mirror near the cavity. The maximum achievable α usually does not exceed 2.

The SCSM code is also used to study the effect of beam radius on the efficiency. The result is shown in Fig. 3.7. In the SCSM simulation, zero beam thickness is assumed. The result indicates that beam radius can be varied substantially without decreasing the efficiency, and with the beam guiding center spread of 0.025 cm as predicted by EGUN, close to peak efficiency can be obtained.
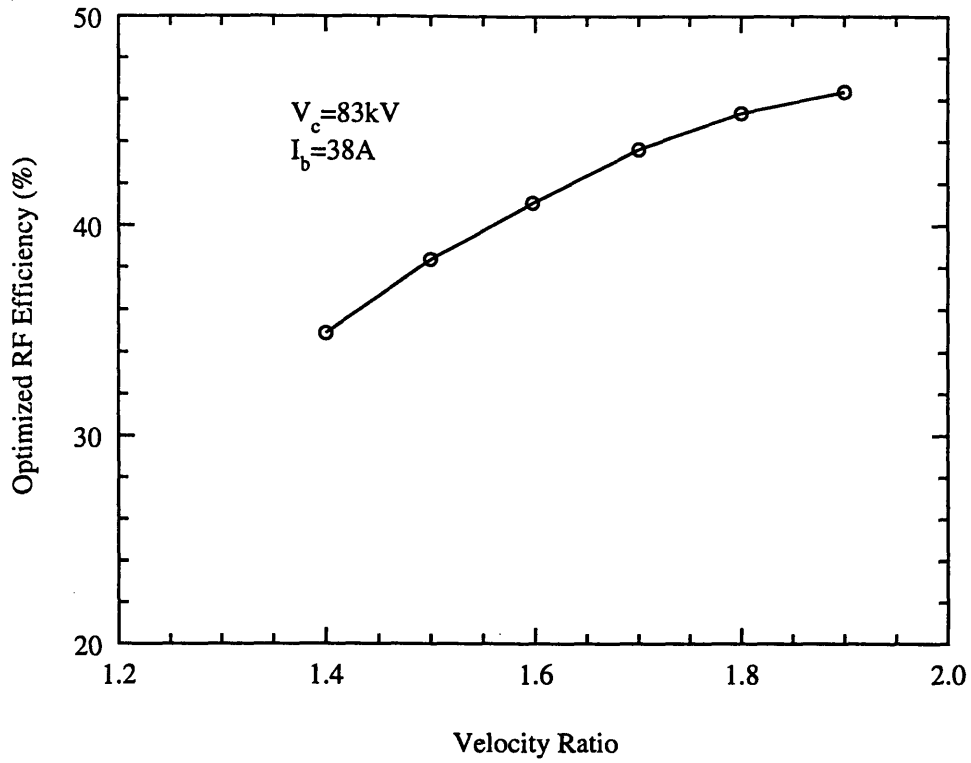
Figure 3.6: SCSM result of optimized efficiency vs. velocity ratio.
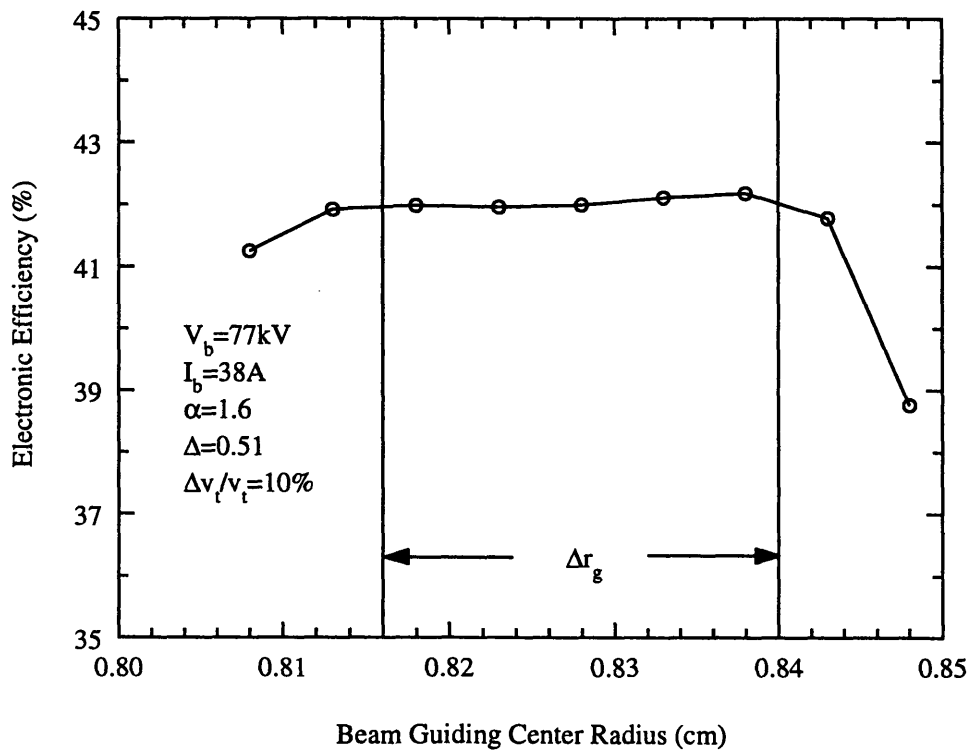
Figure 3.7: Efficiency versus beam radius assuming zero beam thickness.

3.3.1 Mode Competition

Mode competition with the desired TE_{mp1} mode are either azimuthal, radial or axial in nature. Competition from higher axial modes can be safely neglected for the following reason. Higher axial modes TE_{mpq} ($q > 1$) are formed by waves with relatively large group velocities and, accordingly, with relatively weak reflection at the output of the cavity. Analysis [27] shows that the diffractive Q decreases proportional to q^{-2}. Hence axial competition is negligible because Q of the competing TE_{mp2} mode is smaller by a factor of four, with Q of higher radial modes even lower. For example, the quality factors are 1383 for $TE_{28,8,1}$ mode, 285 for $TE_{28,8,2}$ mode, and 140 for $TE_{28,8,3}$ mode as calculated by the cold cavity code.

One effective way to determine which modes are the main competitors with $TE_{28,8}$- mode is to find the starting current of those modes whose frequency lies in the amplification band of electron beam and have coupling coefficients comparable to the coupling coefficient of the $TE_{28,8}$- mode. The amplification band is defined by [40]

$$\Delta \omega_{am} \approx \frac{\pi}{T} \tag{3.2}$$

where T is the transit time of electrons through the resonator. For the assumed electron beam voltage of 77 kV and velocity ratio $\alpha = 1.6$, the amplification band is approximately 3.2 GHz. Because gyrotron operates near cut-off, the frequency of the TE_{mp} mode is approximately given by $f \sim \nu_{mp}c/(2\pi r_w)$, where ν_{mp} is the p-th root of boundary equation for TE_{mp} mode, $J'_m(\nu_{mp}) = 0$, and r_w is the radius of the waveguide. More accurate theoretical frequencies can be obtained by simulating the designed cavity with the cold cavity code. The diffractive quality factors for the cold cavity can also be calculated.

To further distinguish the competing modes, the linear starting current curves are generated using Eq. 2.78 for modes within the amplification band. In Fig 3.8, the starting currents of these modes are plotted as a function of the cavity magnetic field. Beam energy of 77 kV and velocity ratio of 1.6 are assumed in the calculation. The beam radius is chosen at 0.828 cm, which yields maximum coupling for the $TE_{28,8}$- mode. Fig. 3.8 shows that the mode spectrum near the $TE_{28,8}$- mode is dense and that many of the nearby modes couple well to the electron beam and will have practically the same starting requirements as the $TE_{28,8}$- mode. The area

inside the locus of each mode is known as the soft excitation region. The highest efficiency, however, is achieved in the hard excitation region, which lies on the lower magnetic field side slightly beyond the linear starting curve. Oscillation in the hard excitation region has to be initiated by oscillation in the soft excitation region.
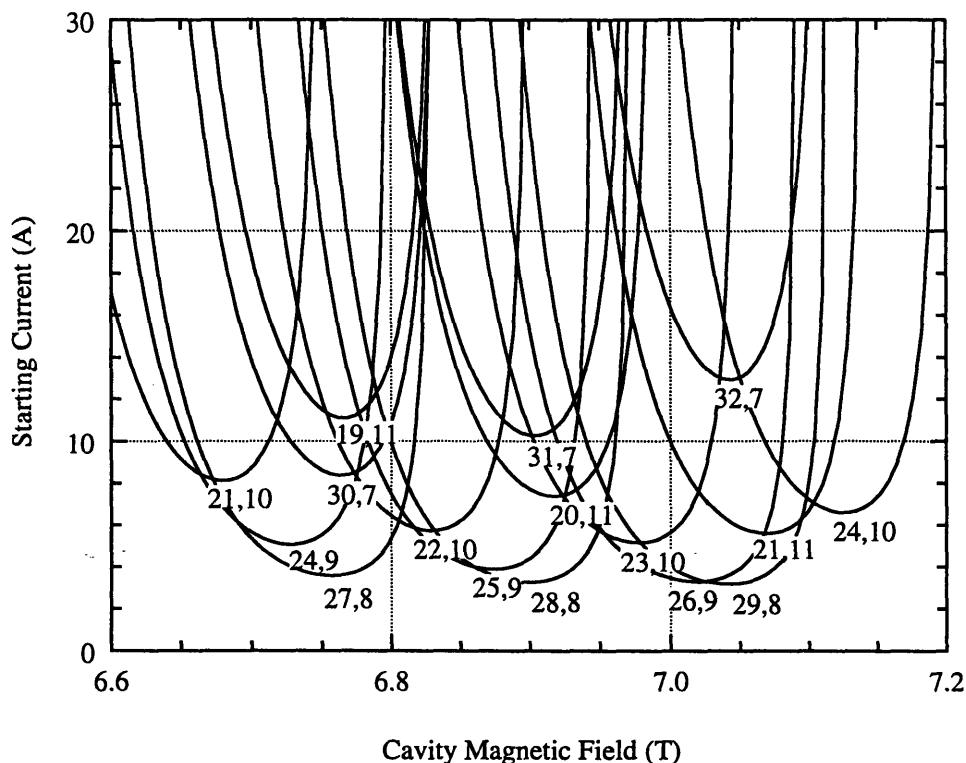
Figure 3.8: Cold-cavity fixed-field starting current versus magnetic field at $V_c = 83\,\text{kV}$ and $\alpha = 1.6$.

Since the quality factors of these competing modes are not significantly different from that of the main mode ($\text{TE}_{28,8}$), the coupling coefficient gives a good estimate of the relative starting current. Fig. 3.9 shows the coupling coefficient C_{mp} defined by Eq. 3.1, as a function of beam radius for different modes. For the $\text{TE}_{28,8}-$ mode, the competition of the radial competing mode $\text{TE}_{25,9+}$ could be reduced by proper positioning of the beam. Azimuthal competing mode, the $\text{TE}_{27,8}-$ mode, however, has almost equal coupling coefficients at the same radial position. In this case, the startup scenario, i.e., the order in which the modes are excited is important since the hard excitation region must be accessed from the soft excitation region. In conclusion, Fig. 3.8 and Fig. 3.9 suggest that the main competing modes for $\text{TE}_{28,8}-$ come from $\text{TE}_{25,9+}$ and $\text{TE}_{27,8}-$ in the high efficiency operating region. In any case, it is necessary

61

to use the multi-mode theory to analyze mode competition problems.
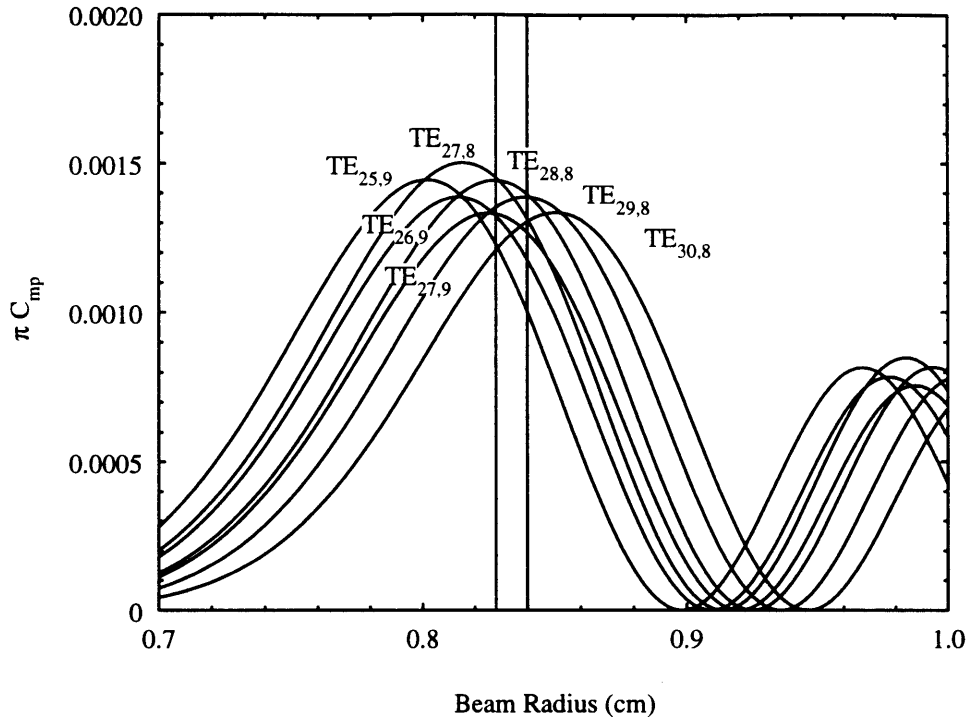
Figure 3.9: Dependence of coupling coefficient for various TE modes on the beam radius.

Performance of the iris cavity was examined with the multimode code MAGY. Result of the multimode simulation confirmed that, except one case, stable, single $TE_{28,8-}$ mode oscillation in steady state can be obtained, with the competing modes oscillating at the noise level. In case where competition between the $TE_{28,8-}$ and $TE_{25,9+}$ modes was considered, the $TE_{25,9+}$ was the surviving mode. To avoid excitation of the $TE_{25,9+}$ mode, the electron beam radius was slightly increased from 0.828 cm to 0.840 cm so that the coupling coefficient of the $TE_{25,9+}$ mode is reduced significantly, while that of the $TE_{28,8-}$ mode remains practically unchanged. Multi-mode simulation shows, for this new beam radius, stable single-mode oscillation is obtained in $TE_{28,8-}$ mode.

The optimum efficiency of the iris cavity is calculated with the multi-mode code for different values of velocity spread. The spread $(\Delta v_\perp/v_{\perp 0})$ is approximated by a Gaussian distribution $f(v_\perp) \sim \exp[-(v_\perp - v_{\perp 0})^2/(2\Delta v_\perp)^2]$. The results are shown in Fig. 3.10. Also shown are the optimum efficiencies predicted by the single-mode code. Comparison shows that mode competition reduces the optimum RF efficiency of the gyrotron by 3-4%. In Sec. 3.4.3 the total

velocity spread of less than 8% is predicted for the designed electron gun. Multi-mode theory predicts RF efficiency of 39% can be achieved with such a spread.
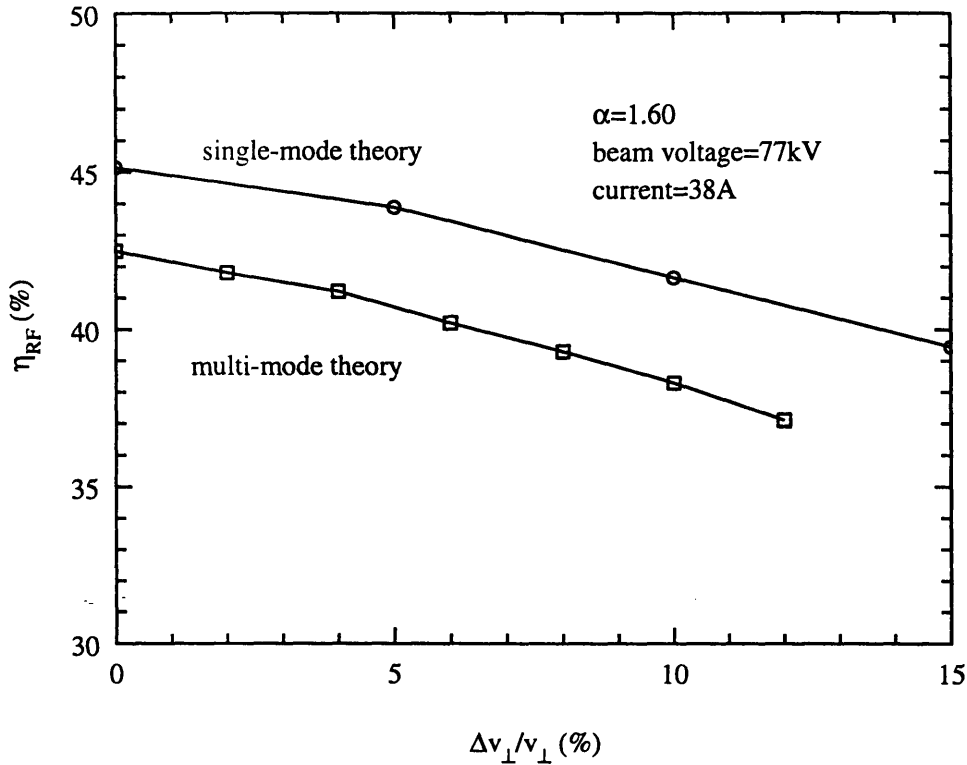
Figure 3.10: Dependence of optimum RF efficiency on the RMS spread of the perpendicular velocities, as predicted by the single-mode code and the multi-mode code.

3.4 Electron Gun

3.4.1 Optimization of Beam Optics

The analytic equations given in Sec. 2.2.1 are used to find a starting point for the gun design. A triode design is selected because it enables us to adjust the velocity ratio by changing the voltage across the cathode and the first anode without changing the beam energy or the beam radius in the interaction region. It also allows the possibility of switching off the beam emission during CW operation by holding the mod-anode at a lower potential from the cathode.

The electron trajectory simulation code EGUN was used to simulate the beam properties.

Typical step size for integration of particle equations of motion, mesh size, and the number of rays used to represent the beam, are 0.2 mesh unit, 0.1 mm, and 48, respectively. Convergence was checked by reducing the particle step size to 0.05 mesh unit, decreasing the mesh size to 0.08 mm, and increasing the number of rays up to 192.
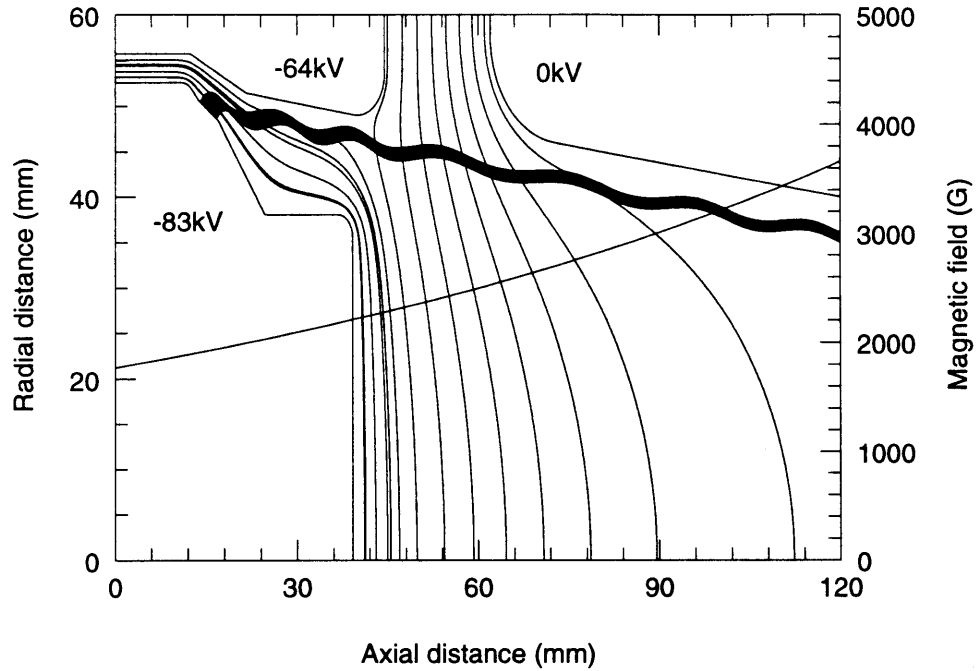
Figure 3.11: Beam trajectories from EGUN simulation.

The geometry of the gun and the electron beam trajectories are shown in Fig. 3.11. To guarantee reliable operation of the gun, the clearance for the beam needs to be sufficiently large to avoid current interception by the mod-anode. The emitter has a relatively large area of $10.8 \, \text{cm}^2$. For beam current of 38 A, the emission density is a modest $3.5 \, \text{A/cm}^2$, about 14% of the Child-Langmuir limiting current density. Thus the gun can be operated in the temperature limited regime and the beam current is adjusted by changing the emitter temperature. The emitter has a large slant angle $\phi_c = 35°$ and produces quasi-laminar flow. The shaping of the electrode surfaces are optimized for low beam velocity spread in the cavity. For the present design, the most critical shaping is that of the nose-piece in front of the emitter. As a result of the optimization, a low perpendicular velocity spread of 2.1% is obtained. Finally the electrode shapes are slightly perturbed around the design point to ensure that minimal machining error would not change drastically the beam characteristics.

Although adiabatic equations generally provide adequate description of the beam characteristics in magnetron injection guns and can be used for the first-cut gun design, it should be noted that often times the beam does not exactly follow the adiabatic rules, especially in a triode-type gun as shown in Fig. 3.11. In a triode-type MIG, the non-adiabatic effects arise due to beam passing the region between the mod-anode and the anode, where the electric field changes direction rapidly during one cyclotron period of the beam, thus violating the conditions for adiabatic approximation given by Eq. 2.86. In this region, depending on the oscillatory phase of the beam, the transverse velocity can be either increased or decreased with respect to its adiabatic value. As a result, the perpendicular velocity $v_\perp$ can not be calculated with Eq. 2.91. In some cases one might even observe relations between parameters predicted by the adiabatic equations being reversed.

Fig. 3.12 shows evolution of the average beam velocity ratio and the perpendicular velocity spread along the axial distance as predicted by EGUN. The emitter is located at the origin $z = 0$ and the cavity is at $z = 53.75$ cm, corresponding to the maximum of the magnetic field. The magnetic field increases from 0.189 T at the cathode to 6.67 T in the cavity. The velocity ratio is defined as $\alpha = v_\perp/v_\parallel$, where $v_\perp$ and $v_\parallel$ are the components of the electron velocity evaluated with respect to the direction of the local magnetic field. The velocity ratio increases due to magnetic field compression, and reaches a maximum value of 1.6 in the cavity region. The velocity spread is calculated as the standard deviation of $v_\perp$ distribution. There is an abrupt increase of spread in the phase mixing region starting at $z = 30$ cm where the beam undergoes transition from a laminar flow to a flow with crossing beam paths. In the mixing region, depending on the oscillatory phase of the electron in the space charge field, the electron will either be accelerated or decelerated in the transverse direction. Velocity spread increases as a result. The spread stays at a constant value of 2.1% after the mixing region. This indicates that the adiabatic theory is valid in the beam tunnel section. The gun design parameters are summarized in Table 3.5.

The axial magnetic field used in EGUN is calculated from ideal coil inputs, which are chosen to fit the axial field produced by EFFI code [41] for the actual coil settings. The off-axis magnetic fields are obtained from a 6-th order expansion of the axial field. A small discrepancy was found between the off-axis field at the cathode calculated by the expansion and
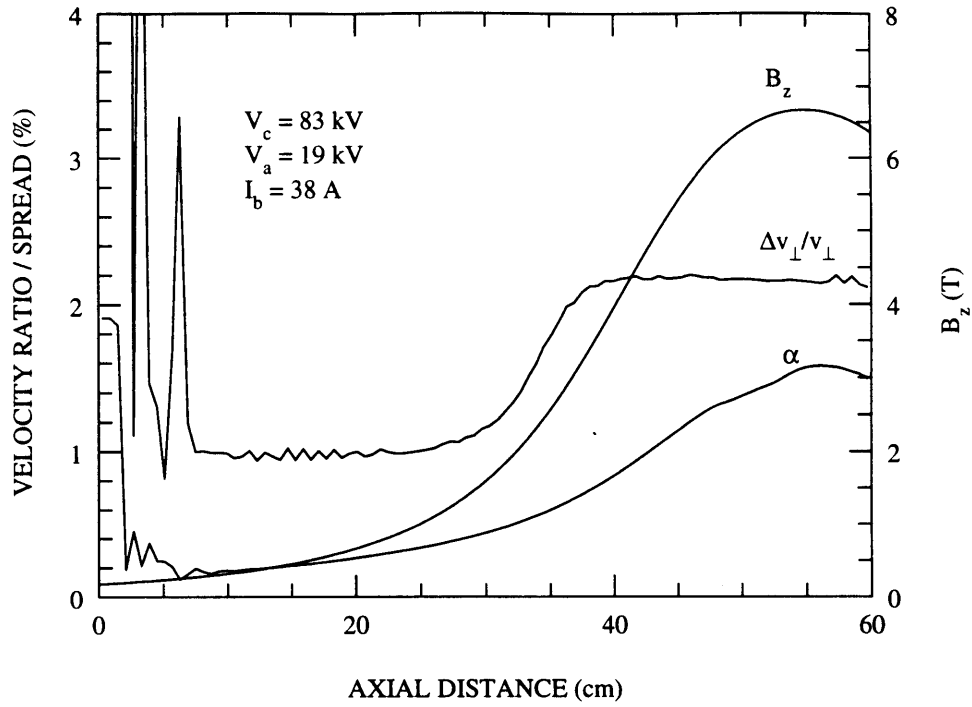
Figure 3.12: Evolution of velocity ratio and perpendicular velocity spread as a function of axial distance.

Average emitter radius r_c	4.95 cm
Emitter width l_c	0.35 cm
Emitter angle ϕ_c	35°
Cathode-anode distance d	0.50 cm
Cathode voltage V_c	83 kV
Mod-anode voltage V_a	19 kV
Beam current I_b	38 A
Limiting current in cavity I_L	74 A
Voltage depression in cavity V_{dep}	6 kV
Velocity ratio in cavity α	1.6
Velocity spread $\Delta v_\perp / v_\perp$ (EGUN)	2.1%
Average beam radius in cavity r_b	0.840 cm
Beam thickness Δr_b	0.05 cm
Emission current density J_c	3.5 A/cm^2
Child-Langmuir current density J_L	24.5 A/cm^2
Magnetic field compression	35

Table 3.5: Design parameters for the electron gun

that predicted by EFFI. However it does not affect the result of EGUN simulation. Measurement of the actual field profile was taken after the superconducting magnet had arrived at MIT. The final gun design was simulated using the actual field profile. A slight shift in the axial location of the gun ($\sim$ 1 cm toward the magnet) was needed to reproduce the simulation results with the initially assumed field profile.

Electric field breakdown is a potential problem for gun operations in long-pulse or CW gyrotrons. A finite-element software ANSYS was used to calculate the static fields inside the gun structure. Electric field on the cathode and anode surfaces are carefully checked to ensure that it does not exceed the acceptable limit of 100 kV/cm. Specifically, the rounded corner behind the cathode emitter tends to be the highest stress point. Sufficiently large radius of curvature for the corner was chosen to reduce the field enhancement factor.

3.4.2 Gun Optimization through Non-Adiabatic Design

The velocity spread ($\Delta v_\perp / v_\perp$) of 2.1% as predicted by EGUN only accounts for optics and self fields in axisymmetric electrostatic fields with electrons emitted at zero initial velocity from a perfectly flat surface. Other factors that would contribute to the spread were previously described in Sec. 2.2.4. Non-axisymmetric magnetic fields can come from the gun not centered or tilted in the tail field of the superconducting magnet, the gun coil not centered or tilted. Non-axisymmetric electric fields can be caused by the cathode not centered or tilted in the mod-anode due to machining error or due to gravity, and azimuthal variations in the current density which would cause different self fields around the emitter. The cathode emitter also moves when it heats up and may move away from its expected position. All of these are potential causes of initial spread, and may not be completely eliminated in the actual experiment.

One way to minimize the velocity spread caused by these non-ideal effects is to build a non-adiabatic gun with beam characteristics less sensitive to the operating parameters. As mentioned previously, non-adiabatic effects arise due to beam passing the region between the mod-anode and the anode. It was observed that by changing the axial location of the anode, the non-adiabatic behavior of the beam can be altered.

To optimize the gun design, the sensitivity of beam characteristics to variations in the operating parameters are studied. Fig. 3.13 and Fig. 3.14 show examples of the optimization

67

process. In the first case, variation of magnetic field azimuthally around the emitter is considered. In Fig. 3.13, dependence of the beam velocity ratio α on the cathode magnetic field is shown for three gun designs. The difference between these three designs is the axial location of the anode. Here the variation in the cathode magnetic field is achieved by moving the gun to different axial locations relative to the magnet. As shown, all three designs can achieve the desired α value of 1.6 with low velocity spread of 2.1%. However, the design with α less sensitive to the cathode magnetic field was chosen. For this design a slight variation of magnetic field azimuthally around the emitter would result in a smaller variation of α, and therefore a lower beam velocity spread. Also shown in Fig. 3.13 is the predicted α based on the adiabatic theory. Clearly adiabatic theory inadequately explains the dependence of α on the cathode field, especially for cathode field below 0.185 T.
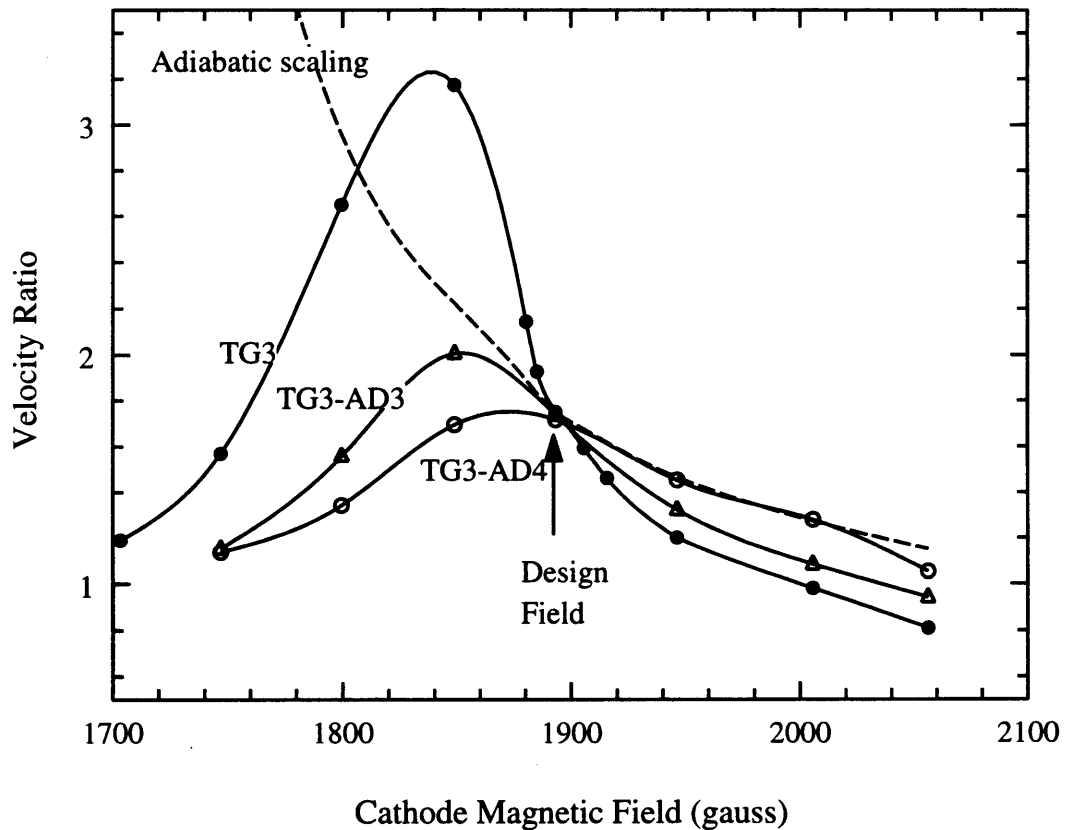
Figure 3.13: Sensitivity of velocity ratio to cathode magnetic field.

Further study was done for sensitivity to the mod-anode voltage. In Fig.3.14, velocity

ratio is plotted as a function of the mod-anode voltage for each design. Again the final design TG3-AD4 is the least sensitive to the variation of mod-anode voltage. For this design, a slight variation in electric field around the emitter would result in a smaller variation of α, and therefore a lower beam velocity spread. Such variations in electric field can be due to a radial offset of the cathode axis and the mod-anode axis. Although a design with even lower sensitivity is possible, the choice is dictated by the need to achieve sufficiently high α within the electric field stress limit.
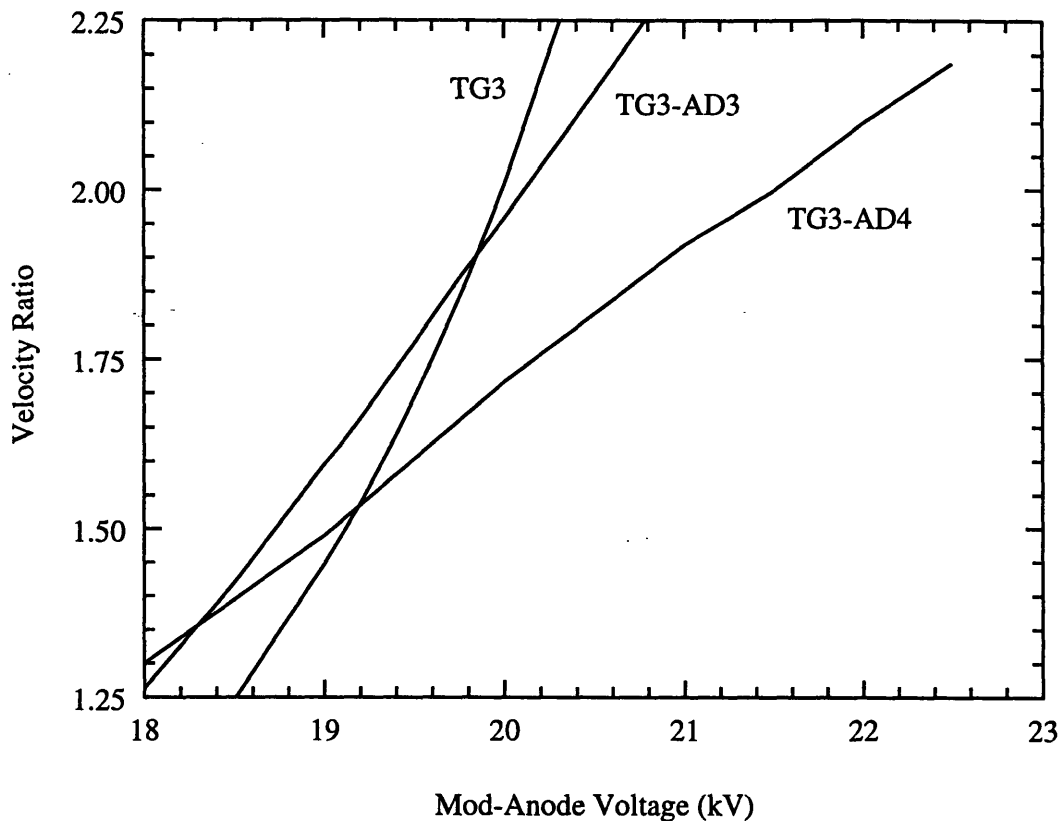
Figure 3.14: Sensitivity of velocity ratio to mod-anode voltage.

Also simulated is the evolution of the velocity ratio during the rise of the cathode voltage. This is of particular interest for the study of startup scenario. In the present pulsed experiment, the voltage on the mod-anode is provided by a resistive divider from the cathode voltage so that the ratio V_a/V_c is held at a fixed value during the voltage rise. In Fig. 3.15, velocity ratio is plotted as a function of cathode voltage with constant V_a/V_c which provides α of 1.6 at

$V_c = 83$ kV. Comparison shows that, for the final design TG3-AD4, the velocity ratio is stable against fluctuation of the cathode voltage near the design point. The implication of this feature needs further study at this point. For example, we need to study how the stability of oscillation in the design mode could be affected by a slight over-shooting of the cathode voltage.
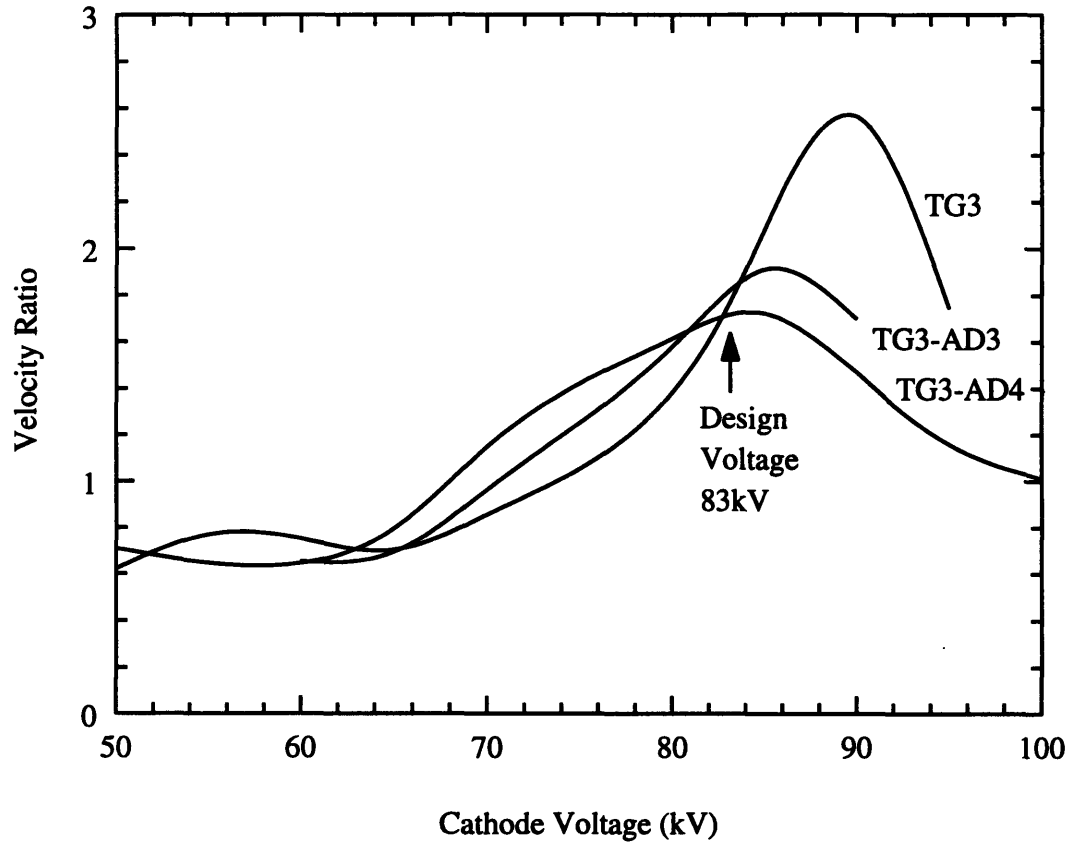
Figure 3.15: Evolution of α during the rise of cathode voltage.

3.4.3 Theoretical Estimate of Velocity Spreads

A simple algorithm is introduced to estimate the final velocity in the interaction region from the spread in initial velocity based on the non-adiabatic behavior of the beam flow. It will be shown that as a result of designing certain non-adiabatic guns, spreads due to non-ideal conditions at the cathode can be reduced. The result further explains why the above process of designing a gun with beam characteristics less sensitive to the operating parameters would lead to low velocity spread.

The perpendicular velocity $v_\perp$ in the cavity can be written as a function of the initial velocity

at the emitter $v_{\perp c}$ and the compression ratio,

$$v_\perp = \frac{v_{\perp c}}{\gamma} \sqrt{\frac{B_0}{B_c}} K(v_{\perp c}). \tag{3.3}$$

This is a variation of the adiabatic equation of Eq. 2.91. The additional parameter $K(v_{\perp c})$, which is a function characteristic of a specific gun design, is introduced to characterize the non-adiabatic behavior. For an adiabatic beam, $K(v_{\perp c}) = 1$. To obtain $K(v_{\perp c})$ for a gun design, the initial velocity is calculated with Eq. 2.89, while the final velocity $v_\perp$ is determined from numerical simulation with EGUN. The variation in $v_{\perp c}$ for EGUN simulation can be achieved by changing either the mod-anode voltage or the cathode magnetic field. Fig. 3.16 shows $K(v_{\perp c})$ as functions of $v_{\perp c}$ for two different gun designs mentioned in the previous section. The horizontal axis is normalized to $v_{\perp c0}$, which is the initial velocity that results in α of 1.6 in the cavity for both gun designs, and is $0.0634c$ for TG3-AD4 and $0.0639c$ for TG3. The dashed lines were obtained by varying the cathode magnetic field, and the continuous lines by changing the mod-anode voltage. The difference between the two sets of curves is due to the fact that the oscillatory phase of the beam reaching the non-adiabatic region depends not only on the amplitude of the initial velocity, but also on the details of the magnetic field along the beam path.

The effect of the non-adiabatic behavior of the beam on the velocity spread can be understood from the following argument. Suppose a small additional spread $(\Delta v_{\perp c}/v_{\perp c})_i$ is introduced to the initial velocity, and assume that this additional spread does not affect uniform space charge effect in the mixing region. For an adiabatic beam, or one with a constant $K(v_{\perp c})$, the additional spread is a constant of motion and will not change along the beam path. The effect of a non-constant $K(v_{\perp c})$ is that it will either increase or decrease the additional spread. Consider an ensemble of electrons distributed between initial velocity $v_{\perp c} - \Delta v_{\perp c}$ and $v_{\perp c} + \Delta v_{\perp c}$. For the TG3-AD4 design, $dK(v_{\perp c})/dv_{\perp c} < 0$, thus the electrons with smaller initial velocity grow faster than the ones with larger initial velocity. The result is a lower spread in the interaction region compared to that of an adiabatic gun. The opposite effect can be expected for the TG3 gun design which has $dK(v_{\perp c})/dv_{\perp c} > 0$.

Assuming that $K(v_{\perp c})$ is a linear function of $v_{\perp c}$ near $v_{\perp c0}$, which is a good approximation

71
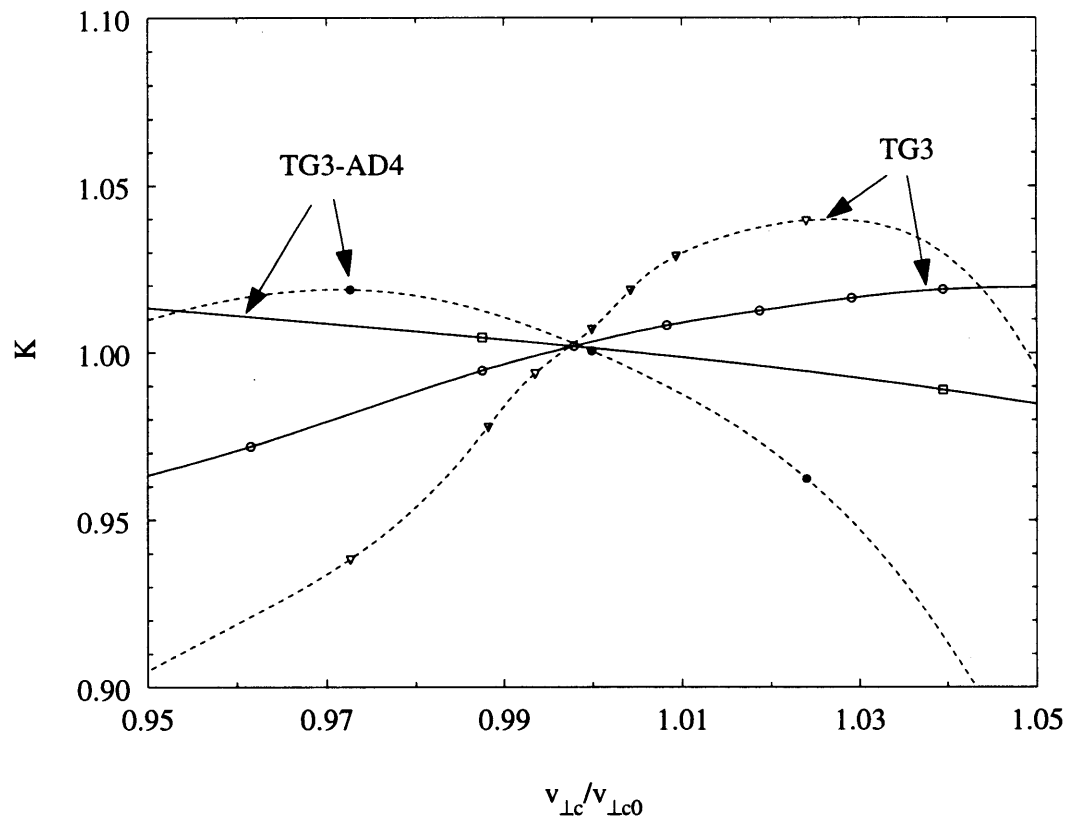
Figure 3.16: Non-adiabaticity parameter $K(v_{\perp c})$ as a function of $v_{\perp c}/v_{\perp c0}$, where $v_{\perp c0}$ is the initial velocity at the designed operating point.

for small initial spread, and let $K_1 = K(v_{\perp c} + \Delta v_{\perp c})$ and $K_2 = K(v_{\perp c} - \Delta v_{\perp c})$, then the final spread can be calculated as

$$
\begin{aligned}
\left(\frac{\Delta v_\perp}{v_\perp}\right) &= \frac{K_1 - K_2}{K_1 + K_2} + \left(\frac{\Delta v_{\perp c}}{v_{\perp c}}\right) \\
&\approx \left(1 + v_{\perp c}\frac{dK}{dv_{\perp c}}\right)\left(\frac{\Delta v_{\perp c}}{v_{\perp c}}\right).
\end{aligned}
\tag{3.4}
$$

Once the function $K(v_{\perp c})$ is obtained for a gun design, and the cause of initial spread is determined, the final spread can be calculated using Eq. 3.4. As mentioned in Sec. 2.2.4, there are several factors that cause initial velocity spread at the cathode. These factors are analyzed separately as below.

(i) Non-symmetric *magnetic* field

Non-symmetric magnetic field around the cathode emitter is caused by either a tilt or a radial offset of the gun axis with respect to the magnetic field axis. To first order in small tilt and offset, the field variation can generally be written as

$$
B_c(\theta) = B_{c0}\left[1 + \left(a_1\frac{\delta r_s}{r_c} + a_2\delta\varphi\right)\cos\theta\right],
\tag{3.5}
$$

where B_{c0}, a_1 and a_2 can be found from field simulation using the EFFI code. The initial velocity $v_{\perp c}$ as a function of the azimuthal angle θ can then be found in terms of δr_s and $\delta\varphi$ by combining Eq. 2.89 and Eq. 3.5 and expand to first order as

$$
v_{\perp c}(\theta) = v_{\perp c0}\left[1 - \left(a_1\frac{\delta r_s}{r_c} + a_2\delta\varphi\right)\cos\theta\right].
\tag{3.6}
$$

Here $v_{\perp c0}$ is the initial velocity for the case of no tilt or offset. The spread can be easily calculated from the standard deviation of the distribution as,

$$
(\Delta v_{\perp c})_B = \frac{1}{\sqrt{2}}\left(a_1\frac{\delta r_s}{r_c} + a_2\delta\varphi\right)v_{\perp c0}.
\tag{3.7}
$$

The initial spread $(\Delta v_{\perp c})_B$ can be evaluated using Eq. 3.7 for a given tilt angle or radial

73

offset. Substitute $(\Delta v_{\perp c})_B$ into Eq. 3.4 in place of $(\Delta v_{\perp c})$ and find the corresponding values of K from the dashed curves in Fig. 3.16, the final spread in the cavity due to non-symmetric magnetic field can be obtained.

For the present gun design, $B_{c0} = 0.1845\,\text{T}$, a_1 and a_2 are calculated from EFFI to be 0.050 and 0.265, respectively. For realistic values of $\delta r_s = 0.2\,\text{cm}$ and $\delta\phi = 1° = 0.017\,\text{rad}$, the initial spread is 0.5%, and the final spreads are 0.4% for TG3-AD4, and 0.8% for TG3.

(ii) Non-symmetric *electric* field

Non-symmetric electric field can be created by a radial offset of the cathode axis and the mod-anode axis. Although such an offset can be eliminated by careful machining, operating the gun in a horizontal position could cause sagging of the cathode since the cathode is only supported at the back. An offset of 0.2 mm was actually measured by CPI in a gun previously operated at MIT.

The electric field at the emitter surface is given by Eq. 2.90. Assuming $d \ll r_c$, $\delta r_m \ll d$, the azimuthal variation of the electric field at the cathode for a radial offset δr_m can be written as

$$E_c(\theta) = E_{c0}\left(1 - \cos\phi_c \frac{\delta r_m}{d} \cos\theta\right), \tag{3.8}$$

where E_{c0} corresponds to the field for zero offset case. The spread in initial velocity can be derived similar to Eq. 3.7 as

$$(\Delta v_{\perp c})_E = \frac{\cos\phi_c}{\sqrt{2}}\left(\frac{\delta r_m}{d}\right)v_{\perp c0}. \tag{3.9}$$

In the present gun design, $d = 5\,\text{mm}$, $\phi_c = 35°$. For a realistic value of $\delta r_m = 0.2\,\text{mm}$, the initial spread introduced by the offset is 2.3%. Use Eq. 3.4 and find the corresponding values of K from the continuous curves in Fig. 3.16, the final spreads are estimated to be 1.7% for TG3-AD4 and 3.6% for TG3.

The estimation of spreads due to non-axisymmetric magnetic and electric fields is based on the assumption that the electron trajectories do not experience large change of the azimuthal

angle. This assumption is valid in the present design because the $\mathbf{E} \times \mathbf{B}$ drift of the beam in the gun region amounts to approximately 15° change of the azimuthal angle.

(iii) Thermal spread and surface roughness

The effect of temperature and surface roughness of the emitter of a magnetron injection gun has been studied previously by researchers in Russia [42]. With a thermionic cathode, the electrons emitted from the cathode surface have slightly different initial velocities due to the thermal spread. The temperature induced velocity spread is given by

$$(\Delta v_{\perp c})_T = \left(\frac{k_B T_c}{m}\right)^{1/2}, \tag{3.10}$$

where T_c is the cathode temperature in Kelvin, k_B is the Boltzmann constant. The normal operating temperature of a thermionic cathode is around $1300\,\text{K}$. Therefore the initial thermal spread is 0.7%. Again use Eq. 3.4 and find the corresponding values of K from the continuous curves in Fig. 3.16, the final spread in TG3-AD4 and TG3 will be 0.5% and 1.1%, respectively.

The roughness of the emitter surface also affects the velocity spread. For a roughness with the shape of a hemisphere, electrons emitted from different parts of the hemisphere experience different accelerating fields initially. This induces a spread in initial velocities similar to the thermal spread. It is estimated to be

$$(\Delta v_\perp)_R = \left(\frac{0.3 e h E_c}{m}\right)^{1/2}, \tag{3.11}$$

where E_c is the cathode electric field, and h is the radius of a small hemispherical bump on the cathode surface which is representative of the cathode roughness dimension. The factor 0.3 can vary depending on the assumed bump shape, and can be as high as 0.6 for a cone shaped bump [43]. A typical hemispherical bump size of $3\,\mu\text{m}$ and $E_c = 50\,\text{kV/cm}$ will result in an initial spread of 4.0%. Therefore the final spread is 2.9% in TG3-AD4 and is 6.3% in TG3.

Velocity spread is examined using EGUN for different beam current. The increase in spread is mainly due to enhanced space charge effects during the mixing, rather than the thermal spread from higher cathode temperature. As shown in Fig. 3.17, $\Delta v_\perp / v_\perp$ increases from 1.4% at $10\,\text{A}$

beam current to 2.5% at 50 A, and to 4.3% at 75 A at which point the limiting current is reached. A slight decrease in the velocity ratio is due to the increased space charge near the emitter surface that reduces the cathode electric field.

Previous study showed that the cathode emission density can have an azimuthal variation as much as ±30% of the average value. This would create a variation in velocity ratio for electrons emitted from different azimuthal locations due to the space charge near the emitter. A total spread can be estimated by averaging the velocity values at different currents, for example, from Fig. 3.17. The result shows that the spread due to the nonuniform emission is a relatively small value of ~ 0.3%.
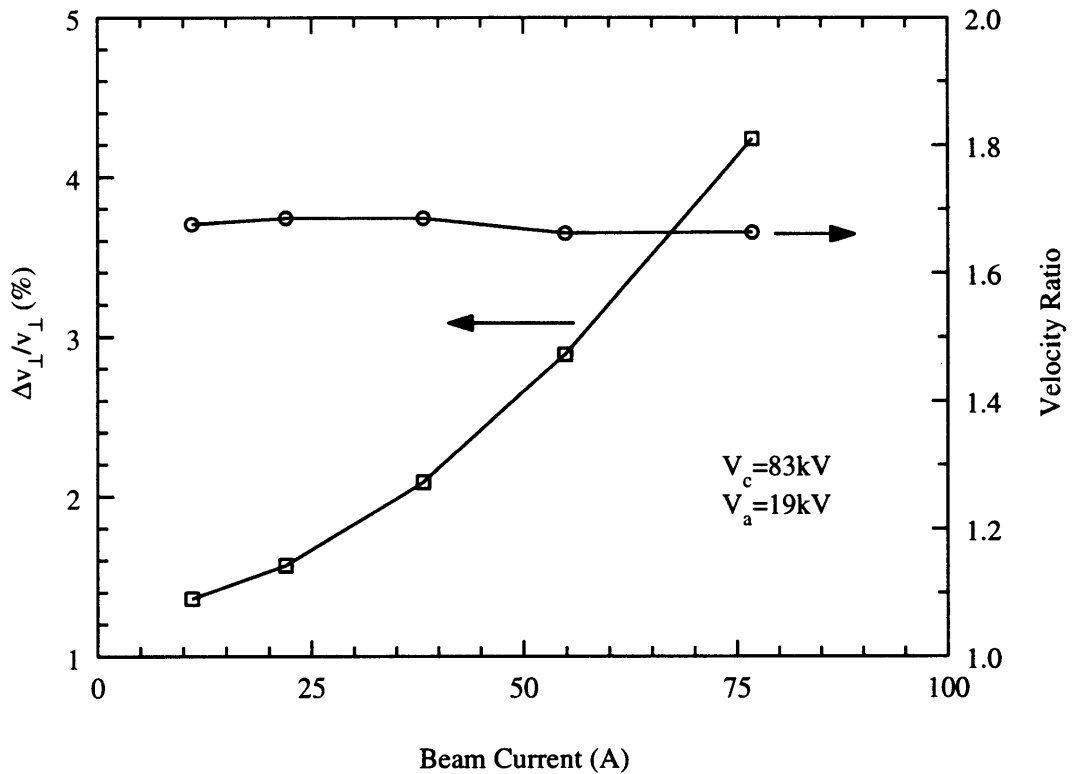
Figure 3.17: Velocity spread as a function of beam current.

The contributions to velocity spread from all sources are summarized in Table 3.6. A total spread of 4% is estimated for the final gun design with realistic values of emitter temperature, surface roughness, tilt and offsets. Surface roughness is the top contributor followed by beam optics and radial offset of cathode and mod-anode axes. The total spread is calculated with Eq. 2.110 as the statistical sum. For the present gun design (TG3-AD4), even with twice the

	TG3-AD4	Adiabatic	TG3
Beam optics	2.1	2.1	2.1
Gun tilt and offset (1° and 2 mm)	0.4	0.5	0.8
Cathode mod-anode offset (0.2 mm)	1.7	2.3	3.6
Thermal spread (1300 K)	0.5	0.7	1.1
Surface roughness (3 μm)	2.9	4.0	6.3
Nonuniform emission (30% variation)	0.2	0.3	0.4
Total spread	4.0	5.2	7.7

Table 3.6: Comparison of estimated total velocity spread in percent for the final gun design TG3-AD4, the adiabatic design, and TG3 design.

added spread, velocity spread less than 8% should be possible. The analysis result shows that a low-sensitivity non-adiabatic gun design significantly reduces the total velocity spread of the beam. It also reminds us that a sensitivity study must be done to avoid building a gun with the features of TG3 gun, although EGUN simulation shows the same beam characteristics can be achieved. The reduction in spread is particularly meaningful if the initial spread is above 10-15% since such a large spread will result in a significant decrease of the gyrotron efficiency.

3.5 Internal Mode Converter System

In order to efficiently transmit the RF wave generated by megawatt gyrotrons to fusion plasma, a mode converter is generally used to converter the TE mode to a Gaussian-like beam. Radial output coupling of the RF power of a gyrotron into a Gaussian mode has three significant advantages for high-power operation. First, the Gaussian beam is directly usable for low-loss transmission as well as for effective interaction with the fusion plasma and no further mode converters are needed. Second the converter separates the electron beam from the RF wave path, so that the electron collector is no longer part of the output waveguide as in the case of a tube with an axial output. Hence the collector can be designed especially for handling the high electron beam power. In addition, energy recovery with depressed collector becomes possible. Third, the influence of RF power reflected from the output window is expected to be significantly reduced. Dimpled wall converters are employed because they have the advantage of high conversion efficiency (95%) and small physical size [44].

r_0	1.807 cm
l_1	3
l_2	1
$\epsilon_1 = \epsilon_2$	2.1×10^{-3} cm
β_1	-0.339 cm^{-1}
β_2	-1.871 cm^{-1}
Length	19.4 cm

Table 3.7: Design parameters for the dimpled-wall waveguide.

3.5.1 Dimpled Wall Launcher

The converter consists of a dimpled-wall launcher section with a stepcut launching aperture followed by several mirrors in an open-space transmission line for beam steering and profile shaping. The purpose of the dimpled-wall launcher is to produce a mode mix in the launching waveguide such that the field intensity on the wall has a Gaussian profile. This favorable mode mix is achieved by converting power from the input mode to several selected satellite modes $TX_{mi,pi}$, which can be either TE or TM modes. To obtain this type of mode conversion, the waveguide wall is perturbed to have a helicoidal wall profile, described by the following equation,

$$r(\phi, z) = r_0[1 + \epsilon_1(z) \cos(\beta_1 z - l_1 \phi) + \epsilon_2(z) \cos(\beta_2 z - l_2 \phi)], \qquad (3.12)$$

where $\beta_1 \sim \pm(\beta_0 - \beta_i)$, $l_1 = \pm(m_0 - m_i)$, $\beta_2 \sim \pm(\beta_0 - \beta_j)$, $l_2 = \pm(m_0 - m_j)$. The subscript 0 corresponds to the input mode, $TE_{28,8}$, and the subscripts i and j refer to the first and second satellite modes. The design parameters for the launcher are summarized in Table 3.7.

The analysis of the rippled wall waveguide was carried out using coupled mode theory. In addition to the four selected satellite modes, all other modes that can couple through the wall perturbations are considered in the coupled mode analysis. A total of 25 modes were included in the analysis based on the coupling. Fig. 3.18 shows the evolution of power in the main satellite mode as a function of axial distance. Beginning with 100% power in the input mode, more than 50% power is converted into four main satellite modes. Fig. 3.19 shows the resulting Gaussian wall current profile. A distinct, well-shaped beam is indicated. The Gaussian wall current profile has a peak to valley ratio of approximately 25, indicating minimal power outside

78

the beam. The irregular waveguide section is 19.4 cm long. The radiation is launched from the rippled wall section by cutting the waveguide wall around one Gaussian bunch where the wall currents are at a minimum, which virtually eliminates edge diffraction effects.
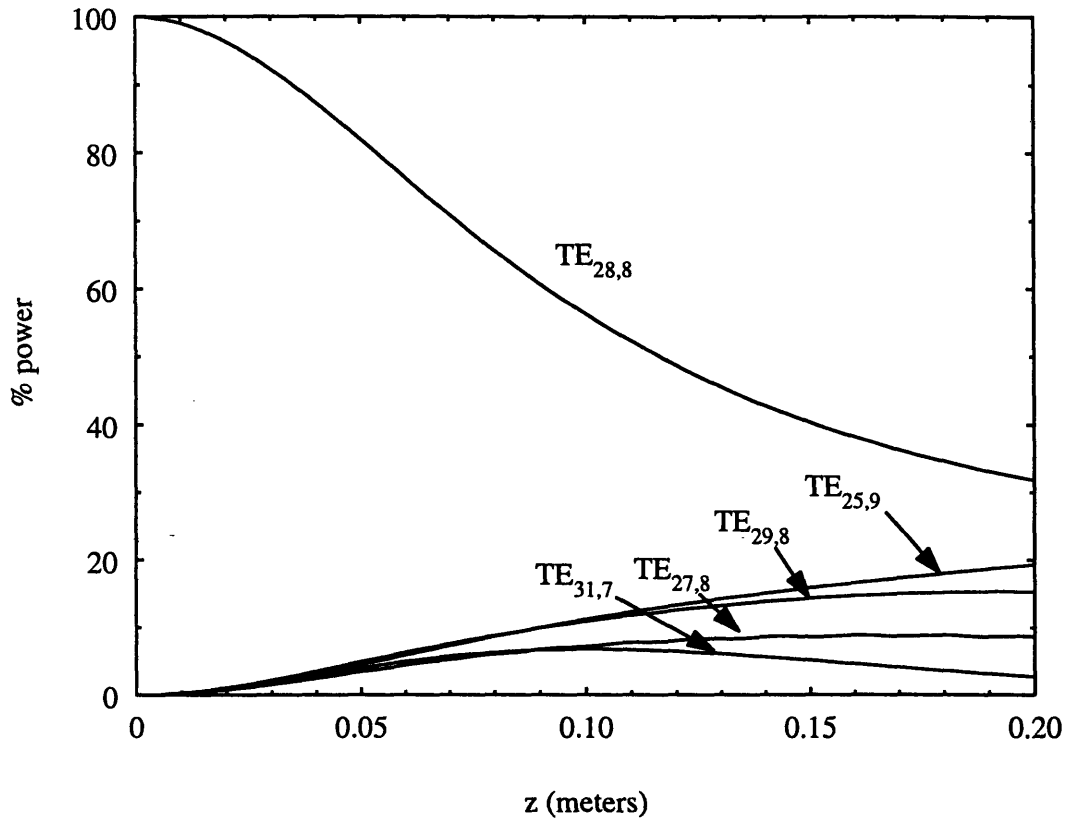
Figure 3.18: Evolution of power in modes in the dimpled wall launcher.

3.5.2 Four-Mirror Transmission Line

The launcher and open mirror transmission line are shown in Fig. 3.20. The purpose of the open mirror transmission line is to provide steering and profile shaping for the beam radiated from the launcher. The Stratton-Chu diffraction theory, a vector formulation of Huygen's principle, was used to simulate the launch and to predict the behavior of the beam as it propagates from the launcher into free space. The theoretical beam expansion was compared to that of an elliptic Gaussian beam and good agreement was obtained. Therefore, the preliminary design of the focusing mirrors can be made using Gaussian optics theory. The elliptic beam is focused to
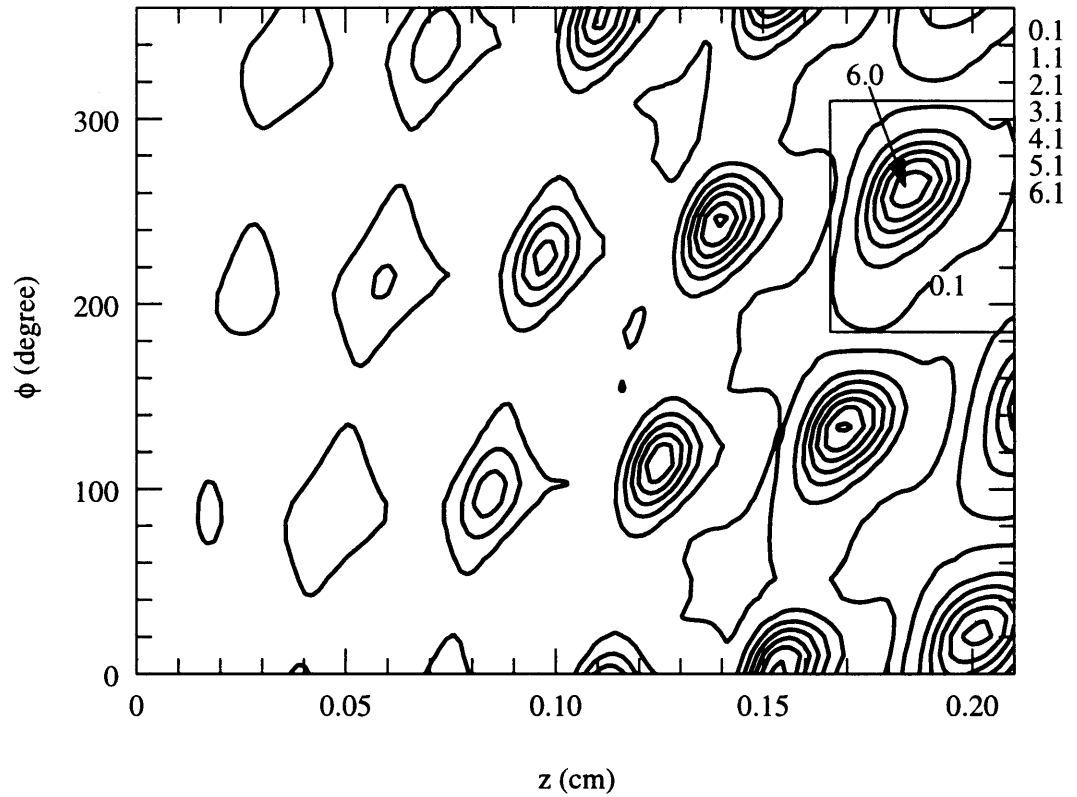
Figure 3.19: Intensity of the surface currents on the inside walls of the launcher. The contours represent the ratio of the local wall current to the current at the beginning of the launcher. The contours are plotted as a function of the axial distance z and the azimuthal angle ϕ.
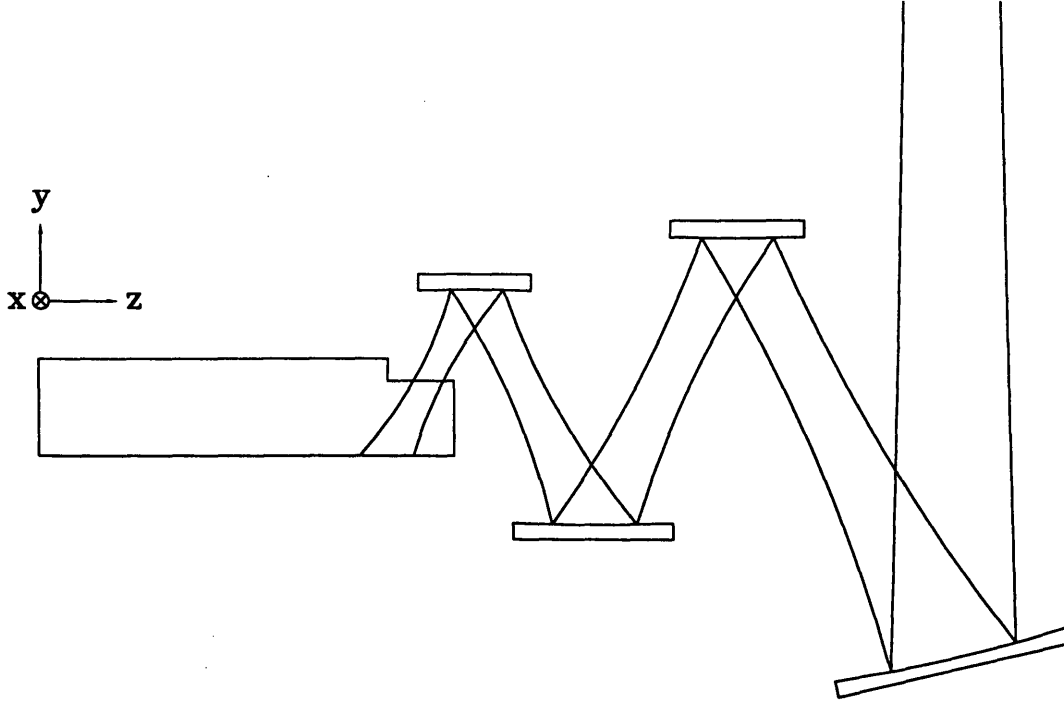
Figure 3.20: Schematic of launcher and mirror transmission line.

a circular fundamental Gaussian beam with four toroidally shaped mirrors with the surface profile given by

$$y = \pm \left(-z^2 + \left[R_z - R_x + \sqrt{R_x^2 - x^2} \right]^2 \right)^{1/2}. \qquad (3.13)$$

With the input and desired output beam waists known, the Gaussian optics q-parameter [45] was used to determine the radii of curvature in the vertical and horizontal directions, R_x and R_z, respectively. Stratton-Chu diffraction theory was used to simulate RF beam propagation through the four-mirror relay to the output window. The preliminary Gaussian optics design is refined to obtain a desired field profile at the window. The resulting mirror design parameters are summarized in Table 3.8. The calculated field pattern at the window is shown in Fig. 3.21.

3.6 Electron Beam Tunnel

The drift region between the gun and the cavity contains slotted structures to prevent spurious oscillations. The profile of the structure is chosen such that the beam radius is 0.7 of the wall

81

	R_z	R_x	y_0	x_0
Mirror 1	27.48	11.50	5.20	18.94
Mirror 2	254.47	-148.61	-5.30	24.75
Mirror 3	-37.20	-307.58	8.12	33.47
Mirror 4	61.68	-314.00	-8.65	44.36

Table 3.8: Design parameters for the 4-mirror transmission line. All units are in cm. Negative radius of curvature indicates mirror shape in that direction is convex.
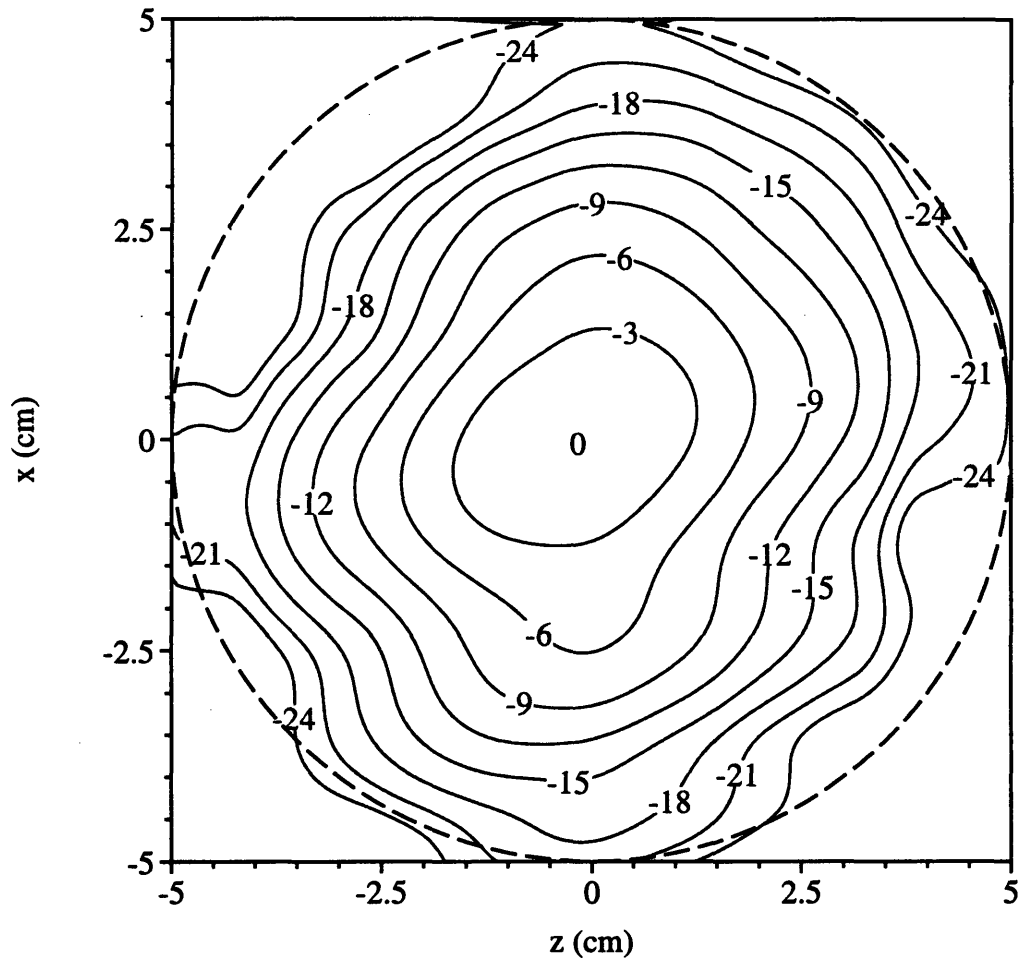
Figure 3.21: Calculated $|E_x|^2$ in decibel at the 10 cm diameter output window. The dashed line in the plot represents the boundary of the window.

radius. In addition, there is a section 5 cm long just before the cavity consisting of alternating copper and Ceralloy rings that absorb any power leaking from the cavity that could reach the cathode region and disrupt gun operation.

3.7 Output Window

Dielectric output windows are widely used in vacuum microwave devices to separate the vacuum volume and the outer space. For devices like gyrotrons operating at high powers and high frequencies, the problem of window elaboration is very important. The window has to be made of material with low losses and high thermal conductivity and the window unit must provide low scattering of the mode transmitted through the window. At 110 GHz, power limit is about 500 kW CW using a double disk sapphire window, and this is a critical problem facing high power CW gyrotrons. There are worldwide efforts directed toward research in the area of window design. In this section, however, only general properties of windows used in pulsed gyrotron experiments are discussed.

The simplest output window model is a dielectric plate with thickness d and permittivity ϵ, which is assumed to be real. Since the coupling between transversal guide modes is absent, the window works like a simple Fabry-Perot interferometer and the reflection and transmission coefficients depend on the plate thickness periodically [46],

$$|R|^2 = \frac{(1 - \gamma_r)^2 \sin^2 \chi}{4\gamma_r \cos^2 \chi + (1 + \gamma_r)^2 \sin^2 \chi},$$

where $\gamma_r = (\epsilon_r - \sin^2 \Theta_B)/\cos^2 \Theta_B$, $\chi = (\omega/c)d\sqrt{\epsilon_r - \sin^2 \Theta_B}$, and $\Theta_B = \tan^{-1}(k_\perp/k_\parallel)$ is the Brillouin angle of wave in the waveguide. It is apparent from the above equations that when the plate thickness d is equal to half-integer number of longitudinal wavelengths in the dielectric, it is possible to obtain zero reflection.

The window used in the initial operation is made of UV-grade fused silica, with $\varepsilon_r = 3.8267$, and a thickness of $d = 0.391$ cm. The radius of the waveguide in the vacuum is 2.223 cm. Fig. 3.22 shows the power reflection coefficient versus frequency. This shows that there is no reflection at 170.1 GHz for the $TE_{28,8}$ mode, but there will be approximately 25% power

reflection for both the TE$_{27,8}$ mode at 166.6 GHz and the TE$_{29,8}$ mode at 173.5 GHz. The effect of the power reflection on the operation of gyrotron will be discussed in Sec. 4.1.5.
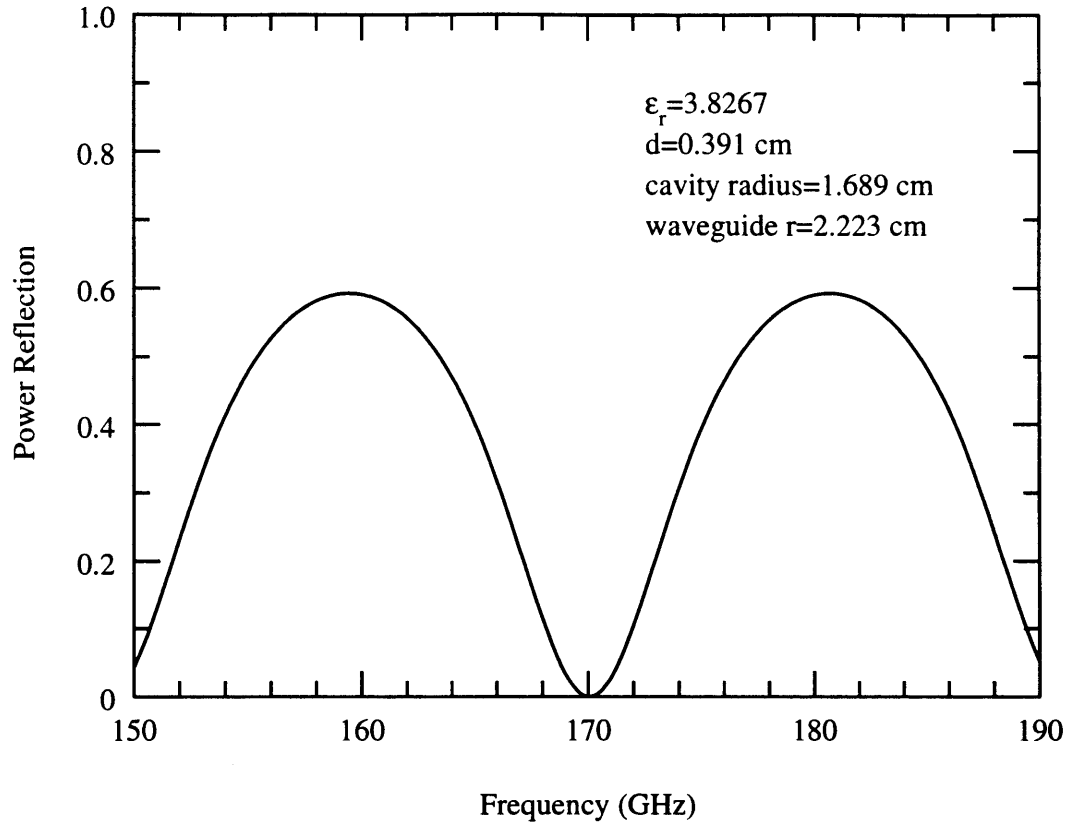
Figure 3.22: Window power transmission versus frequency for a 0.3912cm thick fused silica window

Even for zero reflection, not all the power is transmitted through the window. The power absorption of the window is approximately given by

$$\frac{dP}{dz} = -P\frac{k^2\varepsilon_r \tan\delta}{k_z} \tag{3.14}$$

where k_z is the z component of the wavevector in the window, and δ is the loss tangent of the window material. For fused silica at 170 GHz, $\tan\delta = 13.5 \times 10^{-4}$ [47]. Thus during the initial experiment, the power absorption in the window is 3.9% of the incident power.

3.8 RF Power Losses in Waveguide

For TE cylindrical waveguide mode with fields in the form of Eq. 2.81 and profile function $f(z) = e^{-ik_z z}$ of a forward propagating wave, the power flow in the waveguide is given by [26]

$$
\begin{aligned}
P_{rf} &= \frac{1}{2\mu_0} \int_a |\mathbf{E} \times \mathbf{B}^*|\, da \\
&= \frac{\pi k_z}{4\mu_0 \omega k_\perp^2}(\nu_{mp}^2 - p^2) J_m^2(\nu_{mp}) E_0^2
\end{aligned}
\tag{3.15}
$$

Comparing Eq. 3.15 with the ohmic density given by Eq. 2.82, these two quantities can be related as,

$$
\frac{\rho_{ohm}}{P_{rf}} = \sqrt{\frac{2}{\mu_0 \omega \sigma}} \frac{k_\perp^4}{\pi k_z} \frac{1}{(\nu_{mp}^2 - p^2)}\left(1 + \frac{m^2 k_z^2}{\nu_{mp}^2 k_\perp^2}\right)
\tag{3.16}
$$

In the initial experiment, the straight waveguide which propagates the power from the cavity to the window has a radius of 2.223 cm and a length of 78 cm. The ohmic loss in this waveguide is calculated to be 4.4% of the initial power based on Eq. 3.16. Including the ohmic losses in the cavity of 2.2%, plus the absorption by the window of 3.9%, the final power out of the window would be 89% of the power generated in the cavity.

Chapter 4

Experimental Results

In this chapter, the results from the pulsed gyrotron oscillator experiment at MIT are presented. Measurement techniques are described. Detailed analysis will be given for power and efficiency measurement, velocity ratio measurement, construction of a mode map, startup measurement, estimate of velocity spread from reflected current measurement, and finally some preliminary result from the external testing of the dimpled wall launcher.

4.1 Initial Gyrotron Operation

Although the overall goal of the MIT program is to investigate the gyrotron configuration as shown in Fig. 3.1, the initial experiments were conducted without the internal mode converter. The experimental configuration is shown in Fig. 4.1. The objectives of these experiments were to optimize the cavity performance, to investigate the electron beam characteristics, and to determine if mode competition was adversely affecting the operation of the cavity. The measurement results would be easier to interpret with this configuration. The RF power generated by the cavity was propagated by a 2.223 cm radius cylindrical copper waveguide along the tube axis to a fused silica vacuum window. The waveguide also serves as the collector for the electron beam. In addition, launching of the TE mode through the output window also enables us to determine the performance and to align the mode converter externally. A picture of the experimental setup is shown in Fig. 4.2.

The magnetron injection gun is energized by a modulator capable of producing up to 150 kV,

86

ITER GYROTRON EXPERIMENT
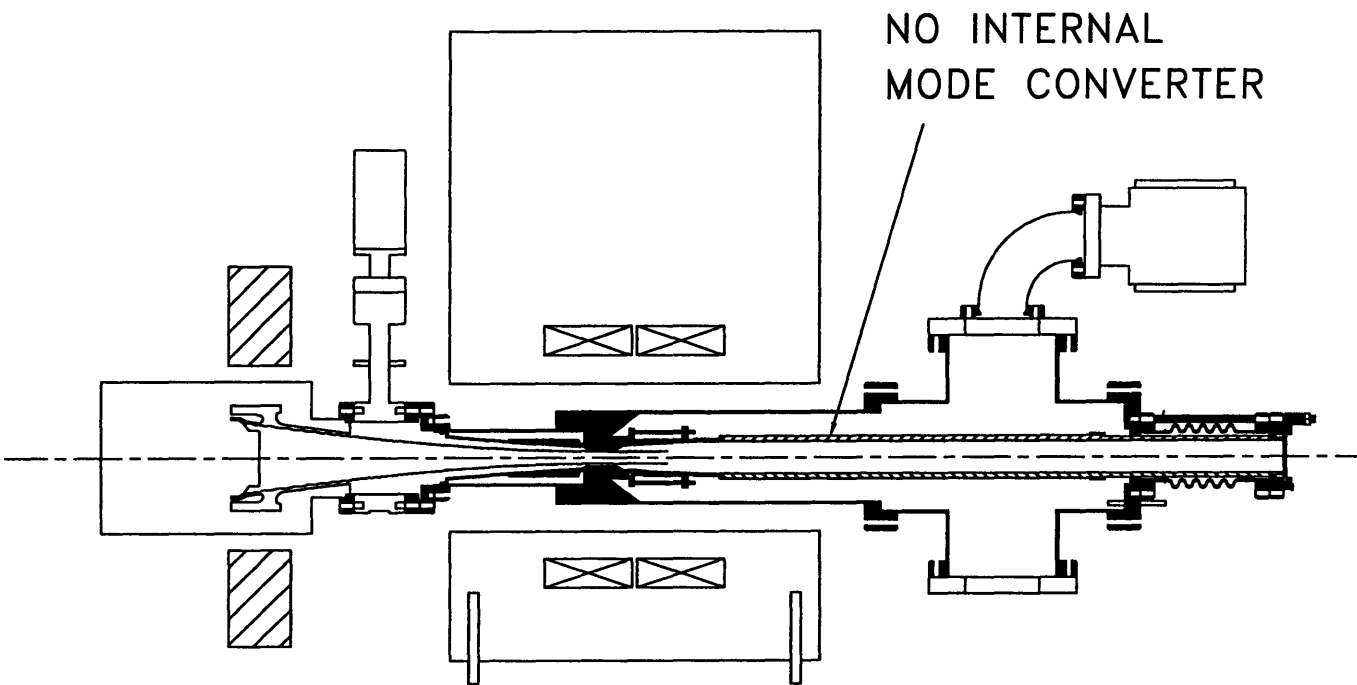## (FIRST OPERATION)

NO INTERNAL
MODE CONVERTER

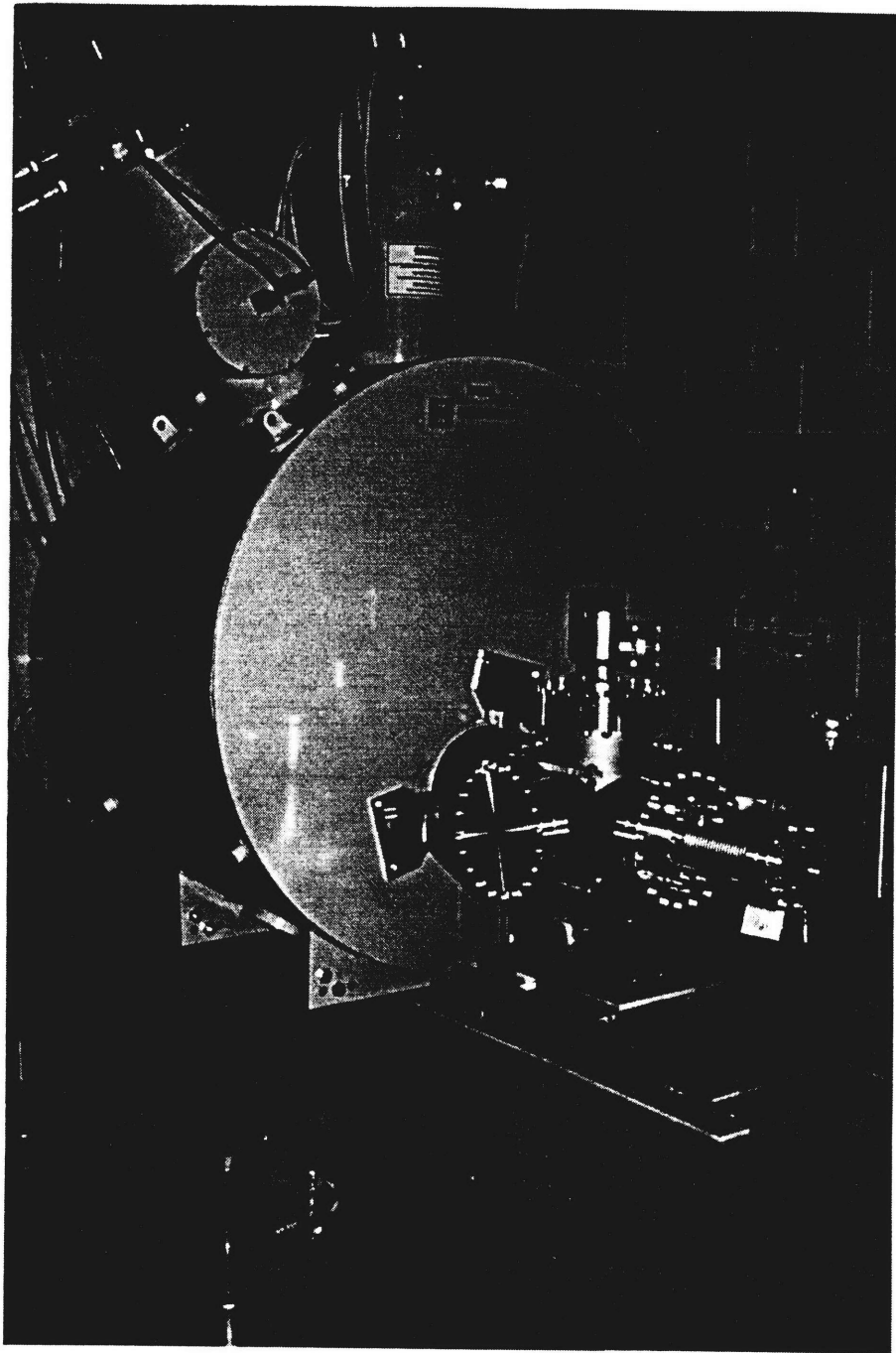Figure 4.1: Schematic of gyrotron setup for first operation.

Figure 4.2: Picture of the gyrotron experiment setup.

3 μsec pulses. The voltage of the pulse is measured with a capacitive voltage divider (CVD) on the secondary side of the pulse transformer. The voltage ratio $V_c : V_{CVD}$ is calibrated to be 11700:1 for this experiment. The current signal is measured with a Rogowski coil. Typical pulse repetition rate was 2 Hz but can be as high as 6 Hz. Typical experimental traces are shown in Fig. 4.3. Here the flat-top of cathode voltage signal is shown at 85 kV, while the beam current is 48 A. Note that the current signal is wider in width that the voltage signal. This is due to the fact that the electron gun is operating in the temperature limited regime so that the beam current is not a strong function of the applied voltage. The RF signal is detected by a diode positioned outside the vacuum window. The diode signal is transmitted to a digital scope via a coaxial cable. The capacitive probe signal is calibrated to give the parallel velocity of the electron beam. The large spikes at the beginning of the capacitive probe signal are due to noise.

Alignment of the gun axis and the magnetic field axis is important for achieving low beam velocity spread. For alignment, the axial component of the local magnetic field is measured azimuthally around the cylindrical housing of the electron gun. The accuracy of the alignment is a radial displacement of less than 0.2 cm.

The alignment of the cavity axis and the beam axis is critical for obtaining optimum coupling of the beam and the RF. The plot of efficiency versus beam radius in Fig. 3.7 shows the cavity axis must be aligned with the beam within a tolerance of 0.02 cm in order to maintain efficient coupling. The alignment is done by monitoring the beam interception on a beam scraper right before the cavity. The beam scraper is a ring with an inner radius of 1.2 cm. Although alignment with the beam scraper is reproducible within a radial displacement of ±0.01 cm, it is based on the assumption that beam density is uniform azimuthally. Fine tuning of the alignment must be done by maximizing the RF signal from the gyrotron.

4.1.1 Mode Identification

The frequency of the output is measured with a harmonic mixer and a digital scope with FFT capabilities. The mixer combines the gyrotron output signal of frequency ν_{RF} with a local oscillator signal of frequency ν_{LO}. The local oscillator is tuned to yield a 0.3 GHz intermediate frequency, with $\nu_{RF} = n\nu_{LO} \pm \nu_{IF}$, where n is the harmonic number. The accuracy of this frequency measurement system is ±10 MHz and can be used to identify the mode excited in

89

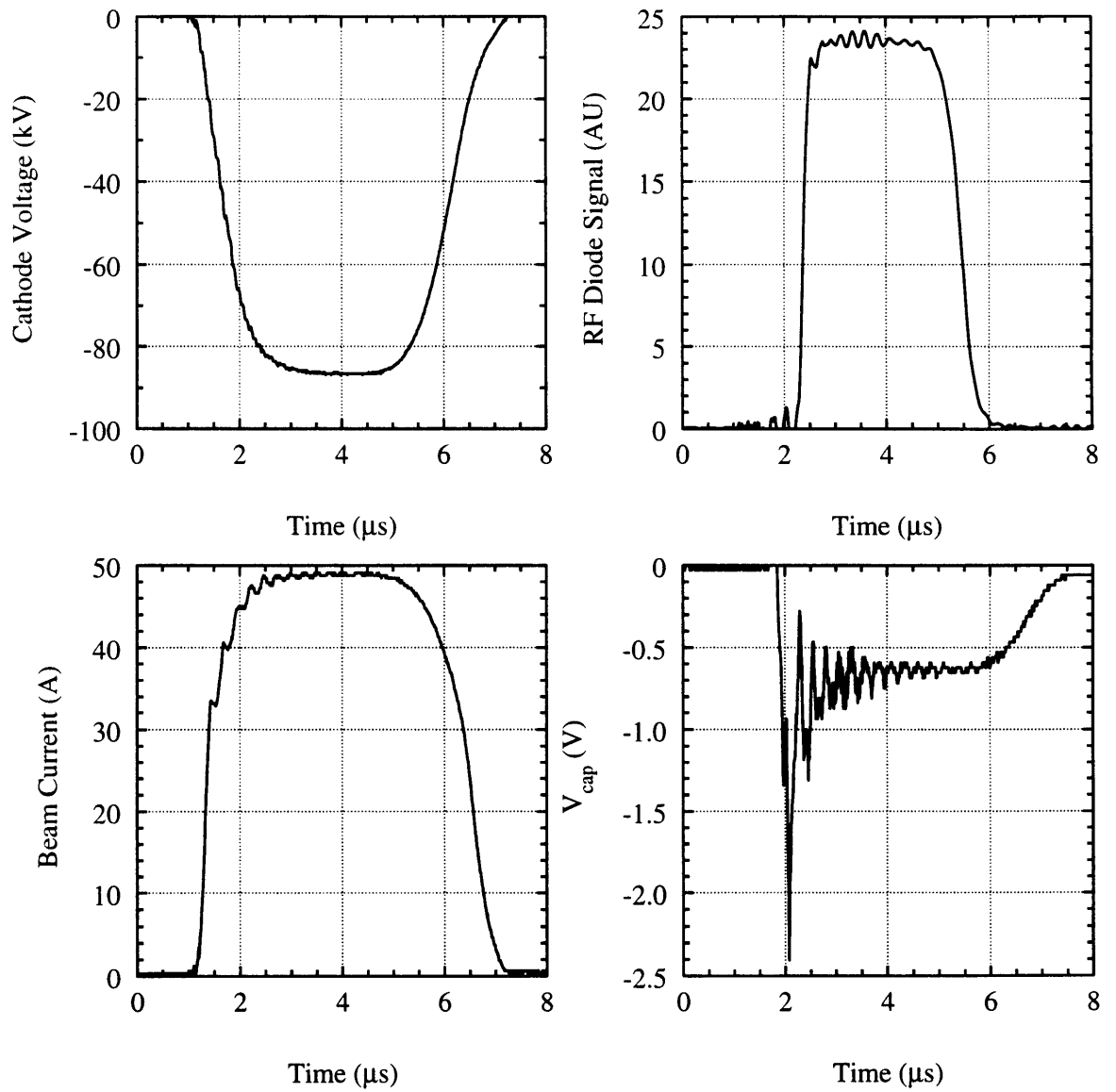Figure 4.3: Typical signal traces of cathode voltage, beam current, RF diode and capacitive probe.

m	p	ν_{exp} (GHz)	ν_{thry} (GHz)	$\Delta\nu$(MHz)
27	8	166.650	166.595	55
30	7	166.770	166.772	-2
22	10	168.400	168.350	50
25	9	169.507	169.445	62
28	8	170.110	170.066	54
31	7	170.190	170.167	23
23	10	172.008	171.965	43
26	9	173.124	172.981	143
29	8	173.518	173.526	-8
24	10	175.662	175.565	97
27	9	176.618	176.504	114
30	8	177.029	176.931	98

Table 4.1: Comparison of measured frequency and theoretical frequency predicted by cold cavity simulation.

the gyrotron.

Cathode voltage, mod-anode voltage, cathode and cavity magnetic fields, and beam current are the parameters that can be adjusted in the experiment. By changing these parameters, a large number of TE_{mp} modes were excited between 166 GHz and 177 GHz. The measured frequencies are compared to the theoretical frequencies of different modes calculated from cold cavity simulations. All measured frequencies are identified and are listed in Table. 4.1. Observed are TE_{mp} modes with m from 22 to 31 and p from 7 to 10. The discrepancies between the measured and the theoretical cold cavity frequencies are due to presence of the electron beam which modifies the RF frequency from the cold cavity value. The magnitude of the frequency shift depends on operating parameters. However it should not exceed the bandwidth of the gyrotron mode approximately given by $\Delta\omega/\omega \approx 1/Q$. For our specific gyrotron $\Delta\omega$ is of the order of 150 MHz. Therefore most of the modes can be identified if the discrepancy is within 150 MHz and frequencies of nearest neighboring modes are distinctly separated. However for several modes, such as the case for $TE_{28,8}$ and the $TE_{31,7}$ modes, the distinction of one mode from the other requires knowledge of the relative coupling constant C_{mp} of each mode at that particular beam radius. An average shift of 60 MHz can be seen between the theoretical and measured frequencies. This could be explained by a 6×10^{-6} m fabrication error in the cavity radius. The tolerance for fabrication was specified at 2.5×10^{-5} m.

4.1.2 Measurement of Power and Efficiency

The output power is measured with a calorimetric method. A 10 cm diameter Scientech calorimeter is placed in front of the output window. The absorption coefficient of the calorimeter surface is calibrated to be $82 \pm 3\%$ in the frequency range of $166 - 173$ GHz. The power was measured at a repetition rate of 2 Hz. The calorimeter measurement provides the average output power P_{avg}. The peak power is calculated from $P_{peak} = P_{avg}/(f_{rep}\tau)$, where f_{rep} is the repetition rate and τ is the pulse width. With the relative error in measurement of the pulse width, and the uncertainty in the reflection coefficient of the calorimeter, the relative error for the power measurement is $\pm 5\%$. This translates into $\pm 2\%$ relative error for measured efficiency around 30%.

During the investigation of the gyrotron performance near the design frequency of 170 GHz, it was found initially that the $TE_{27,8,1}$ mode at 166.6 GHz was easier to access than the design mode and thus attention was focused on this mode. First the optimized power and efficiency were measured as the beam current is increased. The result is shown in Fig. 4.4. The shot-to-shot power stability was better than 5% at each operating point. Single mode emission was confirmed using the frequency measuring system at all currents. Over 30% efficiencies were achieved for currents over 15 A. Also plotted is the optimized detuning parameter Δ, which is calculated from the cavity magnetic field, the beam energy, the rf frequency, and the transverse beam velocity. The increase in Δ as the beam current rises is consistent with nonlinear theory. This can also be understood from the starting current curves in Fig. 3.8. As beam current increases, the high efficiency (hard excitation) region of each mode is shifted to lower magnetic field region, thereby increasing the normalized detuning parameter.

Although more difficult than the $TE_{27,8,1}$ mode, eventually we were able to obtain high power and high efficiency for the designed $TE_{28,8,1}$ mode. The high power measurement results are summarized in Table 4.2. High power was measured in the $TE_{28,8,1}$ mode as well as the adjacent $TE_{27,8,1}$ and $TE_{29,8,1}$ modes. Highest power levels were achieved in both $TE_{27,8,1}$ and $TE_{28,8,1}$ with ~ 50 A beam current for efficiencies close to 35%. At the design point as shown in the third column, 1.07 MW power was observed in $TE_{28,8,1}$ mode with 35.0% efficiency. Taking into account 11% total power loss in the cavity, waveguide and output window, these efficiencies are in good agreement with the predictions of the multimode code MAGY assuming
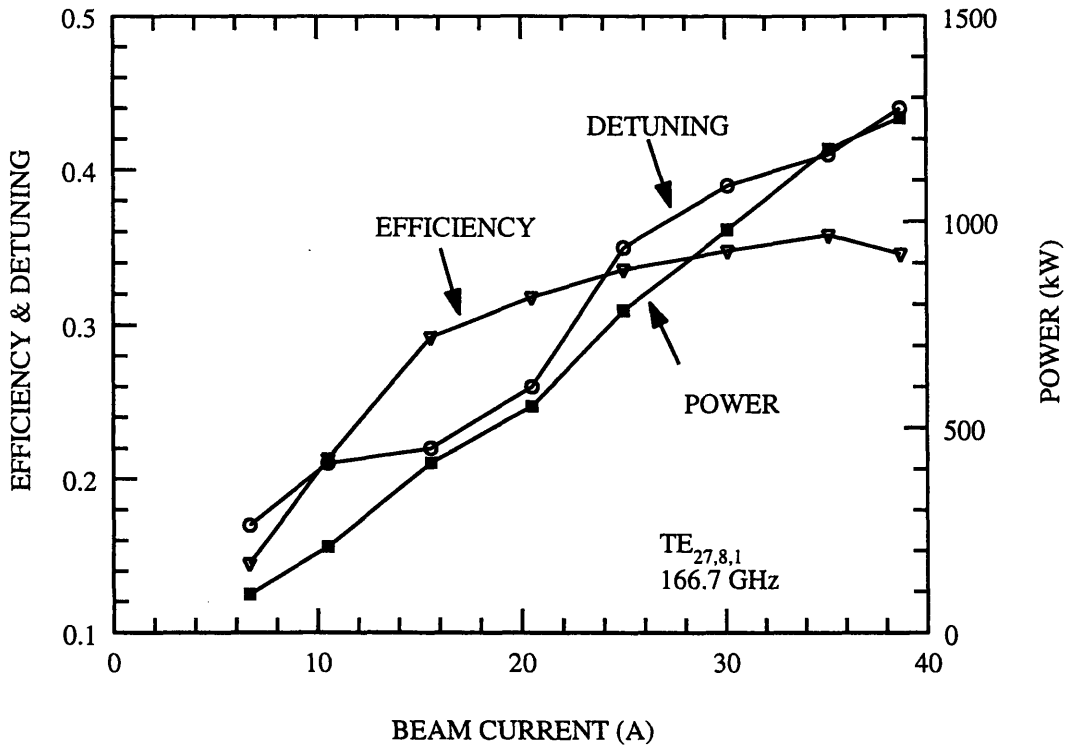
Figure 4.4: Optimized power and efficiency versus beam current in $TE_{27,8,1}$ mode.

8% perpendicular velocity spread. At all currents, with measured beam and field parameters which produced maximum efficiencies in the $TE_{28,8,1}$ mode, the self-consistent single-mode code predicts 39% RF efficiency with 8% perpendicular spread. However, the measured Δ of 0.47 is lower than 0.52, value for which SCSM code predicts the maximum efficiency.

Fig. 4.5 shows measured power and efficiency versus beam current for $TE_{28,8,1}$ and $TE_{27,8,1}$ modes. Both modes maintain efficiencies of 34% or above for beam current over 25 A and up

Mode	$TE_{27,8,1}$	$TE_{27,8,1}$	$TE_{28,8,1}$	$TE_{28,8,1}$	$TE_{29,8,1}$
V_c (kV)	83.0	84.1	84.0	86.5	86.9
I (A)	36.5	54.7	36.4	48.8	35.2
B_0	6.580	6.532	6.717	6.701	6.850
α	1.41	1.43	1.59	1.53	1.41
r_b (cm)	0.837	0.835	0.842	0.840	0.842
Δ	0.49	0.54	0.47	0.52	0.56
Power (MW)	1.09	1.56	1.07	1.50	1.10
Efficiency (%)	36.1	33.9	35.0	35.6	35.8

Table 4.2: Summary of high power and high efficiency measurement in $TE_{m,8}$- modes where $m = 7, 8, 9$.

to 50 A.
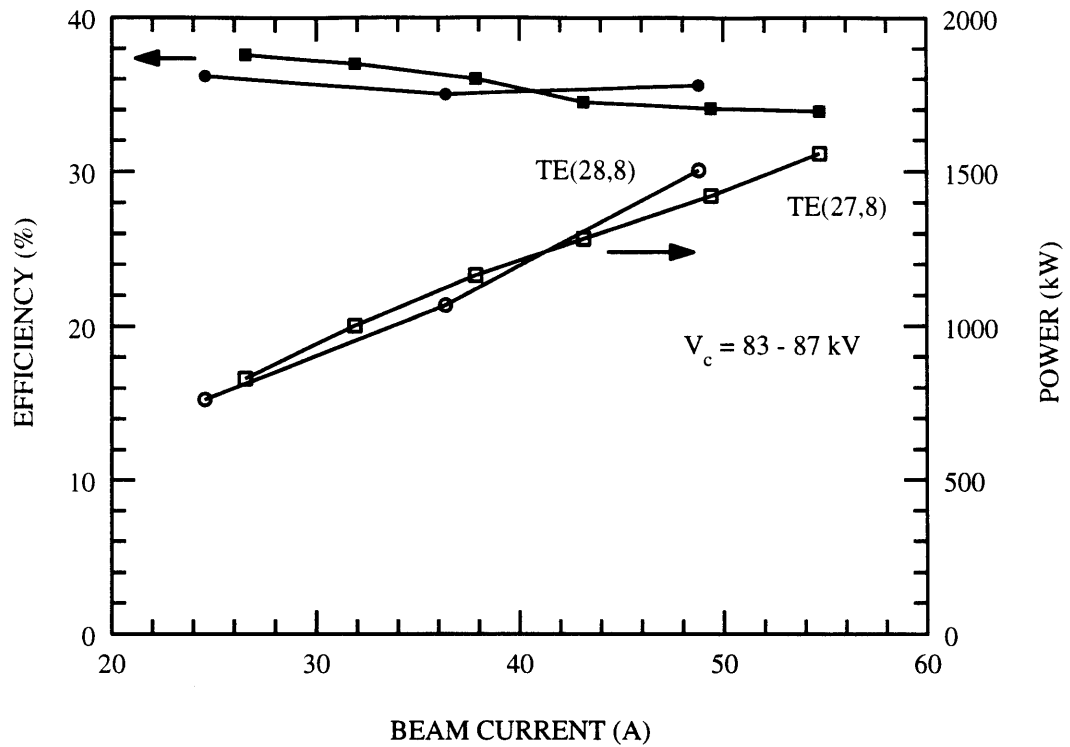
Figure 4.5: Comparison of operating characteristics of the $TE_{27,8,1}$ and $TE_{28,8,1}$ modes at high current.

Fig. 4.6 shows optimized efficiency in the $TE_{28,8,1}$ mode for different velocity ratio values but at approximately the same cathode voltage and beam current. Also plotted is the optimum efficiency predicted by the SCSM code with these α values. The increase in measured efficiency is consistent with theory at low α values. However the measured efficiency saturates at α of 1.6 and declines slightly as α further increases. There are two possible explanations for this discrepancy. One is the enhanced mode competition at high α values due to increased interaction length since the normalized interaction length μ scales as $\beta_\perp^2 / \beta_\parallel$. This indicates that although higher α means more energy is contained in the transverse motion of the beam for extraction and hence higher total efficiency could be expected, mode competition from the azimuthal mode prevents high efficiency region to be reached. Efficiency can also be reduced at high α values due to higher velocity spread since the beam with high α is more prone to electrostatic instabilities that induce velocity spread.

Optimized efficiency in the $TE_{28,8,1}$ mode as a function of cathode voltage is shown in
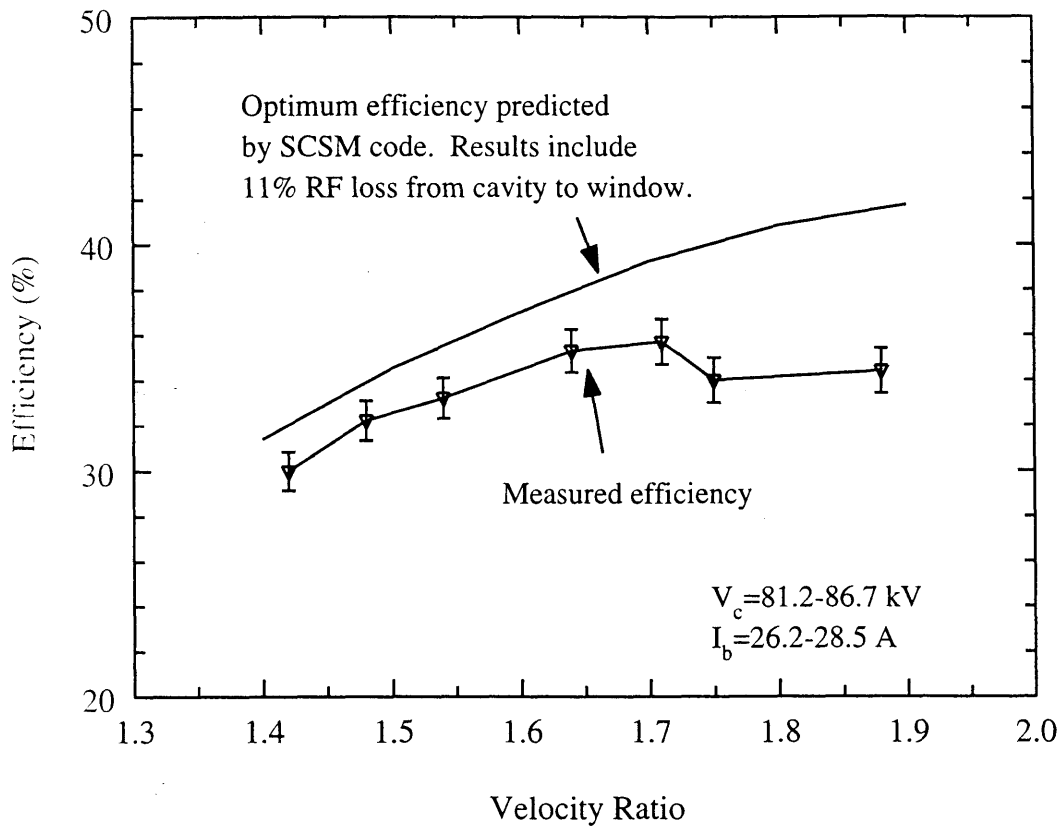
Figure 4.6: Optimized efficiency in the $TE_{28,8,1}$ mode is plotted as a function of velocity ratio. Here the cathode voltage is chosen between 80 to 85 kV, beam current between 28 to 33 A, and the efficiency is optimized by adjusting the magnetic field in the cavity.

Fig. 4.7. As can be seen, between 77 kV and 86 kV, the optimum efficiency is rather insensitive to the cathode voltage. Optimized efficiencies near 70 kV and 100 kV are both close to 30%.
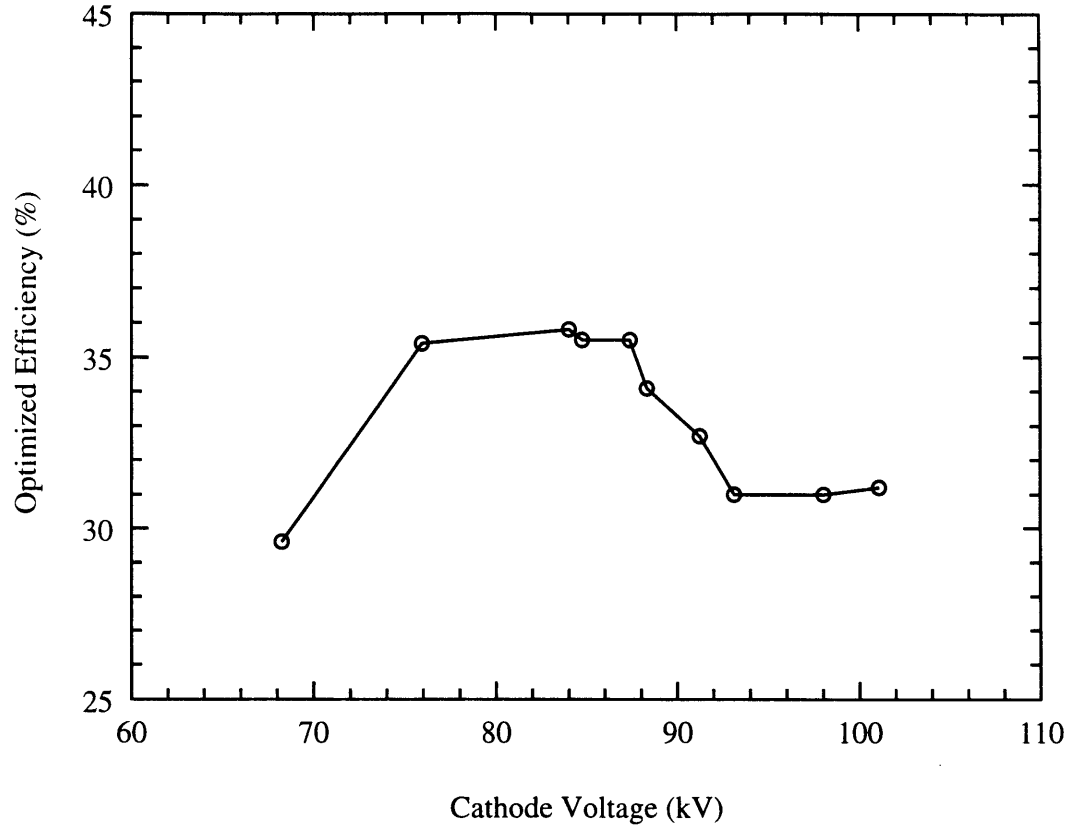
Figure 4.7: Efficiency at different cathode voltage values. The beam current varies from 28.2 A to 33.0 A, and the velocity ratio varies from 1.51 to 1.84. The cavity magnetic field is adjusted at each point to optimize the efficiency.

4.1.3 Startup Measurement

The influence of startup on the operating behavior is also investigated. It has been shown by Whaley et al.[48] that the way in which the operating point is reached can be used to eliminate excitation of undesirable modes and assure oscillation in the proper mode.

The rise time of the voltage pulse is much longer than the time of oscillation growth ($\sim Q/\omega = 1.3$ ns), and the transit time of electrons through the cavity ($L/v_\parallel = 0.1$ ns). This allows one to consider each point on the voltage rise curve as an equilibrium state and the voltage increase as a quasi-stationary process.

Fig. 4.8 shows the startup characteristics when the $TE_{28,8}$ mode is excited as the cathode

voltage was raised to 105 kV. The non-adiabatic behavior of the gun is evident with the oscillatory dependence of α on cathode voltage. Also shown are the theoretical curves for the linear starting current for the main competing modes. Inside the locus, the theoretical linear starting current is lower than the beam current and therefore the mode can be excited. It should be noted that the measured velocity ratio is used in the present study of the startup scenario, whereas in the investigation of startup by Whaley, an adiabatic dependence of α on V_c is assumed.
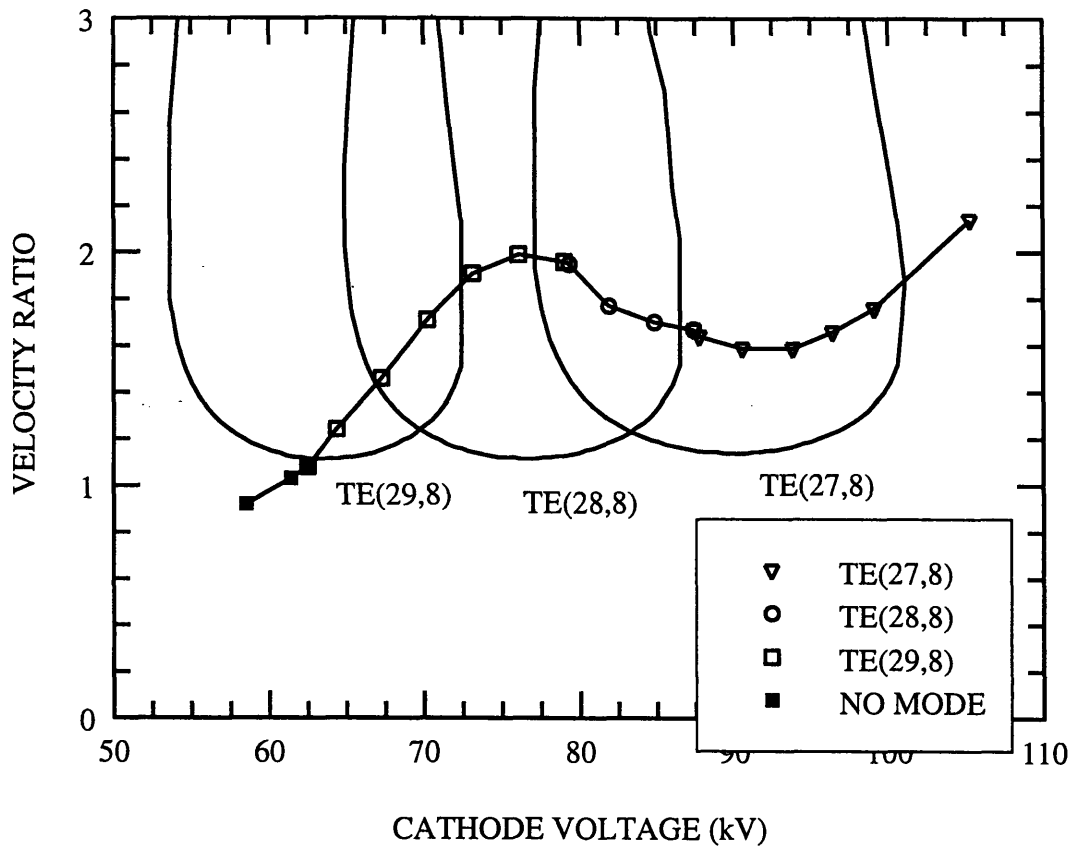
Figure 4.8: Modes observed during startup with predictions based on linear theory. The scan was done for a magnetic field of 6.77 T. The beam current varied from 21.2 A at 60 kV to 26.9 A at 104 kV.

No microwaves were observed when the cathode voltage is below 63 kV. At that point, $TE_{29,8}$ is excited, consistent with the theoretical starting prediction. The region of operation for each excited mode is consistent with the linear theory. However each mode continue to oscillate beyond the region predicted by linear theory, an indication that the mode is operating in the hard excitation region.

4.1.4 Mode Map Construction

A map of the observed modes is produced by varying the cathode and cavity magnetic field, and is shown in Fig. 4.9. Varying the cathode field changes the beam radius r_b and also the beam velocity ratio α. Varying the cavity field allows one to change the cyclotron frequency of the electron beam, hence optimizing the detuning parameter Δ for the excited mode. The upper boundary of the region where the modes are excited corresponds to a magnetic compression of about 32. Above this boundary the compression is too small, so that the beam is intercepted by parts of the beam tunnel before reaching the cavity. The lower boundary, which corresponds to a compression of 40, indicates the region where electrons start to reflect back into the gun because α is too high. Between these two boundaries there are primarily two rows of azimuthal TE_{mp} modes with radial indices p of 8 and 9.

Figure 4.9: A map of the observed modes as a function of the cathode and cavity magnetic fields. The cathode voltage and the beam current are kept at 82.3 kV and 25.0 A, respectively.

In general, the gyrotron was characterized by regions of single mode emission, although there are a few operating regions that resulted in multimoding, such as the boundary between
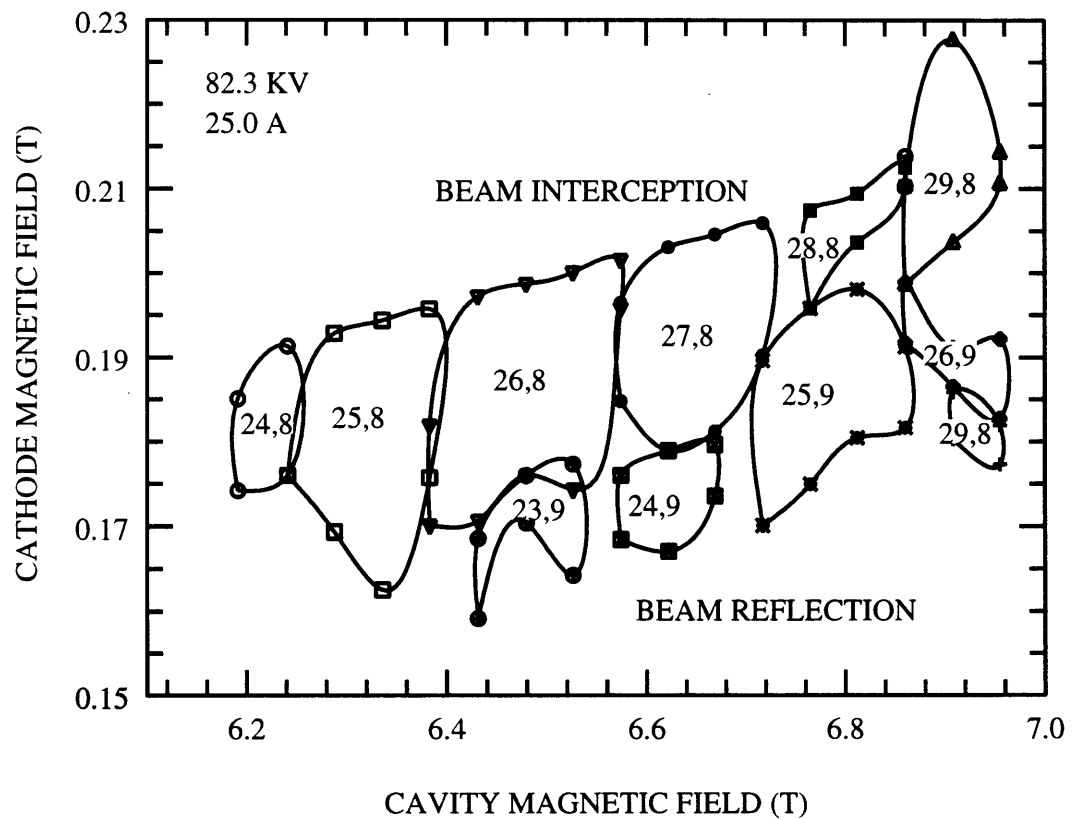
98

the $TE_{24,8}$ and $TE_{25,8}$ modes. It is also evident that the region of excitation for $TE_{28,8}$ is smaller than regions of neighboring modes. This may be due to the fact that the window was matched to the $TE_{28,8}$ frequency of 170 GHz. For other modes at different frequencies, the power reflection at the window influences both the the quality factor and the field distribution in the cavity. The starting current of the competing modes is decreased due to higher quality factor, thus they are excited more easily in the resonator.

As can be seen from Fig. 4.9, mode switching from the $TE_{28,8}$ mode to the $TE_{25,9}$ mode occurs at the field compression ratio of 34, corresponding to beam radius of 0.840 cm in the cavity. This result is consistent with the prediction of the multi-mode simulation.

4.1.5   Effect of Power Reflection at the Output Window

The consequence of RF reflection at the output window is its effect on oscillations in the cavity. The reflected RF waves will travel back through the waveguide system to the cavity and influence the field structure and quality factor. Detailed study of this effect can be done by means of Rieke diagrams [49]. A theoretical discussion of further aspects of reflections on gyrotron performance is given in [50].

One indication of the effect of the power reflection is shown in the measurement of RF frequency as a function of the detuning parameter for different modes. The detuning parameter $\Delta = 2/\beta_\perp^2(1 - \omega_c/(\gamma\omega))$ can be adjusted in the experiment either by varying the cathode voltage, thus changing the relativistic factor γ, or by tuning the cavity magnetic field. Fig. 4.10 shows measured frequencies for $TE_{27,8}$ and $TE_{28,8}$ modes versus detuning Δ as a result of varying the cavity magnetic field. Cathode voltage and beam current are fixed at 83 kV and 38 A. A discreet frequency jump of 75 MHz was observed for the $TE_{27,8}$ mode. The frequency jump roughly matches the frequency difference between two waves such that the phase factors at the window $k_z L_w$ differ by $\pi/2$. Here L_w is the distance from the end of the cavity to the window, and is 78 cm in this experiment. On the other hand, the frequency of the $TE_{28,8}$ mode is continuous, and the slope of the curve is in agreement with the SCSM code predictions. The shift of 60 MHz in frequency can be explained by the cavity machining error.
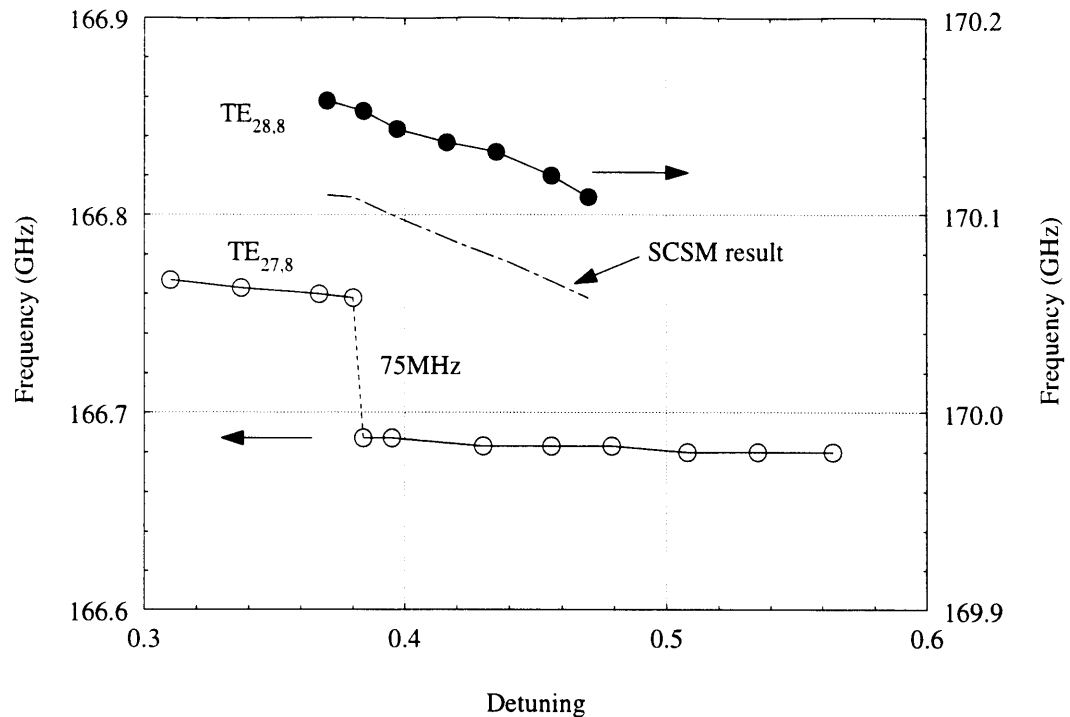
Figure 4.10: Change of output frequency as a function of detuning Δ. The detuning was changed by varying the cavity magnetic field while the cathode voltage is kept at 83 kV and the beam current at 26 A. The dotted line represents a discrete jump in frequency.

4.2 Electron Beam Properties

4.2.1 Velocity Ratio Measurement

The high power and high efficiency results indicate that the electron gun is producing a good quality beam with the expected characteristics. A more direct confirmation that the gun is operating as designed can be obtained by measuring the velocity ratio of the electron beam as operating parameters are being changed. Measurements were taken with the capacitive probe as describe in Sec. 2.2.5. The measured results are compared with EGUN simulations.

Fig. 4.11 shows the velocity ratio as a function of the cathode voltage. Plotted are measured data as discrete points and EGUN results as continuous lines. Constant ratio of mod-anode to cathode voltage is maintained. Two sets of curves are shown for V_a / V_c of 0.258 and 0.236. At higher mod-anode to cathode voltage ratio, higher α values are obtained. Although the peaks of both experimental curves are shifted slightly toward lower voltage compared to the theoretical predictions, both experimental and theoretical curves show similar oscillatory dependence with

nearly the same peak values.

As can be be seen from Fig. 4.11, the sensitivity of α to variation in cathode voltage is low at 83 kV. The advantage of this feature in future CW operation needs to be investigated. The drawback seems to be the inflexibility in controlling the velocity ratio at the designed point. However as indicated by the power measurement, α much higher than 1.5 does not lead to higher efficiency. Also as will be shown later, the maximum α that can be achieved before the beam starts to get reflected is 1.8 for a 83 kV, 38 A beam. With added spread, the maximum achievable α would be even lower. Thus there is no clear advantage in designing an adiabatic gun for the purpose of achieving higher α.

For the curve with higher α values, beam reflection was observed at the highest α of 2.3. Thus this startup scenario should be avoided because the reflected electrons could damage the cathode emitter. However this is not a concern in the CW operation since separate power supply can be used to supply voltage to the mod-anode and therefore any desired startup scenario can be achieved.

In Fig. 4.12 the dependence of velocity ratio on the mod-anode voltage is plotted. Again good agreement can be seen between EGUN and the experimental results. The non-adiabatic nature of the beam characteristics is evident from the comparison with adiabatic prediction.

Fig. 4.13 shows α versus the cathode magnetic field. Comparison with the EGUN result shows discrepancy particularly for cathode field less than 1.84 kG. These measurements were taken at beam current of 20 A, and reflection of beam current was observed for α greater than 2.3. Possible explanation for this is the space charge effect of the reflected current as well as contribution to capacitive probe signal from electrons trapped between the gun and the cavity.

4.2.2 Experimental Estimate of Velocity Spread

In Sec. 3.4.2, we estimated the total perpendicular velocity spread of the designed electron gun to be less than 8%. Large velocity spread not only reduces the efficiency of the gyrotron interaction, it also limits the maximum achievable velocity ratio when part of the electron beam starts to be reflected. Experimental determination of the spread is rather difficult. In the past, there have been measurements using retarding potential method. As voltage is applied to the collector, a fraction of the beam with high transverse velocity component will be repelled.

EGUN simulation
□ measured α for V_a/V_c=0.258
○ measured α for V_a/V_c=0.236

Velocity Ratio

3.0
2.5
2.0
1.5
1.0
0.5
0

40   60   80   100
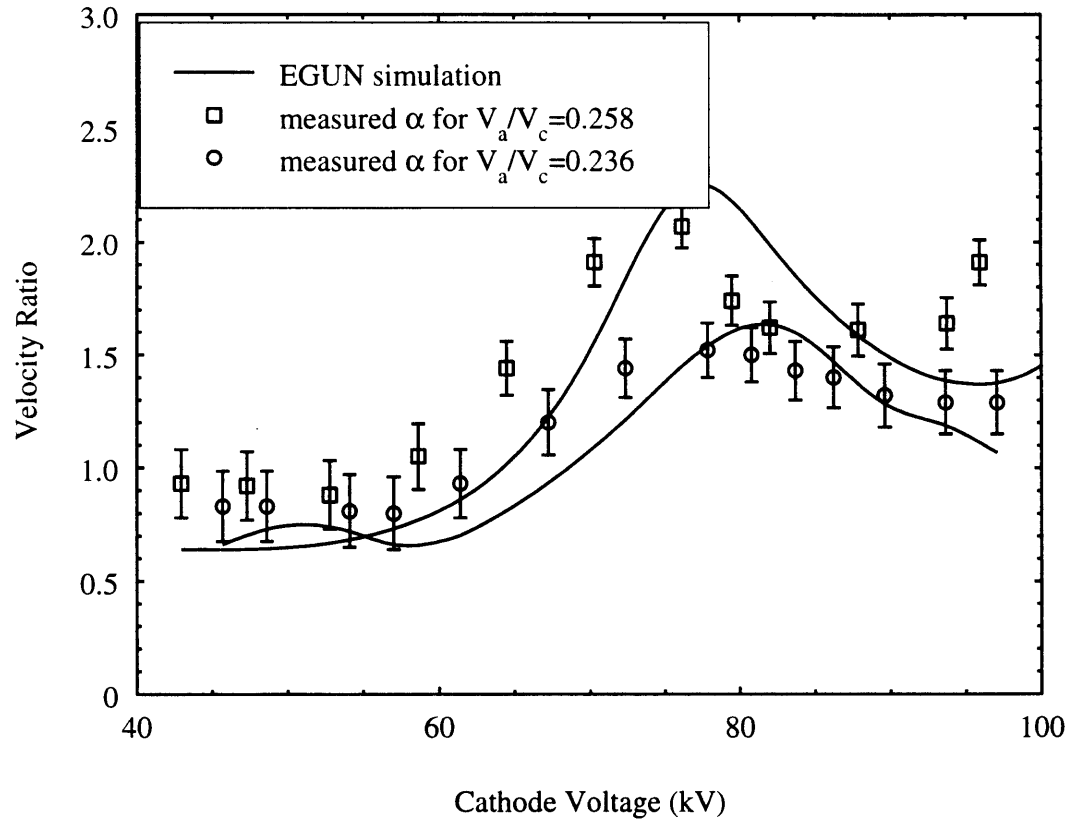
Cathode Voltage (kV)

Figure 4.11: A comparison of the beam velocity ratio as measured with a capacitive probe with predictions based on EGUN. Here the velocity ratio is plotted as a function of cathode voltage. The mod-anode voltage is kept at a constant ratio from the cathode voltage, $V_a = 0.236\,V_c$ (circles) and $V_a = 0.258\,V_c$ (squares).
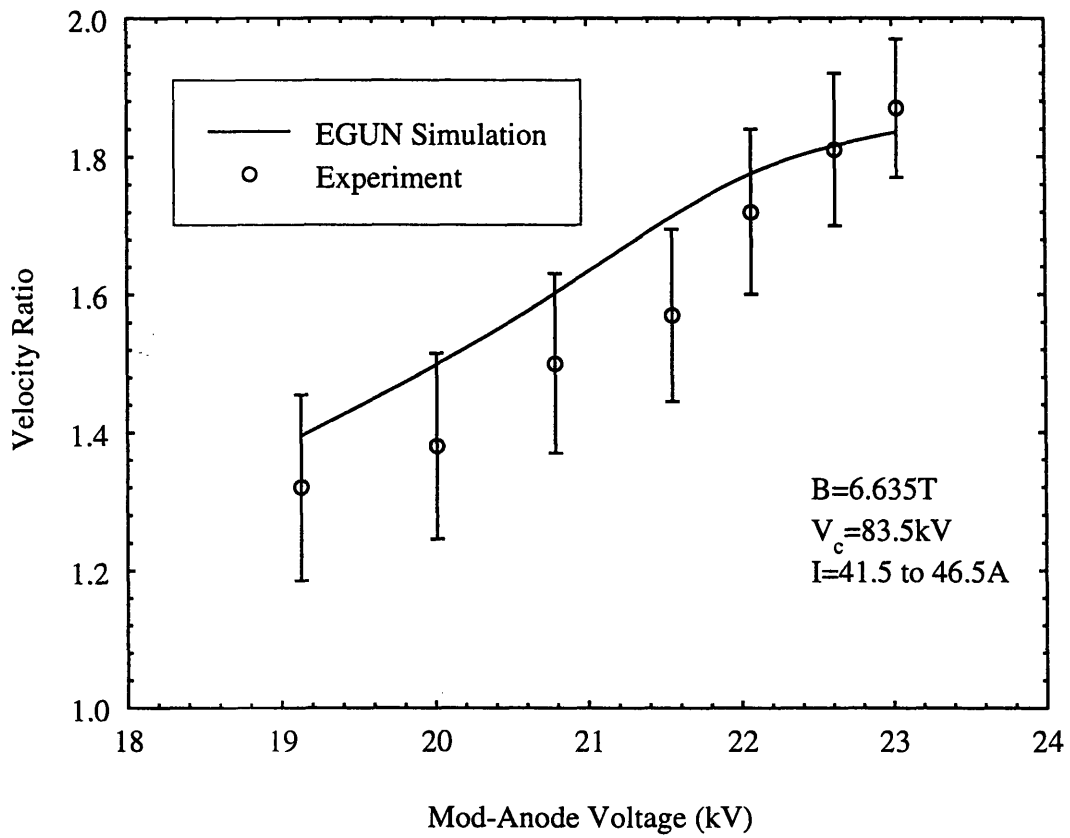
Figure 4.12: Measured beam velocity ratio as a function of mod-anode voltage.
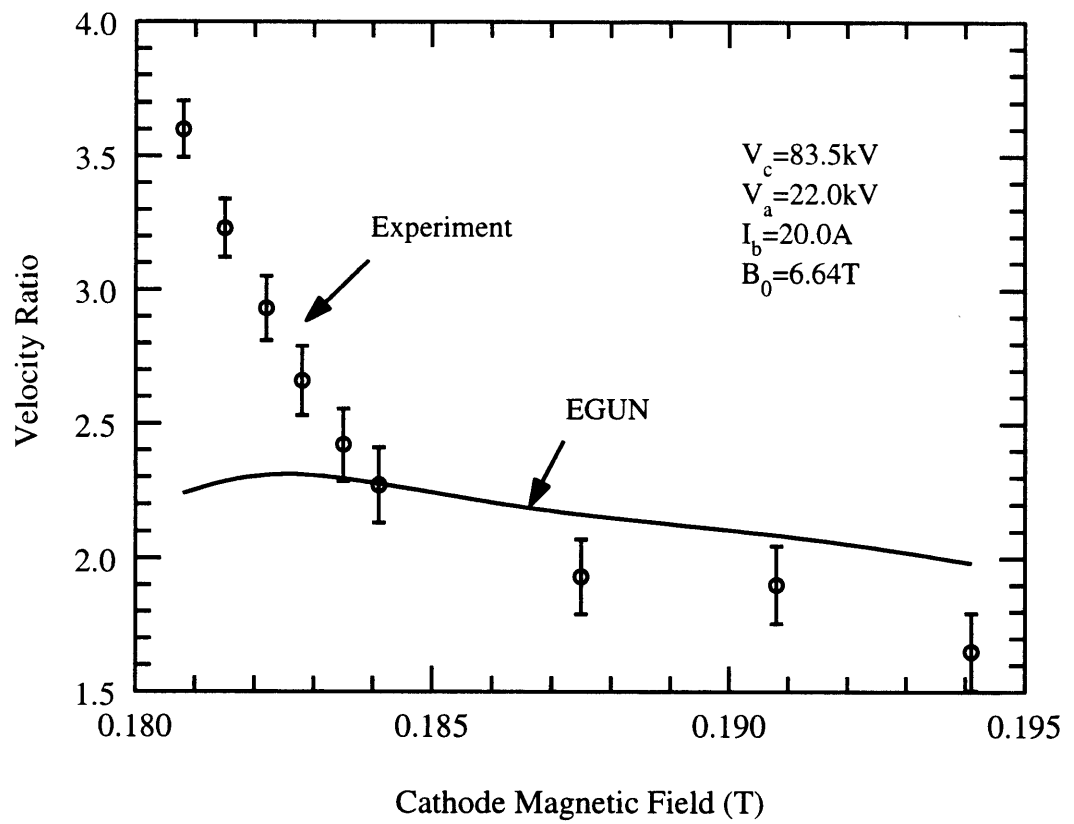
Figure 4.13: Measured beam velocity ratio as a function of cathode magnetic field.

The figure shows a plot with "Velocity Ratio" on the y-axis (ranging from 1.5 to 4.0) and "Cathode Magnetic Field (T)" on the x-axis (ranging from 0.180 to 0.195). Data points labeled "Experiment" with error bars and a curve labeled "EGUN" are shown. Parameters listed: $V_c = 83.5\text{kV}$, $V_a = 22.0\text{kV}$, $I_b = 20.0\text{A}$, $B_0 = 6.64\text{T}$.

The velocity spectrum can be obtained by measuring the intercepted current versus the applied voltage. In the past, Russian researchers reported RMS spread of $\sim 10\%$ in transverse velocity measured using this method. Measurements at MIT [51] using more sophisticated version of the repelling collector yielded result of 6% RMS spread at low beam current.

The retarding potential measurement was not performed for this experiment. Instead, an estimate of the velocity spread was made from the reflected current measurement. For an electron beam with finite perpendicular velocity spread, as the velocity ratio increases, electrons with large perpendicular velocity component will be reflected to the cathode region. These electrons can either be intercepted by the mod-anode, by the cathode, become trapped electrons between the cathode and the cavity, or after a round trip to the gun region, return to the cavity region and exit the gyrotron. Experimentally, only the mod-anode current is monitored, therefore it is a lower limit to the reflected electron current.

The transverse velocity spread is a constant of motion along the beam path after the phase mixing region. This is confirmed by EGUN simulation as shown in Fig. 3.12. Assuming the largest perpendicular velocity of an electron is $v_{\perp 0} + \Delta v_{\perp max}$, and that the relative spread $\Delta v_{\perp} / v_{\perp}$ does not change with velocity ratio, then the maximum velocity ratio without electrons being reflected is given by

$$\frac{\Delta v_{\perp max}}{v_{\perp 0}} = \frac{1}{2\alpha_{max}^2}. \tag{4.1}$$

If the velocity distribution is assumed to be a square function given by

$$f(v_{\perp}) = \begin{cases} 1, & |v_{\perp} - v_{\perp 0}| < \Delta v_{\perp max} \\ 0, & |v_{\perp} - v_{\perp 0}| > \Delta v_{\perp max} \end{cases} \tag{4.2}$$

then the RMS spread can be expressed as

$$\left(\frac{\Delta v_{\perp}}{v_{\perp 0}} \right)_{rms} = \frac{\Delta v_{\perp max}}{\sqrt{3} v_{\perp 0}} = \frac{1}{2\sqrt{3}\alpha_{max}^2}. \tag{4.3}$$

For example, if maximum velocity ratio of 2 can be achieved before the beam starts reflecting, the RMS spread should not be larger than 7.2%. The assumption of a square distribution function yields higher values of spread than other symmetric functions, such as a parabolic

function. Thus the result is a conservative estimate for the upper limit of velocity spread.

In the experiment, the gun coil is used to adjust the cathode magnetic field. As the cathode field is decreased, the transverse velocity of the electron increases due to a larger compression ratio. Fig. 4.14 shows the rise of the mod-anode current in fraction of the beam current as the velocity ratio is increased. For beam current of 11 A, α reaches 2.8 before beam reflection occurs. From Eq. 4.3, the RMS spread is 3.7%. Similarly for beam current of 21 A, $\alpha_{max} = 2.3$, therefore the spread is 5.5%.

Values of α_{max} were also determined at higher beam currents. At beam currents of 38 A and 48 A, they are 1.8 and 1.6, corresponding to RMS spreads of 8.9% and 11.3%, respectively. At these high current levels, measurements of intercepted current versus velocity ratio were not performed since excessive beam interception may damage the cathode emitter.

It is also convenient to assume a Gaussian distribution function

$$f(v_\parallel) = \exp\left[\frac{(v_\parallel - v_{\parallel 0})^2}{2\Delta v_\parallel^2}\right], \tag{4.4}$$

where $-v_0 < v_\parallel < v_0$, $v_0 = c\sqrt{1 - 1/\gamma^2}$ is the maximum velocity of the electron, and $v_{\parallel 0}$ is the average parallel velocity. Then the ratio of the reflected current to the beam current can be expressed as

$$\frac{I_{ref}}{I_b} = \frac{\int_0^{-v_0} v_\parallel f(v_\parallel)\, dv_\parallel}{\int_0^{v_0} v_\parallel f(v_\parallel)\, dv_\parallel}. \tag{4.5}$$

The spread obtained in this manner seems to depend on the α value at which the estimate is being made. The average spread and the error bar is taken from estimates for α values that give $I_{mod-anode}/I_b$ between 0.1%-1%.

The estimated spread as a function of the beam current is plotted in Fig. 4.15. The result of both estimates qualitatively agree. The analysis of the results given in [51] also shows the spreads estimated using the above two methods are very close to the spread measured from the retarding potential method.
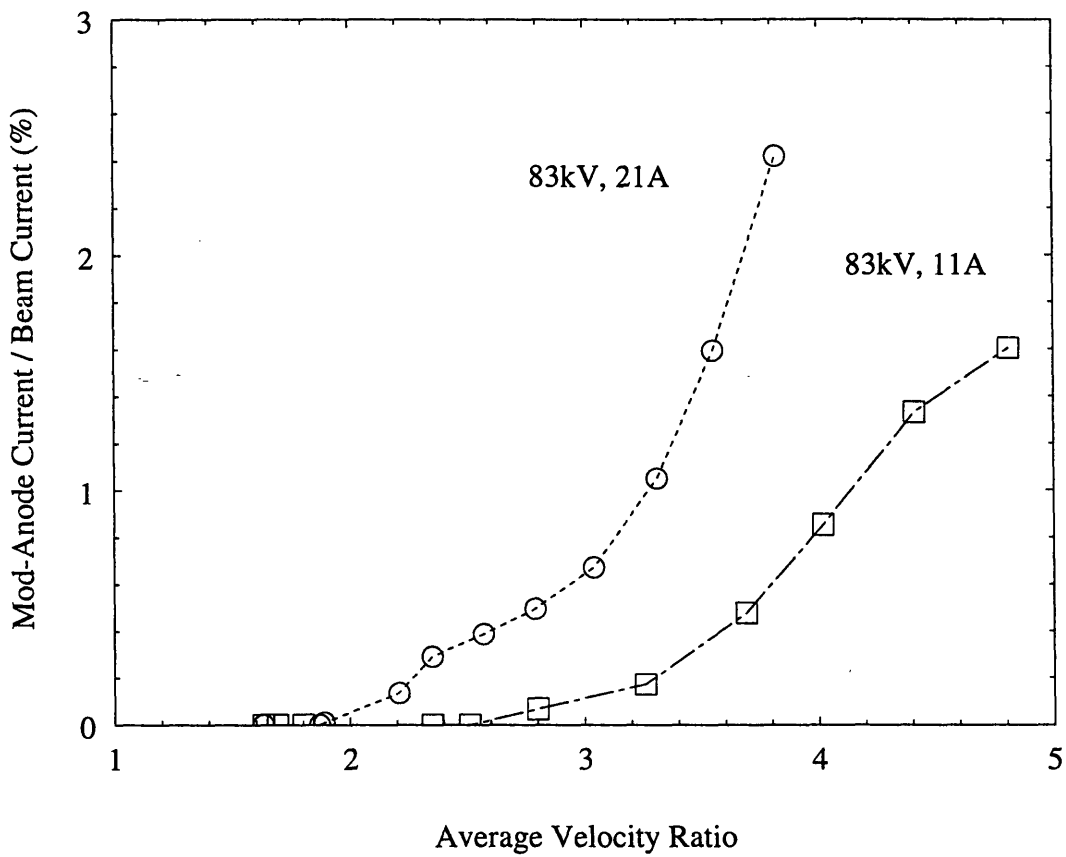
Figure 4.14: Reflected current being intercepted by mod-anode as a function of the average beam α.
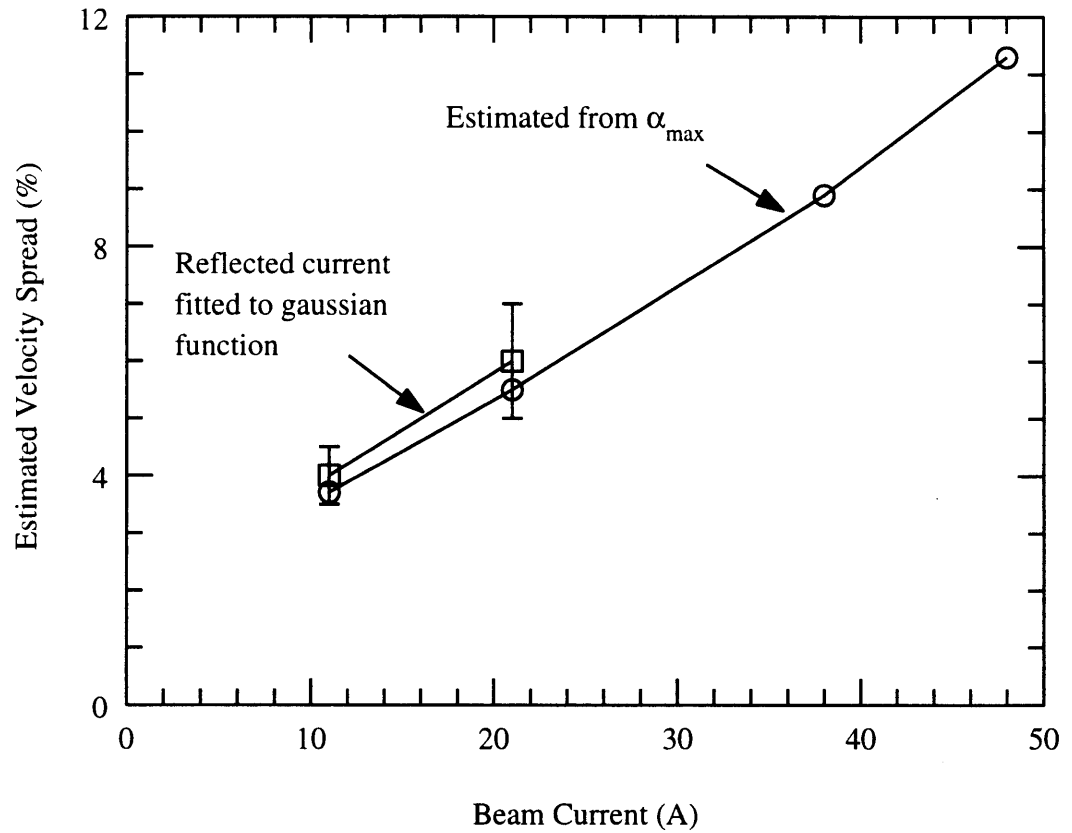
Figure 4.15: Perpendicular velocity spread as estimated from the maximum velocity ratio without beam reflection. A flat-top distribution function in $v_\perp$ space is assumed.

4.2.3 Cathode Emission

To understand the emission process of the cathode emitter, the beam current is measured as a function of the mod-anode voltage. The curves in Fig. 4.16 are for different settings of the cathode heater power. The temperature of the cathode is calculated from a table of temperature versus heater power as supplied by CPI, where the temperature of the emitter was measured with a pyrometer.

At low voltage, the gun is operating in the space charge limited regime and there is good agreement between the measurement and the theory curve given by

$$I = K V_a^{3/2} \qquad (4.6)$$

where the perveance K is calculated using Eq. 2.98. As voltage increases, there is a transition from the space charge limited regime to the temperature limited regime where emission strongly depends on the temperature of the cathode but weakly on the applied voltage. The slope of the curve in the temperature limited regime is due to the Schottky effect [52]. One notices the transition at low current is sharper, an indication of lower velocity spread.

4.3 External Testing of Mode Converter

4.3.1 Measurement of Radiation from Dimpled Wall Launcher

The measurement of the launcher wall perturbation was taken at the MIT Lincoln Lab to an accuracy of 5×10^{-6}m. The measured pattern is plotted in Fig. 4.17 and the designed pattern is shown in Fig. 4.18. Even after the best fit of the measured pattern with all possible tilt and offset errors, there is still distinct difference between the two patterns. Despite the discrepancy, it would still be interesting to test the launcher.

The performance of the dimpled wall launcher is assessed using the RF output from the gyrotron. The output port consists of a waveguide of 2.223 cm radius inside the vacuum extending to within 0.2 cm of the output window. Outside the window, a down-taper transmits power further into the launcher with minimal mode conversion. The profile of the down-taper is exactly the same as that of the up-taper used inside the tube.
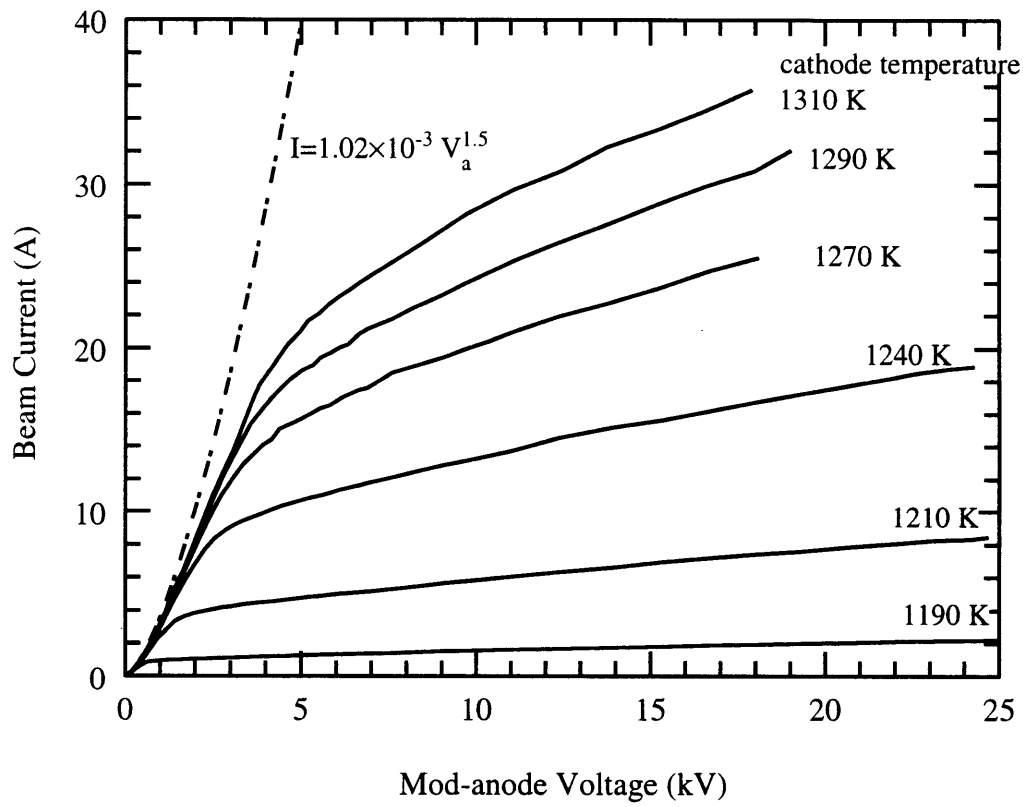
Figure 4.16: Cathode emission density versus mod-anode voltage.

The figure shows Beam Current (A) versus Mod-anode Voltage (kV). The dash-dot line is labeled:

$$I = 1.02 \times 10^{-3}\, V_a^{1.5}$$

The curves are labeled with cathode temperature: 1310 K, 1290 K, 1270 K, 1240 K, 1210 K, 1190 K.
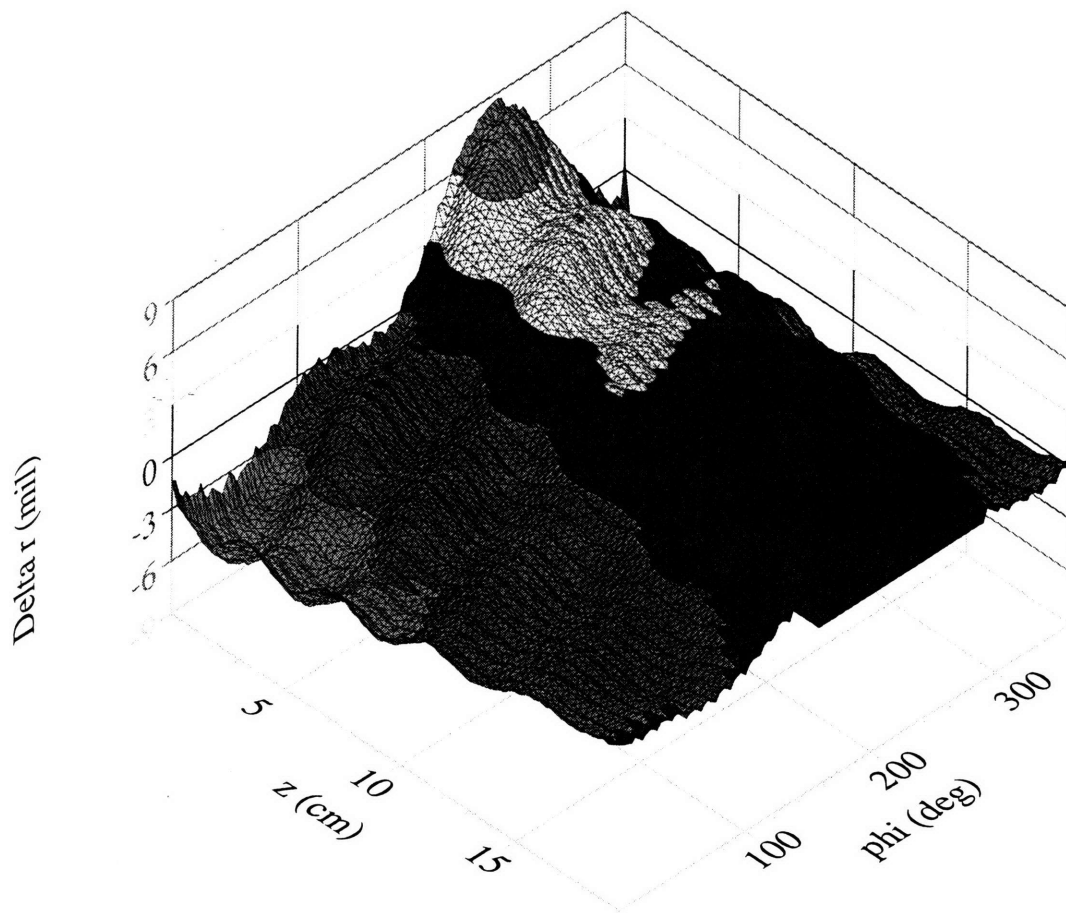
Figure 4.17: Measured dimpled wall pattern of launcher. (1 mil is 2.5×10^{-5} m)
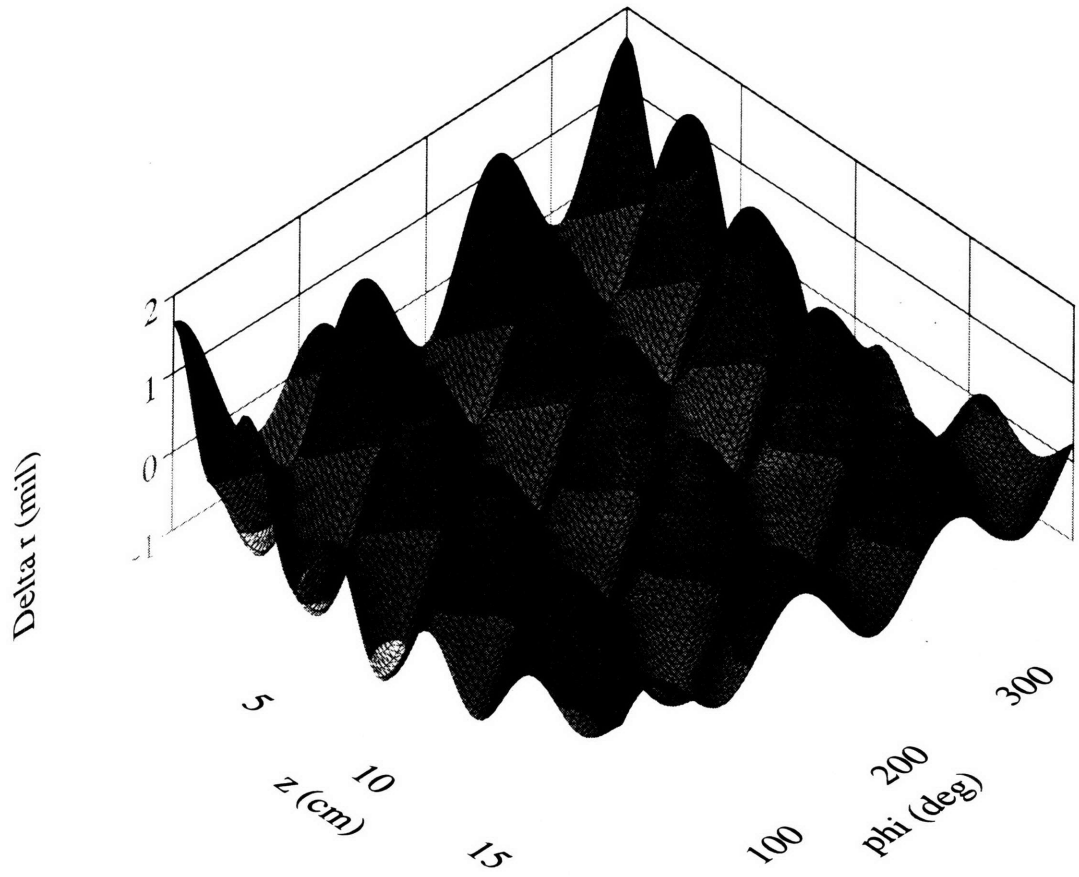
Figure 4.18: Dimpled wall pattern of launcher as designed.

For external testing, the mode purity of the signal going into the mode converter must be carefully verified beforehand since the mode converter was designed for a specific mode. With added modes, the experimental results would be difficult to interpret.

Generally there are two types of modes in the gyrotron output. The first type are the beam-excited modes such as the design mode or the competing modes, which are excited in the cavity by the interaction between electron beam and RF field. Because beam-excited modes are operated close to cut-off, they can be easily identified from the measured frequency.

The second type of modes are spurious modes excited in the waveguide system of the tube by unwanted conversion from a certain beam-excited mode. The conversion can occur at any axial inhomogeneity of the waveguide boundary, which are usually diameter transitions (tapers or steps), tilts and offsets between junctions [53], dielectric discontinuities (output window) [46]. This type of modes has the same frequency as the original mode, thus can not be distinguished by frequency. If the output port is a simple aperture, a scan of the far-field radiation pattern is usually made and compared to scalar diffraction theory which assumes the waveguide mode's RF field at the aperture is unperturbed and is radiated into free space.

The far-field measurement was made with a fundamental rectangular waveguide horn which detects E_θ in the far field. During the first scan of the radiation pattern from the window, difference of 5 decibel in peak signal levels was observed in the pattern on two side of the axis of symmetry. This indicates that mode conversion has occurred inside the tube. The gyrotron tube was brought open to air for visual examination. A radial offset of 0.02 cm at the junction between the second uptaper and the straight waveguide was indeed observed.

A careful alignment of the components was done before the gyrotron was reassembled. A scan of the far-field radiation was taken and is shown in Figure 4.19. Good agreement is shown between the measurement and the theoretical prediction. The symmetry of the antenna pattern indicates much improved mode purity. A 2-dimensional scan was not performed due to limitation of the equipment at the time. Instead, only the symmetry of the pattern in other directions is confirmed by measuring radiation power at various spatial locations. Good symmetry was observed in all cases.

The sleeve and the launcher were also carefully aligned to eliminate mode conversion. The radiation pattern from the end of the sleeve was similarly measured to verify the mode purity
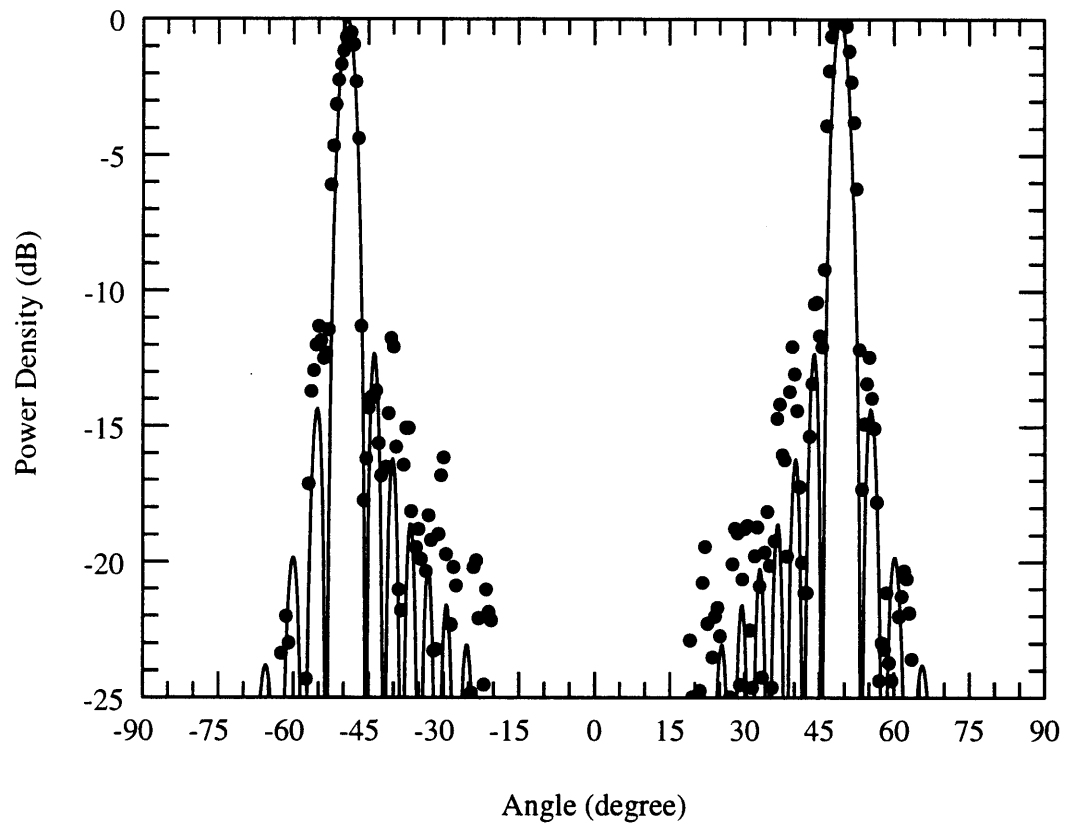
Figure 4.19: Far-field pattern of radiation from the output window.

before the dimpled wall launcher was attached to the down taper and the radiation from the rectangular cut was scanned using an X-Y scanner with a motorized attenuator. The results are shown in Fig. 4.20 and Fig. 4.22 for scans at $y = 6$ cm and 10 cm, where y is the distance between the detector plane and the launcher axis. Here the field intensity $|E_x|^2$ is plotted in decibel down from the peak value on the measured plane. The theoretical patterns for the designed converter using the Stratton-Chu diffraction theory are shown in Fig. 4.21 and Fig. 4.23. Comparison shows that the actual locations of the beam in the axial direction are in good agreement with the theoretical predictions. In the azimuthal direction, the measured beam propagation angle deviates from the theoretical value by 12°. Two peaks can be identified in the measured patterns in the azimuthal direction. Because the actual inner surface of the launcher is vastly different from the designed one, the Gaussian bunch could be slightly shifted from the location of the aperture. This could have resulted in wave diffracting off the edge of the aperture.

Measurements were also taken at several planes away from the launcher cut to determine the expansion of the beam. The radius of the beam is determined from the -8.68 dB line in the radiation pattern. Fig. 4.24 shows the radius of the launched beam as function of position y of the detecting plane. The result shows that the actual beam is expanding at a faster rate than theoretical predictions. This indicates that the mode content in the radiated beam could be different from the predictions of the coupled mode theory. The large difference between the design and the actual inner wall pattern could be the most plausible cause for the discrepancy.

There is an ongoing effort at MIT to develop a phase-reconstruction theory that allows one to retrieve the phase information of an RF wave from amplitude measurement data. If successful, the amplitude and the reconstructed phase information can be used to design the mirror transmission line to be used with this launcher. However a preliminary result of phase-reconstruction was unsatisfactory, probably due to the fast-expanding beam phase front. As a first cut design, the first mirror was chosen based on the Gaussian optics theory with the Gaussian waist fitted to the beam expansion in Fig. 4.24.

Figure 4.20: Measured output pattern from the launcher at $y = 6\,\text{cm}$.
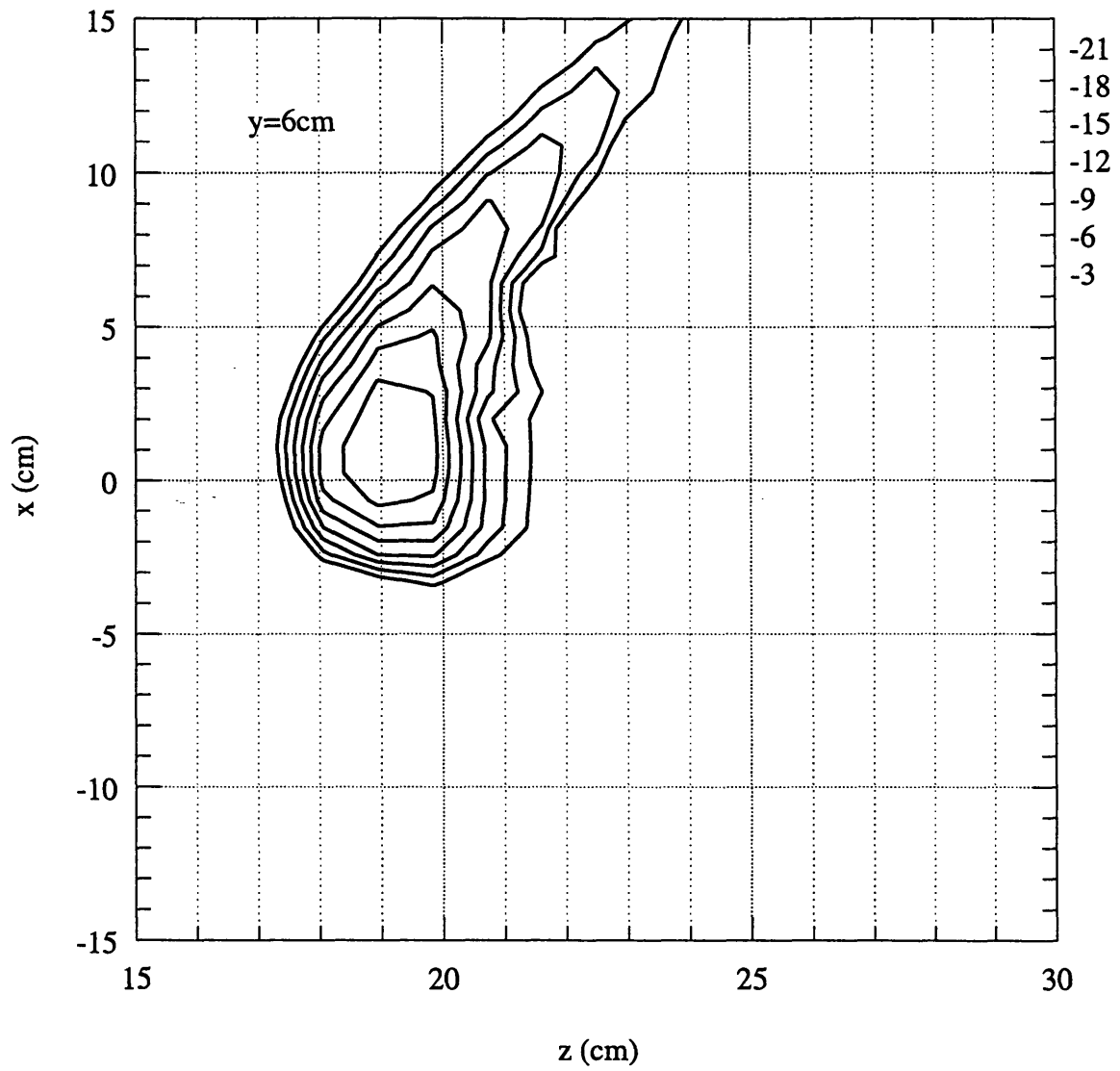
Figure 4.21: Predicted output pattern at $y = 6\,cm$ from Stratton-Chu diffraction theory.
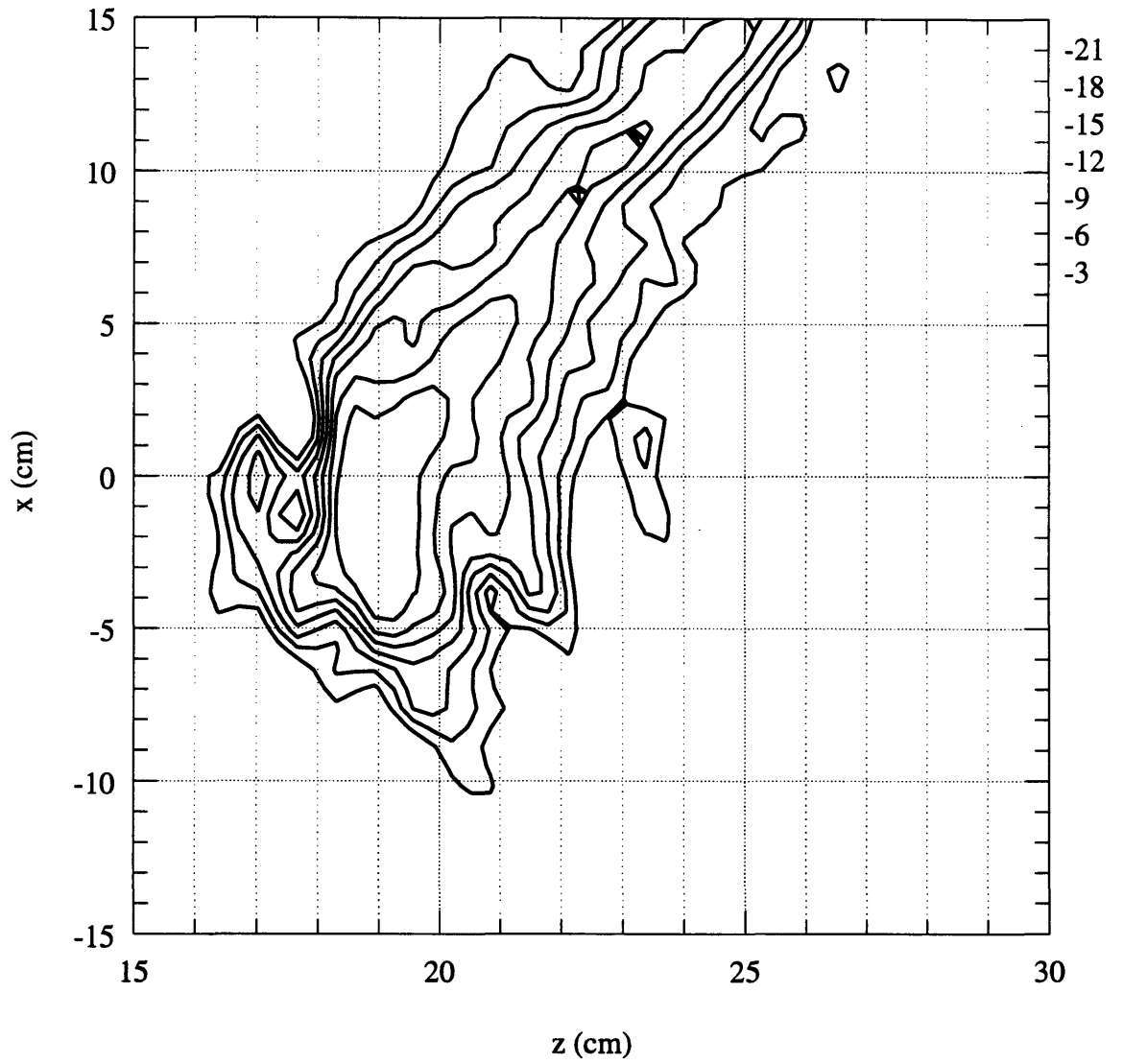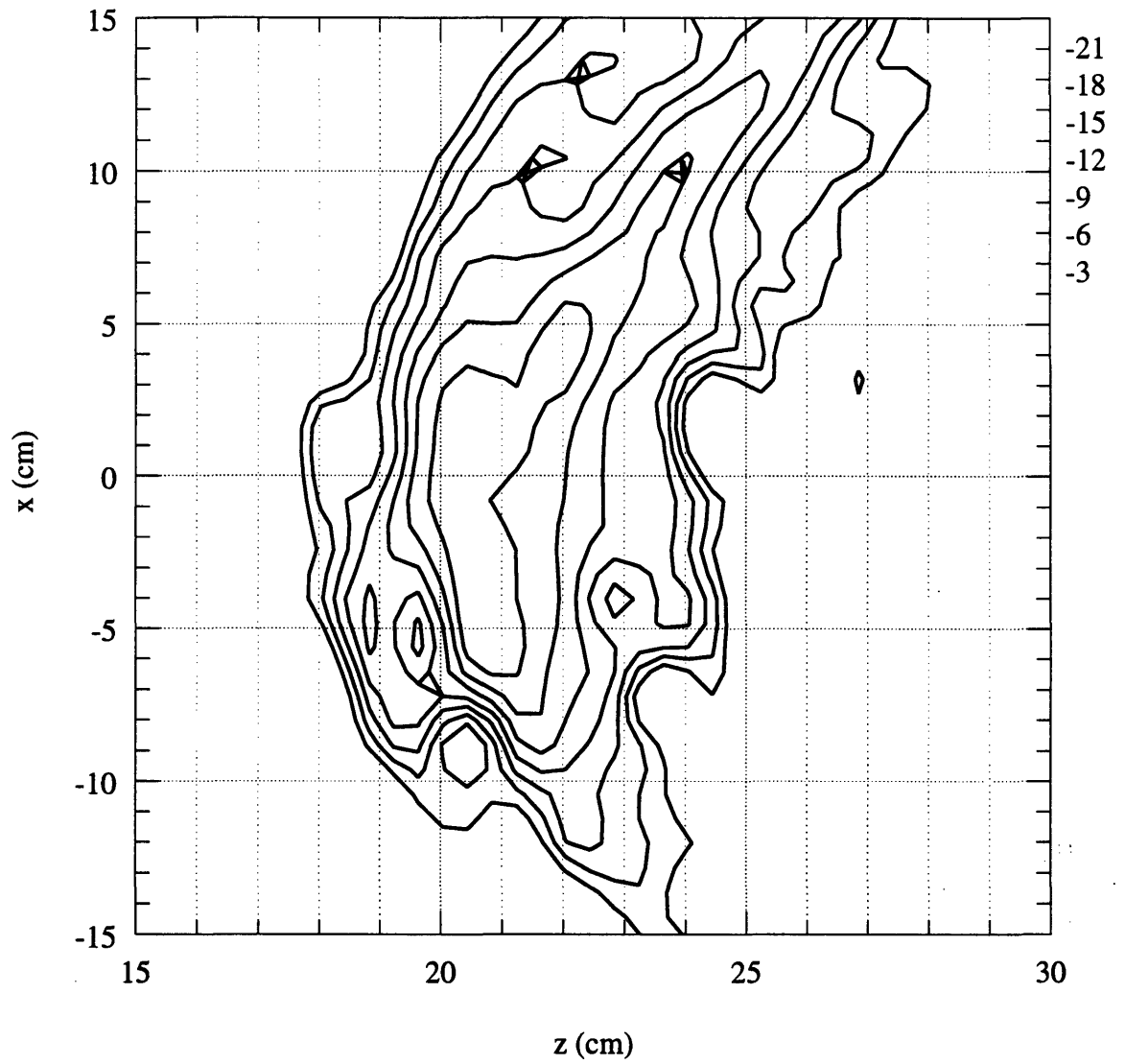
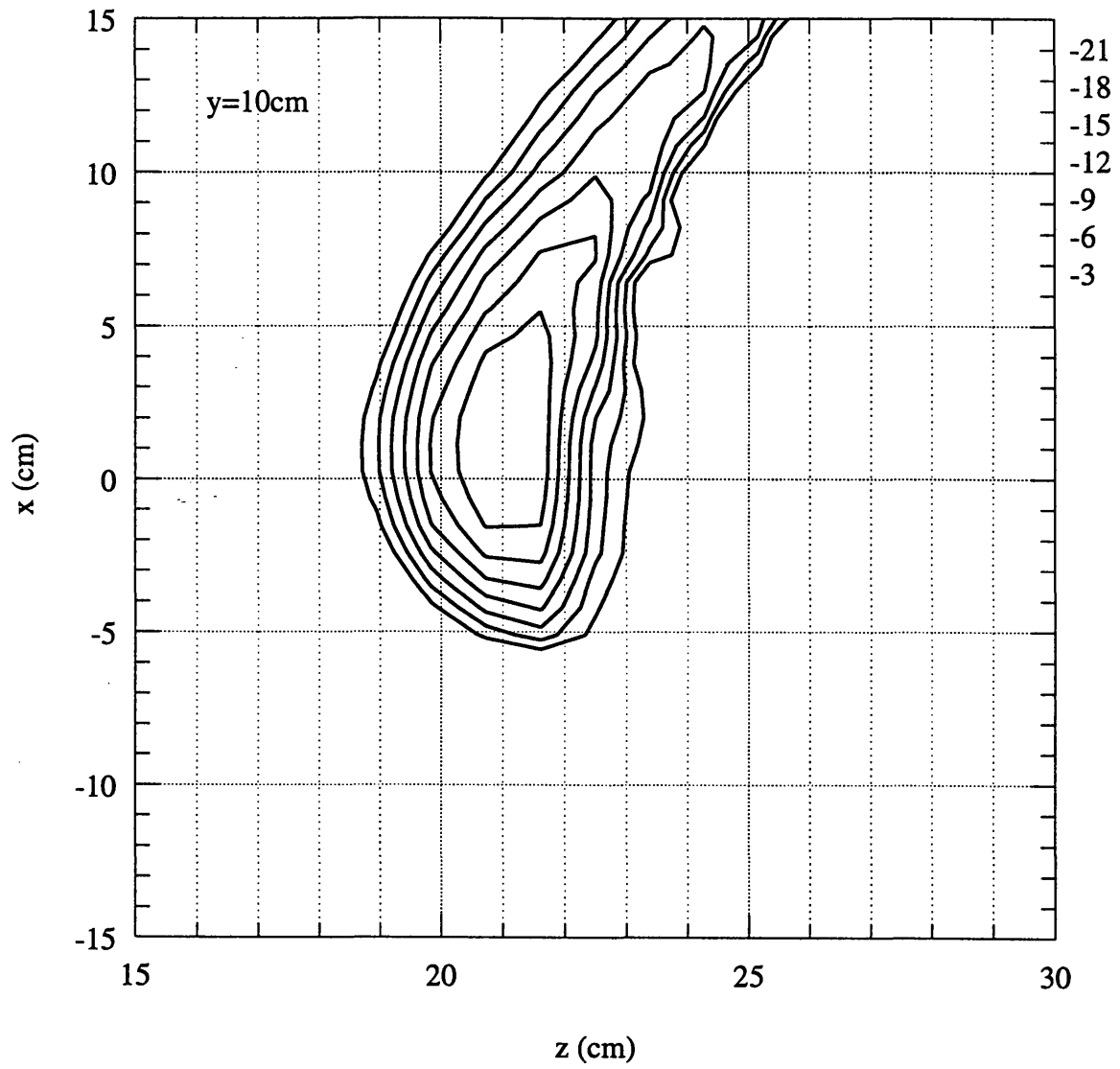Figure 4.22: Measured output pattern from the launcher at $y = 10$ cm.

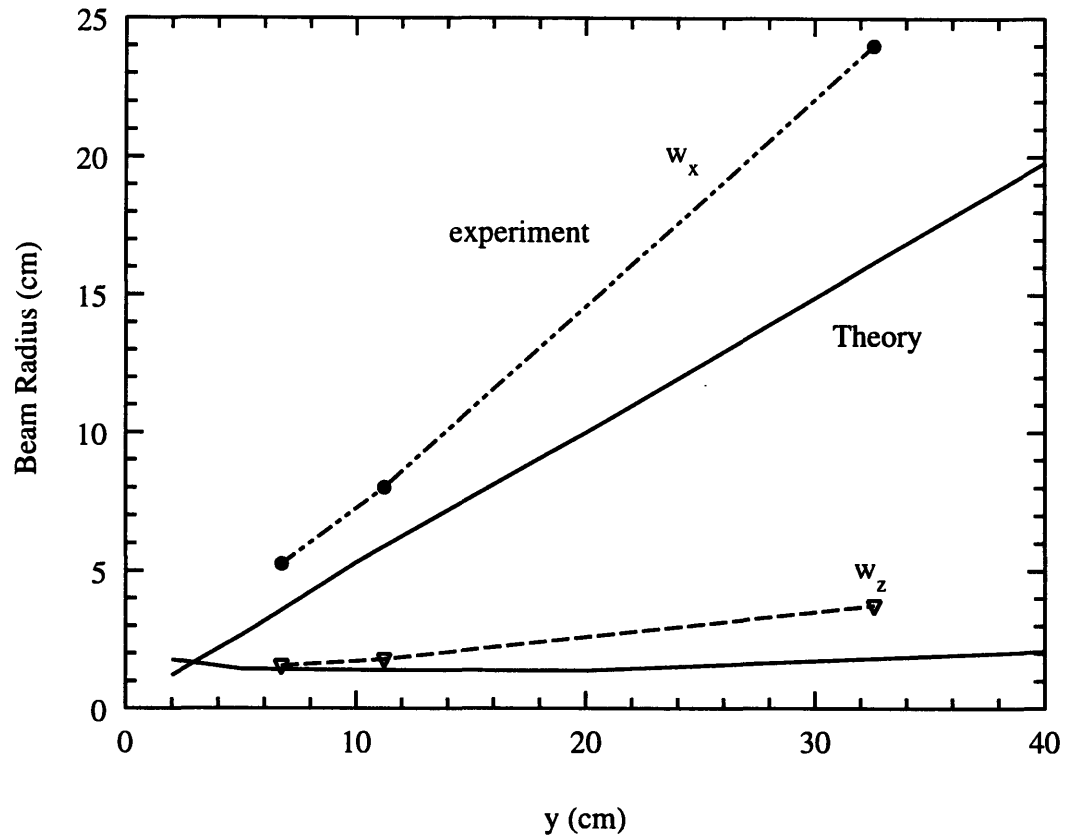Figure 4.23: Predicted output pattern at $y = 10\,\text{cm}$ from Stratton-Chu diffraction theory.

Figure 4.24: Expansion of beam waist of the radiation from the launcher. The dot-lines are the measurements and the continuous lines are the theoretical predictions of the Stratton-Chu theory.

Chapter 5

Summary

This experiment has successfully demonstrated that 1.5 MW RF power can be generated by a pulsed gyrotron at 170 GHz with a total efficiency of 35%. The whole design is compatible with 1 MW CW operation that would meet the requirements of ITER for bulk heating and current drive. The excellent results are based on careful study and designing of the electron gun and the interaction cavity.

The initial cavity design was optimized with a single-mode, self-consistent code for a maximum RF efficiency of 45% within the ohmic heating constraint. A time-dependent, multi-frequency, multi-mode and self-consistent code was then utilized to assess the performance of the cavity when excitations of competing modes are taken into consideration. Multi-mode simulation shows that only 32% RF efficiency can be achieved due to enhanced mode competition in a long cavity with normalized interaction length μ of 16. The design was subsequently modified to have a shorter interaction length and μ of 14. The reduction in the cavity quality factor due to shortened length was compensated by an iris step at the end of the cavity straight section. Multi-mode simulation predicts 38% RF efficiency with this new cavity for a realistic beam perpendicular velocity spread of 10%. The peak ohmic loss density on the cavity wall is calculated to be 2.3 kW/cm^2 for 1 MW final output power.

The electron gun was designed using EGUN code with an improved space charge algorithm. Electrode shapes were optimized for minimum spread due to beam optics. Further reduction in velocity spread was achieved through analysis of the non-adiabatic behavior of the electron beam. Estimates of the total spread using a first order approximation shows that by designing

a non-adiabatic gun such that the beam velocity ratio is insensitive to variations of operating parameters near the design point, the estimated total spread is reduced by 20% compared to an adiabatic gun, and by 100% compared to a non-adiabatic gun with high sensitivity.

The initial experiment, from which all of the experimental data in this thesis are taken, was conducted without an internal mode converter. Highest output power of 1.5 MW was achieved with single-mode operation in both the $TE_{28,8,1}$- and the $TE_{27,8,1}$- mode with 50 A, 84–86 kV beam for efficiencies of 34–35%. At the design operating point of the gyrotron, 1.1 MW power was measured with a 36 A, 84 kV beam. The corresponding efficiency is 36%.

For the $TE_{28,8,1}$- mode, the strongest competition comes from $TE_{25,9,1}+$ and $TE_{27,8,1}$- modes. To suppress the excitation of the $TE_{25,9,1}+$ mode, one needs to increase the beam radius from 0.828 cm to 0.840 cm, thus decreasing slightly the coupling for the $TE_{28,8,1}$- mode, but significantly that for the $TE_{25,9,1}+$ mode. The highest efficiencies achieved in the experiment agree with prediction of the multi-mode code but are lower than that of the single-mode simulations.

Excitation of modes during the startup was studied. Comparison with the linear starting current curves shows good agreement. Oscillation of modes in the hard excitation region was identified.

A map of modes was constructed in the plane of cathode and cavity magnetic fields. Two sets of radial modes consistent with the beam compression ratios were found. The $TE_{28,8,1}$ mode is shown to have a relatively small operating region in the mode map. This was attributed to the fact that the output window is only matched to the design frequency, and power reflection at other frequencies changes the quality factors for other modes. A discrete frequency jump was observed in the frequency versus detuning measurement for the $TE_{27,8,1}$ mode, indicating that power reflection at the window is influencing the gyrotron operation.

The properties of the electron beam were also measured. The velocity ratios $v_\perp/v_\parallel$ as measured by the capacitive probe are generally in good agreement with the EGUN simulation results. The non-adiabatic nature of the beam is evident in the oscillatory dependence of α on the cathode voltage. Velocity spreads were estimated at different beam current levels from measurements of the reflected current as a function of the average velocity ratio. A rough estimate of the spread based on the assumption of a square distribution function of $v_\perp$ yielded

a spread as a function of beam current that is qualitatively in agreement with the theoretical estimate of spread with all the known contributions.

Finally the dimpled wall launcher was tested externally using the output power from the gyrotron. Two-dimensional scans of the radiation from the launcher were taken at several detection planes. A Gaussian-like beam was obtained. Results show that the actual beam size is expanding faster than the theoretical predictions, which are calculated from the coupled mode theory and the Stratten-Chu diffraction theory. There is good agreement between theory and experiment for the propagation angle of the beam in the axial direction. The propagation in the azimuthal direction differs by approximately 12°.

The next step in the gyrotron experiment is to complete the external testing of the mode converter. Since the radiation pattern from the launcher is different from the expected pattern, the original design of the mirror transmission line has to be modified to achieve the desired field at the output window. The first mirror was designed with the shape of the mirror surface determined using the measured beam expansion which is fitted to a Gaussian form. This mirror has already been fabricated. The design of the second mirror can be determined after the beam expansion from the first mirror is measured. Following this process, the third and fourth mirror can also be designed. The final adjustment could be made by changing the positions of all four mirrors, or if necessary, slight adjustment to the shape of the fourth mirror.

The output from the mode converter designed using the above scheme could be quite different from the desired circular Gaussian pattern with 2.85 cm waist at the window. A better alternative would be to retrieve the phase information of the RF beam using the phase-reconstruction code which is currently under development at MIT. By reconstructing the phase of the beam from the amplitude measurement after the second mirror, the last two mirrors can be optimized to achieve the desired output.

If the internal mode converter test proves to be successful, then a depressed collector can be implemented to improve the overall efficiency of the gyrotron. By applying a retarding voltage on the collector thus slowing down the spent electrons reaching the collector, part of the beam energy can be recovered. Theoretical study suggests that a single-stage depressed collector can enhance the efficiency from 35% to 50%, while 65% efficiency can be achieved with a multistage depressed collector.

We can also explore gyrotron operation at 150 GHz and 190 GHz since a step-tunable gyrotron is very attractive in applications. The thickness of the output window can be chosen so that it is matched to these frequencies as well as 170 GHz. During the initial testing, 540 kW power has been measured in the $TE_{23,8}$ mode at 152.9 GHz with 31% efficiency. To operate at 190 GHz, the Lambda plate on the superconducting magnet needs to be activated so that field over 7.5 T can be reached. Study is also needed to determine how the internal mode converter performs for these modes.

Bibliography

[1] V. Erckmann and U. Gasparino. Electron cyclotron resonance heating and current drive in toroidal fusion plasmas. *Plasma Phys. Control Fusion*, 36:1869–1962, 1994.

[2] M. Makowski. ECRF systems for ITER. *IEEE Transactions on Plasma Science*, 24(3):1023–32, 1996.

[3] Y. Takase, R.L. Boivin, F. Bombarda, P.T. Bonoli, C.L. Fiore, D. Garnier, J.A. Goetz, S.N. Golovato, R.S. Granetz, M.J. Greenwald, S.F. Horne, A.E. Hubbard, I.H. Hutchinson, J.H. Irby, H. Kimura, R. Majeski, E.S. Marmar, M. May, A. Mazurenko, P. O'Shea, R. Pinsker, M. Porkolab, J. Reardon, J.E. Rice, C. Rost, J. Schachter, J.A. Snipes, P. Stek, J.L. Terry, R.L. Watterson, B. Welch, and S.M. Wolfe. Survey of ICRF heating experiments and enhanced performance modes in Alcator C-Mod. *Plasma Physics and Controlled Fusion*, 38(12):2215–29, 1996.

[4] Y. Fujiwara, T. Inoue, K. Miyamoto, N. Miyamoto, Y. Ohara, Y. Okumura, K. Shibata, S. Suzuki, M. Tanii, and K. Watanabe. Design and R&D for ITER NBI system at JAERI. *Fusion Technology*, 30(3):810–14, 1996.

[5] D.A. Kislov, V.V. Alikaev, Yu.V. Esipchuk, A.M. Kakurtn, A.Ya. Kislov, D.A. Martynov, G.E. Notkin, K.A. Razumova, and V.V. Sushkov, A.V.and Volkov. The $m = 2, n = 1$ mode suppression by ECRH on the T-10 tokamak. *Nuclear Fusion*, 37(3):339–50, 1997.

[6] H. Nakamura, J. Dietz, and P. Ladd. Wall conditioning in ITER. *Vacuum*, 47(6-8):653–5, 1996.

[7] K. Felch, M. Blank, P. Borchard, T.S. Chu, and J. Feinstein. Long-pulse and CW tests of a 110 GHz gyrotron with an internal, quasi-optical converter. *IEEE Trans. Plasma Sci.*, 24(3):558, 1996.

[8] Sato M., T. Shimozuma, Y. Takita, S. Kubo, H. Idei, Ohkubo K., T. Kuroda, T. Watari, M. Loring, Chu S., K. Felch, and H. Huey. *Proceedings of the 20th Int. Conf. Infrared and Millimeter Waves*, page 195, 1995.

[9] G.G. Denisov, A.N. Kuftin, V.I. Malygin, N.P. Venediktov, and V.E. Zapevalov. *Int. Journal Electronics*, 72(1079):1091, 1992.

[10] S. Alberti, O. Braz, P. Garin, Giguet E., M. Pain, P. Thouvenin, M. Thumm, C. Tran, and M.Q. Tran. *Proceedings of the 21st Int conf. Infrared and Millimeter Waves*, page AF1, 1996.

[11] G. Dammertz, O. Braz, C.T. Iatrou, M. Kuntze, A. Moebius, B. Piosczyk, and M. Thumm. Long-pulse operation of a 0.5 MW $TE_{10,4}$ gyrotron at 140 GHz. *IEEE Trans. Plasma Sci.*, 24(3):570, 1996.

[12] R.Q. Twiss. Radiation transfer and the possibility of negative absorption in radio astronomy. *Australian J. Phys.*, 11:564–579, 1958.

[13] J. Schneider. Stimulated emission of radiation by relativistic electrons in a magnetic field. *Phys. Rev. Lett.*, 2:504–505, 1959.

[14] A.V. Gapanov. Interaction between electron fluxes and electromagnetic waves in waveguides. *Izv. VUZ., Radiofizika*, 2:450–462, 1959.

[15] R.H. Pantell. Backward-wave oscillations in an unloaded guide. *Proc. IRE*, 47:1146, 1959.

[16] J.L. Hirshfield and J.M. Wachtel. *Phys. Rev. Lett.*, 12:533–6, 1964.

[17] A.V. Gapanov, M.I. Petelin, and V.K. Yulpatov. *Radiophys. Quantum Electron*, 10:794, 1967.

[18] K.R. Chu and J.L. Hirshfield. Comparative study of the axial and azimuthal bunching mechanisms in electromagnetic cyclotron instabilities. *Phys. Fluids*, 21:461, 1978.

[19] Ronald C. Davidson. *Physics of Nonneutral Plasmas*, page 348. Addison Wesley, 1990.

[20] A.W. Fliflet, M.E. Read, K.R. Chu, and R. Seeley. A self-consistent field theory for gyrotron oscillators: application to a low Q gyromonotron. *Int. J. Electron.*, 53(6):505–521, 1982.

[21] M. Abramowitz and I.A. Stegun. *Handbook of Mathematical Functions*, page 355. New York: Dover Publications, 1970.

[22] A.W. Fliflet and J.M. Baird. Development of a computer code to study self-consistent RF field -electron beam interactions in gyromonotrons. Technical Report BKD TR3-488, B-K Dynamics, Inc., 1982.

[23] A.W. Fliflet, R.C. Lee, S.H. Gold, W.M. Manheimer, and E. Ott. Time-dependent multi-mode simulation of gyrotron oscillators. *Phys. Rev. A*, 43(11):6166–6176, 1991.

[24] S.Y. Cai, T.M. Antonsen, G. Saraph, and B. Levush. Multifrequency theory of high power gyrotron oscillators. *Int. J. Electronics*, 72(5-6):759–777, 1992.

[25] B.G. Danly and R.J. Temkin. Generalized nonlinear harmonic gyrotron theory. *Phys. Fluids*, 29(2):561–567, 1986.

[26] J.D. Jackson. *Classical Electrodynamics*. New York: Wiley, 1975.

[27] R.J. Temkin. Analytic theory of a tapered gyrotron resonator. *Int. J. Infrared Millimeter Waves*, 2:629–650, 1981.

[28] J. Mark Baird and Wes Lawson. Magnetron injection gun (MIG) design for gyrotron applications. *Int. J. Electronics*, 61(6):953–967, 1986.

[29] J.L. Cronin. Modern dispenser cathodes. *IEEE Proceedings*, 12:19–32, 1981.

[30] W.B. Herrmannsfeldt. Electron trajectory program. (226), November 1979.

[31] J.R. Pierce. *Theory and Design of Electron Beams*. D. Van Nostrand Co., Princeton, New Jersey, 1954.

[32] A.K. Ganguly and K.R. Chu. Limiting current in gyrotrons. *Int. J. Infrared and MM Waves*, 5(1):103–121, 1984.

[33] Sh. E. Tsimring. Limiting current of helical electron beams in gyrotrons. *Int. J. of Infrared and Millimeter Waves*, 14(4):817–840, 1993.

[34] P. Avivi and Ch. Cohen. *Appl. Phys. Lett.*, 42:948, 1983.

[35] W.C. Guss, T.L. Grimm, K.E. Kreischer, J.T. Polevoy, and R.J. Temkin. Velocity ratio measurements of a gyrotron electron beam. *J. Appl. Phys.*, 69(7):3789, 1991.

[36] J.P. Calame, J. Cheng, B. Hogan, W. Lawson, C.D. Striffler, P.E. Latham, and V. Irwin. Measurements of velocity ratio in a 90 MW gyroklystron electron beam. *IEEE Trans. Plas. Sci.*, 22(4):476, 1994.

[37] T.M. Tran, G. Jost, K. Appert, S. Alberti, and M. Pedrozzi. Particle-in-cell (PIC) simulations of beam instabilities in gyrotrons. To appear in *Physics of Plasmas*.

[38] Girish.P. Saraph, Thomas M. Antonsen, B. Levush, and G.I. Lin. Regions of stability of high-power gyrotron oscillators. *IEEE Trans. Plasma Science*, 20(3):115–125, 1992.

[39] W. G. Lawson. Theoretical evaluation of nonlinear tapers for a high-power gyrotron. *IEEE Trans. on Microwave Theory and Techniques*, 38(11):1617–1622, 1990.

[40] R.A. Correa, A.B. Levush, and T.M. Antonsen. High efficiency cavity design of a 170 GHz gyrotron for fusion applications. *Physics of Plasmas*, 4(1):209–16, 1997.

[41] Steven J. Sackett. Users manual for EFFI – a code for calculating the electromagnetic field, force and inductance in coil systems of arbitrary geometry. Technical Report UCID-17621, Lawrence Livermore National Laboratory, 1981.

[42] Sh. E. Tsimring. On the spread of velocities in helical electron beams. *Radiofizika*, 15(8):1247–1259, 1972.

[43] B. Piosczyk. *Int. J. Electron.*, 67:447–56, 1989.

[44] Monica Blank, Kenneth Kreischer, and R.J. Temkin. Theoretical and experimental investigation of a quasi-optical mode converter for a 110 GHz gyrotron. *IEEE Trans. on Plasma Science*, 24(3):1058–1066, 1996.

[45] Monica Blank. *High Efficiency Quasi-Optical mode converters for overmoded gyrotrons.* PhD thesis, MIT, 1994.

[46] G.G. Denisov, d.A. Lukovnikov, W. Kasparek, and D. Wagner. On the resonant scattering at guide dielectric windows. *Int. J. of Infrared and Millimeter Waves*, 17(5):933–945, 1996.

[47] Mohammed Nurul Afsar and Kenneth J. Button. *Infrared and Millimeter Waves*, volume 12, pages 1–42. New York: Academic Press.

[48] D.R. Whaley, M.Q. Tran, S. Alberti, and T.M. Tran. Startup methods for single-mode gyrotron operation. *Phys. Rev. Lett.*, 75(7):1304, 1995.

[49] E. Borie and B. Joedicke. Rieke diagrams for gyrotrons. *Int. J. of Infrared and Millimeter Waves*, 11:243–250, 1990.

[50] T.M. Antonsen, S.Y. Cai, and G.S. Nusinovich. Effect of window reflection on gyrotron operation. *Phys. Fluids B*, 4:4131–4139, 1990.

[51] W.C. Guss, M.A. Basten, K.E. Kreischer, and R.J. Temkin. Velocity spread measurements on a magnetron injection gun beam. *J. Appl. Phys.*, 76(6):3237–3243, 1994.

[52] A.S. Gilmour Jr. *Principles of Traveling Wave Tubes.* Boston, London: Artech House, 1994.

[53] J.L. Doane. Propagation and mode coupling in corrugated and smooth-wall circular waveguide. *Infrared and Millimeter Waves*, 13:1109–1133, 1986.